Transport thermique dans des membranes très minces de SiN amorphe

Hossein Ftouni

UNIVERSITÉ DE GRENOBLE

THÈSE

Pour obtenir le grade de

DOCTEUR DE L'UNIVERSITÉ DE GRENOBLE

Spécialité : **Physique de la Matière Condensée et du Rayonnement**

Arrêté ministériel : 7 août 2006

Présentée par

Hossein Ftouni

Thèse dirigée par **Olivier Bourgeois**

préparée au sein **de l'Institut Néel, CNRS - Grenoble**
et de **l'école doctorale de Physique**

Thermal transport in very thin amorphous SiN membranes

Thèse soutenue publiquement le **12 décembre 2013**,
devant le jury composé de :

Mme. Séverine Gomès
Chargée de Recherche, Rapporteur
M. Jean-Yves Duquesne
Chargé de Recherche, Rapporteur
M. Frédéric Ayela
Professeur, Examinateur
M. Stefan Dilhaire
Professeur, Examinateur
M. Emmanuel Hadji
Directeur de recherche, Examinateur
M. Jay Amrit
Maître de conférences, Invité
M. Olivier Bourgeois
Chargé de recherche, Directeur de thèse

Acknowledgments

In the preamble of this memory, I wish to express my sincere thanks to those who supported me and who contributed to the development of this thesis during the last three years. This work has been carried out at the Department of Condensed Matter - Low Temperatures (MCBT) of the Institut néel, CNRS - Grenoble during the years 2011-2013.

First of all, I would like to acknowledge my supervisor, Dr. Olivier Bourgeois for trusting me and giving me this opportunity to work in his team, as well as for his guidance and support during the past years. I would also like to thank all the members of thermodynamics of small systems team, as well as the members of pôle capteur: Jean-Luc Garden, Emmanuel Pierre André and Pierre Lashkar. I also acknowledge all the assistance I received in fabrication processes in cleanroom (Nanofab facility), particularly, Thierry Crozes and Bruno Fernandez, as well as the support from cryogenic shop and electronic shop. I would like to thank Pierre Brosse-Marron and Christophe Guttin for all their help with mechanic and electronic related issues. Special thanks go to Jacques Richard for his help and fruitful scientific exchanges.

Finally, Warm thanks to my parents, my sisters, my brother, for their unwavering support during the course of my studies. Living away from home, made me realize how much their love and support mean to me.

Contents

List of Figures

List of Tables

Introduction

With recent developments of two-dimensional and one-dimensional nano structured materials, many limits of bulk (three-dimensional) material properties are being exceeded. Although many research works have been done in this field recently, there is still a need for a better understanding of thermal phenomena in reduced dimension systems. Typically, there are two types of interest: at a technological level, the design of novel structures with desirable thermal properties is highly required for different applications. Away from the technological considerations, the study of thermal properties at the nanoscale presents fundamental questions about the interaction of heat transfer and microstructure at these small length scales.

Thermal properties are essential to optimize the performance of many low temperature and/or nanostructure devices. Moreover, multi-domain coupling (electrical, mechanical and thermal) is an essential feature of micro and nanoscale devices. These devices are commonly fabricated out of thin film materials. While electro-mechanical coupling is commonly exploited in microelectronic and other small-scale systems, the thermal domain must also be considered in these applications. Thermo-mechanical coupling in thin films is typically studied in terms of temperature effects on mechanical properties, and not from a thermal transport perspective. Furthermore, measuring the thermal properties of these nanostructured materials can prove challenging because of their small size and potentially large aspect ratios.

In this thesis work, we have been interested in studying the thermal properties of silicon nitride thin films and the effects of intrinsic stress on its thermal properties. Therefore, thermal properties of both silicon nitride low stress and high stress are measured respectively. These measurements have been performed with 50 nm and 100 nm membrane thick of both SiN low stress and high stress from low temperature (300 mK) up to room temperature. To attain this objective, we have developed a system designed to measure with a very high sensitivity both the thermal conductance and the heat capacity of suspended membrane. This is a versatile method based on the 3ω method coupled to the Völklein geometry (suspended membrane) and can cover a wide temperature range. Finally, we propose that the SiN membranes that have been characterized can be used as a highly sensitive sensor to measure thermal properties of another material deposited on the backside of the membrane.

In Chapter 1 we provide an overview of phonon transfer at the nanoscale, especially in membrane and amorphous materials and thus gives the necessary background for this thesis. We will discuss the size effect on the characteristic lengths of phonon carriers and the particularities of

the glasses and some of possible applications of nanostructures. Then, we will introduce our material of interest studied in this thesis, which is a typical amorphous material based on silicon nitride membrane of low and high stress. Finally, we will discuss the experimental techniques specific for the measurement of thermal properties of thin film.

In chapter 2 we introduce the 3ω-Völklein method. We explain how by using a specific Wheatstone bridge we can detect the weak 3ω voltage. We then study the possible effect of the electrical capacities which can be present in the measurement chain.

In chapter 3 we present the heat transfer model specific to the suspended membrane geometry. In order to determine the exact temperature solution, the heat conduction with the 2-dimensional model is first derived. Then to simplify, the 1-dimensional solution is derived using some assumptions. The difference between the two models on the extracted thermal properties will then be presented. Afterwards, the effect of a finite transducer width will be discussed. Finally in order to validate the 3ω-Völklein method, we present experimental measurements fitted by the theoretical model, the sensitivity of this method will be discussed.

In chapter 4 we present experimental results of thermal propertie measurements for 50 nm and 100 nm suspended SiN membranes, in the two cases of low stress and high stress. In order to predict any possible effect of stress on thermal properties, the thermal conductivity and the specific heat will be fitted using a theoretical model. Moreover the phonon diffusion in such system will be discussed in term of temperature, phonon mean free path and roughness. Finally, we present experimental results at low temperature (300 mK - 10 K) of 50 nm and 100 nm high stress silicon nitride membrane.

In chapter 5 we demonstrate the application of the SiN sensor (constituted by a 100 nm SiN membrane and the deposited NbN thermometer on topside), to the measurement of thermal conductance and heat capacity of 200 nm Bi_2Te_3 film. The Bi_2Te_3 film is deposited on the backside of the SiN membrane by magnetron sputtering technique.

Chapter 1

Nanoscale heat transfer

1.1 Characteristic of nanoscale heat transfer

Heat transfer across solid state materials is limited by diffusion of different heat carrier's types, such as electrons, photons and phonons which can vary according to the materials nature. At the nanometer scale, heat transfer diverges significantly from that at the macro and microscales. The size effects become more important when the mean free path and/or wavelength of heat carriers become comparable to the device length scales. Moreover, at that scale the relaxation time of the heat carries is on the same order of the time of interest (for example: heating, thermalization, and diffusion time). At these limits, classical laws become no longer valid [1–3]. For instance, thermal conductivities are often described following the models developed by Klemens [4], Callaway [5] based on Boltzmann equation applied to phonon transfer, and Debye approximation for phonon dispersion. The extracted properties from such model lead to qualitative understanding of phonon transport.

Although many research works have been done in this field recently, there is still a need for a better understanding of thermal phenomena in reduced dimension systems. Typically, there are two types of interest:

- at a technological level, the concern is to increase the performance of thermoelectric and energy conversion devices, where the particular properties of a material at nanoscale can be very useful [6, 7]. Moreover, concern is to maintain best conditions of functionality and reliability of integrated circuits [8].

- away from the technological considerations, the study of thermal properties at nanoscale presents fundamental questions about the interaction of heat transfer and microstructure at these small length scales that need to be addressed.

Moreover, the accurate measurement and characterization of the thermal properties of nanos-

tructures materials poses many challenges in term of technique and require the fabrication of very small sample. Fig. 1.1 shows an example of suspended membrane and nanowire geometry usually used to study heat transfer at nanoscale.

This chapter will provide an overview of phonon transfer at the nanoscale, especially in membrane and amorphous materials and thus gives the necessary background for this thesis. In the following sections, we will discuss the size effect on the characteristic lengths of phonon carriers and the particularities of the glasses and some of possible applications of nanostructures. Then, we will introduce our material of interest studied in this thesis, which is a typical amorphous material based on silicon nitride membrane of low and high stress. Finally, we will discuss the experimental techniques specific for the measurement of thermal properties of thin film.
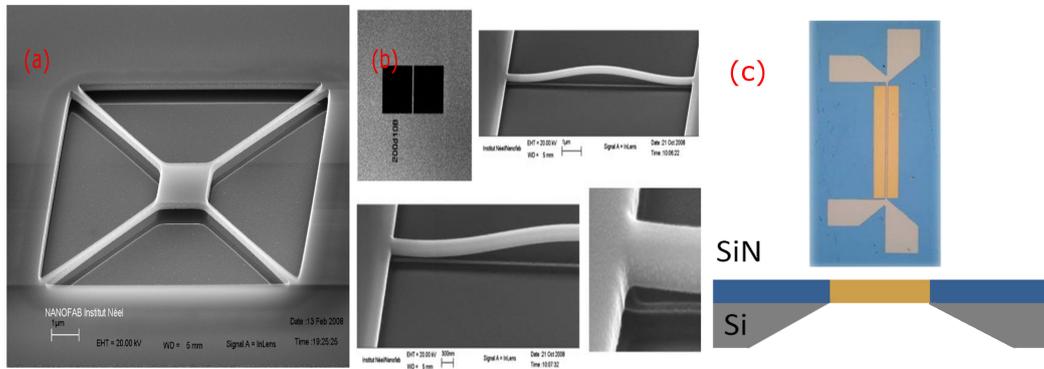
Figure 1.1: SEM images of (a) suspended silicon membrane, (b) and suspended silicon nanowire fabricated at the Institut Néel [9]. (c) Top: topside view of a chip with heater/sensor strip on silicon nitride membrane and contacts pads; bottom: schematics shows the cross section of suspended membrane geometry.

1.1.1   Notion of phonon

The heat carriers in solids are represented by electrons and by quantized lattice vibrations called "phonons". A phonon is a quasi-particle that transports a quantum of vibrational energy. In the study of phonon transfer in nanostructure, it is essential to compare these characteristic lengths to the dimensions of devices.

The vibrational modes of phonon are treated like waves, where the mean free path l is the average distance traveled by the wave before undergoing an inelastic collision and losing its phase coherence. In bulk crystalline materials, at low temperature this distance can be very large and may reach the order of centimeters. In nanostructures, collision with rough surfaces can reduce the average mean free path.

The phonons transport a quantum of energy equal to $\hbar\omega$, with ω the wave frequency in rad/s and $\hbar = h/2\pi$ where $h = 6.6260695 \ 10^{-34}$ J.s is the Planck constant. The vibration is

also defined by the wave vector of propagation given by $k = 2\pi/\lambda$, λ is the wavelength of oscillation. The wave vector direction indicates the direction of the wave propagation in the lattice. Phonons can propagate in all directions, therefore k_x, k_y and k_z define the wave space or phase space.

In three dimensional lattice, acoustic waves have three possible polarizations, one longitudinal polarization and two transverse polarizations. The longitudinal polarization corresponds to vibrations of atoms in the same direction of the wave propagation. Atoms can also vibrate perpendicularly to the wave propagation, this is the transverse polarization. Fig. 1.2 shows the polarization in the simplest system represented by a linear chain of atoms.
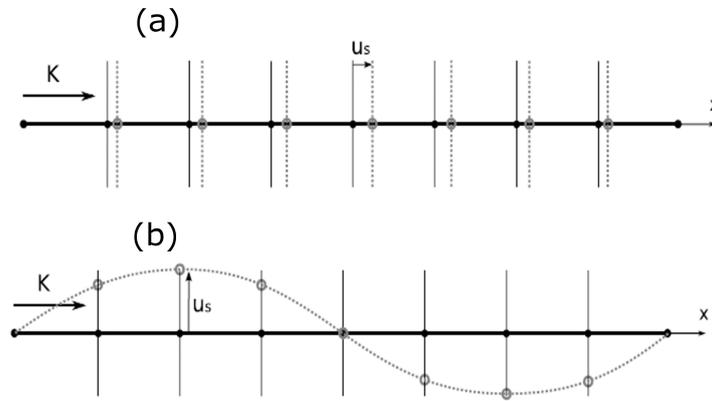
Figure 1.2: Schematics showing the vibration of atoms inside a lattice as function of the wave polarization (a) longitudinal polarization, (b) transverse polarization.

To describe the lattice vibration in term of wave characteristics (such as its frequency, wave length), the simplest system representing an infinite periodic lattice with periodic boundary conditions is introduced. This corresponds to the one dimensional chain of atoms with similar masses and spring constants as shown by Fig. 1.3.

The aim of this section is to derive the dispersion relation that provides the relation between the angular frequency ω and the wave vector k. As shown in Fig. 1.3, mono-atomic crystal has one atom in the primitive cell. When the atoms vibrate, they move from their equilibrium positions. Then, the vibration can be described as a wave propagation through the material.

Due to the connections between atoms, the displacement of one atom will affect all the others. In Fig. 1.3, due to the displacement u, of atoms at position $s\pm1$, the resultant force on atom at position s is proportional to the difference $u_{s\pm1} - u_s$. The force F is given by Hook's law, $F = -C_s(u_{s+1} - u_s) - C_{s-1}(u_s - u_{s-1})$, where $C_s = C_{s-1}$. Therefore, Newton's second law yields:

$$M\frac{\partial^2 u_s}{\partial t^2} = C\left(u_{s+1} + u_{s-1} - 2u_s\right) \tag{1.1}$$
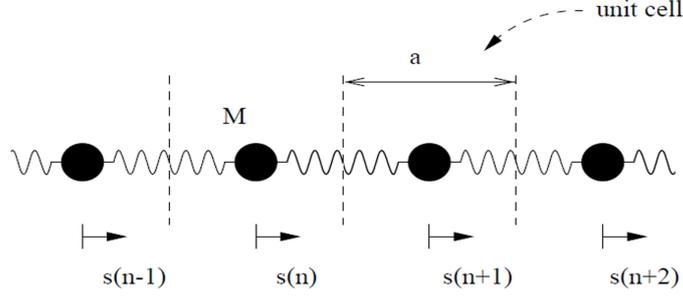
Figure 1.3: Schematic shows linear atomic chain with an atomic mass M, lattice constant a, and spring constant C_s where s depicts the position of atom.

Let us assume that all displacements have the same frequency dependency ($\exp(-i\omega t)$). In this case, we look for a solution as a sum of plane waves:

$$-M\omega^2 u_s = C(u_{s+1} + u_{s-1} - 2u_s) \tag{1.2}$$

This differential equation can be solved by assuming a solution with the form: $u_s = u\,exp(iska)$, with k the wave vector, a is the lattice constant, and s is the plane locations of the atoms. Here we are considering a simple cubic lattice, this means that a fixed phase relationship exists between any two neighbouring planes. Thus Eq. 1.2 becomes:

$$-\omega^2 M u e^{iska} = C(ue^{i(s+1)ka} + ue^{i(s-1)ka} - 2ue^{iska}) \tag{1.3}$$

Which may be simplified using the exponential definition of the cosine: $\omega^2 = \frac{4C}{M}sin^2\frac{ka}{2}$. This is the dispersion relation for an elastic wave of wave vector k and frequency ω. As shown in Fig. 1.4, dispersion relation relates the frequency ω to the wave vector k. $\upsilon_g = \partial\omega/\partial k \neq 0$, where υ_g is the group velocity, then this is an acoustic propagation modes.

As expected ω is a periodic function of k and symmetric with respect to k and -k. The first period that lies between $k = -\pi/a$ and $k = \pi/a$ is the first Brillouin zone.[1]

The wave vectors k that are physically relevant are contained within the first Brillouin zone. The wave vectors outside the first Brillouin zone are always the reproduction of values within the first Brillouin zone, and can always be transformed back into the first Brillouin zone. Thermal waves have group velocities represented by the velocity of energy propagation in the solid, $\frac{\partial\omega}{\partial k} = a\sqrt{\frac{C}{M}}cos\frac{ka}{2}$.

---

[1] The Brillouin zone is the Wigner-Seitz cell in the reciprocal lattice. The Wigner-Seitz cell is the smallest volume enclosure that preserves the symmetries of the Bravais lattice (the primitive unit cell).
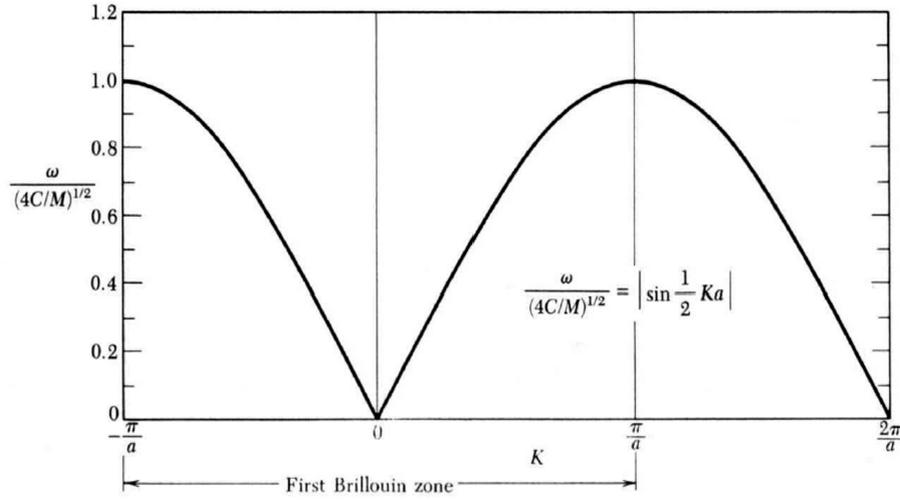
Figure 1.4: Illustration of the dispersion relation of an infinite one dimensional chain of atoms.

This permits the determination of elastic mode energy of frequency ω within the lattice. Thus, this is an essential point which allows the determination of the thermal properties of a solid.

1.1.2 Nanoscale size effect on the mean free path

The research in nanoscale heat transfer attracts significant attention since more than one decade. The most intensive research is the measurement and modeling the thermal conductivity of thin film, nanowires and superlattices due to their importance for nanoelectronics, thermoelectric devices and phononics in general [10]. It has been shown experimentally, that the thermal conductivity of low dimensional nanostructures is one or two orders of magnitude lower than the thermal conductivity values of the original bulk materials [11].

The characteristic lengths of phonon can be given by the mean free path and the phonon wavelength. The mean free path corresponds to the average distance that phonons travel between successive collisions. The corresponding average time is the collision free time, which is referred to as relaxation time. Generally, the mean free path is difficult to estimate from direct calculation, especially for electron and phonon transport in solid. The experimental thermal properties can be used to calculate the mean free path according to the kinetic theory:

$$\kappa = \frac{1}{3}C\tau\upsilon^2 = \frac{1}{3}Cl\upsilon \qquad (1.4)$$

$$\kappa = \frac{1}{3}\int_0^{\omega_{max}} C_\omega\tau_\omega\upsilon_\omega^2\, d\omega = \frac{1}{3}\int_0^{\omega_{max}} C_\omega l_\omega\upsilon_\omega\, d\omega \qquad (1.5)$$

where C the volumetric specific heat, τ the relaxation time and υ the velocity of carries. Eq. 1.4 show the integration over all the phonon frequency, with C_ω, υ_ω and τ_ω are the volumetric specific heat, the velocity and the relaxation time at each frequency respectively. While this simple model groups the contribution of all phonons, the thermal conductivity integral in Eq. 1.5 includes the impact of the phonon dispersion relations.

The phonon wavelength in a crystal varies in a wide range. Moreover, they do not contribute equally to the thermal transport. As the phonon is given by the quantum of vibration energy, the actual probability of excitation for a specific state depends on the energy of state and the temperature. Phonons are governed by the Bose-Einstein distribution as function of the wavelength, thus the energy can be given by the Planck relation $E = h\nu$. The average energy of one quantum state is $k_B T/2$ where $k_B = 1.38 \; 10^{-23}$ J/K is the Boltzmann constant. Moreover, the dominant phonon wavelength is given by $\lambda_{\text{dom}} = \frac{h\upsilon_s}{4.25 k_B T}$ [12], which is around 0.4 nm at 300 K in silicon nitride.
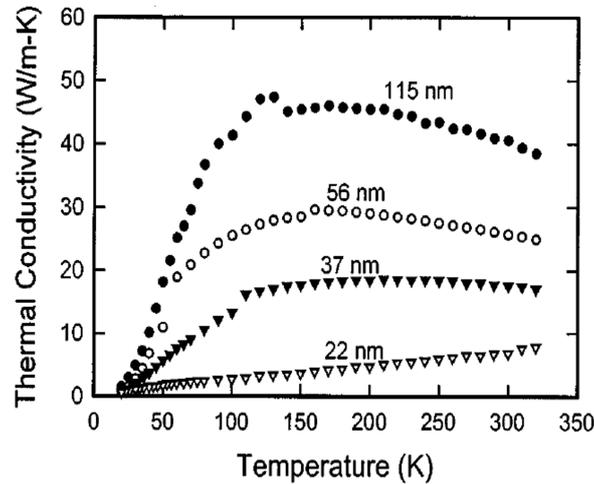
Figure 1.5: Measured thermal conductivity of different diameter Si nanowires. The number beside each curve denotes the corresponding wire diameter. [13].

A reduced system such as a quasi one dimensional (nanowire), or two dimensional material (membrane), shows a thermal conductivity which is significantly lower than a three dimensional bulk material. Fig. 1.5 shows experimental measurements of thermal conductivity for silicon nanowires with different diameters. This measurement shows a strong diameter dependence of thermal conductivity in nanowires. The thermal conductivity observed was more than two orders of magnitude lower than the bulk value. This effect is ascribed to increased phonon boundary scattering, a size effect is imposed to the phonon transport due to the small cross section area. This effect has also been observed in thin films [14].

It is widely accepted from several theoretical and computational studies [15], that the main reasons that lead to reduction in thermal conductivity, is the enhancement of the boundary phonon scattering at the nanowire surfaces, which significantly lowers the mean free path of phonon. This effect of reduced thermal conductivity has inspired the idea of using silicon nanowire for thermoelectrics applications [16].

Phonon transport in a system depends on the phonon ability to scatter, which can be either ballistic or diffusive. At low temperature, phonon mean free path may be larger than the sample dimensions, therefore surface scattering starts to play an important role [9, 17, 18]. This limit was studied by Casimir [19]. Casimir's model suggests that the heat flow through a system can be described by a model analogue to Planck's black-body radiation theory and Stefan Boltzmann radiation law.

Radiative phonon transport has been suggested as transport mechanism [20, 21]. The power flow with this model of phonon radiative transfer has the form $P_{\text{rad}} = A\sigma\xi T^4$, where A is the cross sectional area of the system perpendicular to the direction of heat flow, σ is the Stefan-Boltzmann constant for phonons and is given by,

$$\sigma = \frac{\pi^2 k_B^4}{120\hbar^3}\left(\frac{2}{c_t^2} + \frac{1}{c_l^2}\right) \tag{1.6}$$

where c_t and c_l are the transverse and longitudinal speeds of sound, respectively.

The factor ξ describes the transport efficiency and thus defines if the scattering is diffusive or specular [21]. For ξ=1, the phonon transport is ballistic with specular reflections from the surface. A lower limit of ξ, known as the Casimir limit, is obtained for the case of complete diffuse surface scattering [19].

The experimental measurements may be performed using different techniques, such as the 3ω [22–24] and optical thermoreflectance methods [25, 26]. The experimental data shows that thermal conductance of nanostructure is lower than its bulk counterpart. Similar trend has also been studied by theoretical works [27, 28].

1.1.3 Application of nanostructures

The design of novel structures with desirable properties is highly required for different applications. Understanding the physical properties at nanoscale becomes crucial to attain this objective. For example, carbon nanotubes could make excellent materials for application in cars, aircraft or other systems where the strength is important and the weight needs to be controlled. Thus, studies of the mechanical and chemical properties of these nanotubes are required to optimize the performance.

In addition to engineered materials that exploit nanoscale structures to reach desirable macroscopic properties, miniaturization continues to provide devices at nanometer scale in electronics and sensors. In this case, the thermal management of microelectronics becomes a challenging issue [29, 30]. Currently integrated circuits are available with transistors with small feature size around 65 nm and thin material film below 2 nm. For example, industries like ST microelectronics is working on a 28 nm road map. Such miniaturization leads to enormous integration

levels, where several transistors with more functionality are assembled together on a small area. However, operating power of the miniaturized device cannot be reduced below a certain level. The power problem, the heat generation and chip temperature increment reach a level that will impede the optimized operation of the integrated circuits.

Prevent the hot spots at a localized functional region on the chip is a main question today for the integrated circuit designers. Thus, understanding the heat generation and manipulation of heat transport at the nanoscale have significant implication for reliable functionality of nanoelectronic devices.

On the other hand, energy conversion domain can greatly benefit from energy transport phenomena at the nanoscale. For example, the effect of lower thermal conductivity at nanoscale can improve significantly the thermoelectric phenomena. A thermoelectric component converts the thermal energy into electric energy and vice versa. Thermoelectric phenomena are mainly based on the fact that electrical carries are also heat carriers at the same time. Therefore, the electron mouvement can be driven by a thermal gradient and not only by the electrical potential. The basic effects in thermoelectricity are the Seebeck and the Peltier effects [6]. The Seebeck effect is defined by how much of an electromotive force is generated when the two ends of a material are maintained under a temperature gradient. The Peltier effect is a temperature difference created by applying a current between two electrodes connected to a sample.

A key requirement to improve the energy conversion efficiency is to optimize the material thermoelectric figure of merit ZT given by:

$$ZT = \frac{S^2 \sigma}{\kappa_e + \kappa_L} T \tag{1.7}$$

related to the reduced efficiency [31] through:

$$\eta_r = \frac{\sqrt{1+ZT}-1}{\sqrt{1+ZT}+1} \tag{1.8}$$

with, S is the Seebeck coefficient, σ is the electrical conductivity, κ_e and κ_L are the electron and lattice thermal conductivity respectively. If $ZT \to \infty$, $\eta \to 1$ close to a Carnot cycle.

Thus, increasing Seebeck coefficient S and the electrical conductivity σ, while reducing κ_L are highly required. The special properties of heat transport at nanoscale leads to perform some success in the reduction of lattice thermal conductivity with the concurrent maintenance of good electrical conductivity [32, 33] .

1.2   Thermal properties

In the study of thermal properties of solids, both phonons and electrons contribute to heat capacity and thermal conductance. To extract thermal properties, phonon dispersion relations along with phonon and electronic density of states are important parameters. Moreover, the energy of phonon and electron is related to the dispersion relation through the introduction of the density of states. This section presents a theoretical illustration of the thermal properties, and then describes the specificity of the thermal properties of amorphous materials.

1.2.1   Specific heat

The heat capacity C, of a solid is defined by the temperature derivative of the internal energy U:

$$C_\alpha = \left(\frac{\partial U}{\partial T} \right)_\alpha \tag{1.9}$$

where the index α indicates the parameter which is held constant (volume or pressure). Usually, volume is held constant for solid specific heat measurement. The heat capacity of solid at constant volume is constituted by a phonon term and electron term:

$$C_v = C_{\text{ph}} + C_{\text{el}} \tag{1.10}$$

moreover, specific heat corresponds to the ratio of the amount of energy required to raise the temperature by one Kelvin for one gram of a material.

1.2.1.1   Phonon specific heat

There is different theoretical model to describe the heat capacity within a solid. It was Einstein who developed the first reasonably satisfactory theory of specific heat of a solid. He assumed that the crystal lattice structure of a solid comprising N atoms can be treated as an assembly of 3N undistinguishable one-dimensional oscillators (three oscillators for each atom since the atoms of a solid are free to move in three dimensions). Further, internal energy of solids can be seen as a sum of quantum harmonic oscillator at energy less than k_BT. All oscillators are assumed to have the same and constant frequency, Einstein's model works well at high temperature. Consequently, this theory is in good agreement with the experiment at room temperature, but provides a poor description of observations made at low temperature.

A more realistic model was given by Debye, by treating elastic vibration as a continuum with a high frequency cutoff corresponding to the interatomic distance. Indeed, at higher temperatures, higher energy levels will be excited, but one cannot excite modes whose wavelengths

are shorter than the interatomic distance. This limit implies a maximal wave vector (the Debye wave vector) $k_D^{max} = 2\pi/\lambda^{max}$, where λ_D^{max} is the interatomic distance.

According to this model, the T^3 temperature dependence of the specific heat of insulator materials is well described at low temperature.

Assuming that the internal energy is a sum of quantum harmonic oscillators satisfying Bose-Einstein statistics, U for a material is given by:

$$U = \sum_k \left(\frac{\hbar\omega(k)}{2} + \frac{\hbar\omega(k)}{e^{\frac{\hbar\omega(k)}{k_BT}} - 1} \right) \tag{1.11}$$

using the continuum hypothesis, the sum of the internal energy becomes an integral:

$$U = \int_{BZ} \frac{\hbar\omega(k)}{\left(e^{\frac{\hbar\omega(k)}{k_BT}} - 1\right)} \frac{dk}{(2\pi)^3} = \int \frac{\hbar\omega}{\left(e^{\frac{\hbar\omega}{k_BT}} - 1\right)} D(\omega)d\omega \tag{1.12}$$

the first term in Eq. 1.11 corresponds to what is known as the zero point energy. It has no temperature dependence, and thus plays no role in the specific heat. $D(\omega) = \frac{dk}{d\omega}$ is the density of state of phonon. At low temperature k_BT is small, only the long wavelengths are excited. Consequently, the integral over the first Brillouin zone (BZ) can be extended over the whole k space in three dimensions ($dk = 4\pi k^2 dk$ infinitesimal volume element). Optical modes are not populated at low temperature, then only the acoustic modes (two transverses and one longitudinal modes) contribute to the internal energy. These modes are assumed to have an average sound velocity υ_s and a dispersion relation of the form $\omega(k) = \upsilon_s k$, thus:

$$U = \frac{6}{\pi^2} \int_0^\infty \frac{\hbar\upsilon_s k^3}{e^{\frac{\hbar\upsilon_s k}{k_BT}} - 1} dk \tag{1.13}$$

assuming $x = \frac{\hbar\omega}{k_BT}$, Eq. 1.13 becomes:

$$U = \frac{3}{2\pi^2} \frac{(k_BT)^4}{(\hbar\upsilon_s)^3} \int_0^\infty \frac{x^3}{e^x - 1} dx \tag{1.14}$$

therefore, the well known Debye 3D (bulk) equation of phonon heat capacity is:

$$C_{ph} = \frac{2\pi^2}{5} \frac{k_B^4 T^3}{(\hbar\upsilon_s)^3} \tag{1.15}$$

note that the velocity of sound is the only physical characteristic of the material, where is often represented as the Debye temperature, $\theta_D = 2\pi\hbar\upsilon_s(3N/4\pi V)^{1/3}$, with N/V represents the number of phonons per cubic meter (density of phonons). Substituting these definitions into Eq. 1.14, with $x_D = \theta_D/T$ the general expression of the phonon specific heat becomes:

$$C_{ph} = 9Nk_B \left(\frac{T}{\theta_D}\right)^3 \int_0^{x_D} \frac{x^4 e^x}{(e^x - 1)^2} dx \qquad (1.16)$$

we note that the Debye temperature is a characteristic parameter related to the materials of interest.

1.2.1.2   Electronic specific heat

According to the assumptions of free electron model, there is no interaction between electrons or between electrons and lattice. These approximations can be very accurate in the simplest case of a metal. The electrons can be treated as a free electron gas. The electronic specific heat of a metal is given by:

$$C_{el} = \frac{\pi^2}{2}Nk_B\frac{T}{T_F} \qquad (1.17)$$

where, N the total number of occupied states, thus number of electrons in the system. $T_F = E_F/K_B$ is the temperature equivalent to the energy of the electrons in the highest energy state.

At low temperature (below 1 K), because of the linear power law (opposed to the T^3 law for phonon gas), electronic heat capacity becomes dominant in a metal.

1.2.1.3   Specific heat of glasses

Glass specific heat follows well the Debye model until a few tens of Kelvins, where it presents an unexpected behavior. According to the Debye model at low temperature, the specific heat of an amorphous material should be proportional to T^3. However, a linear behavior of the specific heat is shown below 1 K [34]. A similar behavior was observed for all amorphous materials with a variation within an order of magnitude for different glasses [35]. At low temperature limit, only the lowest branch of each polarization is populated. This large specific heat proves the existence of a new type of low energy state which is specific to the disorder in glasses and does not exist in pure crystals. The linear behavior of the specific heat is explained by a model taking into account the presence of two level systems (TLS) [36,37]. TLS in amorphous material is an atom or a group of atoms, which can tunnel between two minima in the configuration space.

1.2.1.4 Specific heat of nano-structured material

In thin film, when the phonon dominant wavelength becomes comparable to the thickness of the film (at very low temperature), there is a transition from 3D to a 2D phonon gas [28, 38], The heat capacity is evaluated as:

$$C_{ph} = \frac{3k_B S}{2\pi} \left(\frac{k_B T}{\upsilon_s \hbar}\right)^2 \times \left[\int_0^\infty \frac{x^3 e^x}{(e^x - 1)^2}\,dx + \sum_{n=1}^\infty \int_{nx_0}^\infty \frac{x^3 e^x}{(e^x - 1)^2}\,dx\right] \qquad (1.18)$$

where S is the surface area of the membrane and $x_0 = \pi \hbar \upsilon_s / k_B T t$, where t is the film thickness.

The first integral corresponds to the 2D phonon gas:

$$C_{2D} = \frac{9k_B^3 S T^2}{2\pi \hbar^2 \upsilon_s^2} \qquad (1.19)$$

the transition between 2D at low temperature to 3D to recover the bulk limit, is defined as a change of power law in heat capacity from T^3 for 3D to T^2 for 2D. Note that this is relevant only where $t \ll \lambda_{\text{dom}}$.

1.2.2 Thermal conductivity

In the simplest case of a one dimensional heat flow along the x axis, thermal conductivity is related to heat flow by the Fourier's law:

$$\phi = -\kappa_{ph}\frac{dT}{dx} \qquad (1.20)$$

where ϕ is the heat flow (in W/m^2) and κ_{ph} the thermal conductivity (in W/m.K). According to the Boltzmann equation and using the Fourier's law, phonon thermal conductivity is given by:

$$\kappa_{ph} = \int_0^{\omega_{max}} d\omega \int_0^{2\pi} d\varphi \int_0^\pi d\theta sin(\theta)cos^2(\theta)\hbar\tau\upsilon_x^2 \frac{df_0}{dT}\frac{D(\omega)}{4\pi} \qquad (1.21)$$

with f_0 is the equilibrium distribution function and τ is the characteristic scattering time, and $(\partial f/\partial t)_{coll} = -(f - f_0)/\tau$, is given by the relaxation time approximation. Eq. 1.21 is used to demonstrate a direct relation between the thermal conductivity and the specific heat as given by kinetic theories in Eq. 1.4.

1.2.2.1 Thermal conductivity of glasses

Amorphous solid exhibit properties that differ from the well known crystalline solid properties. The long range crystalline order does not exist in amorphous solids. The disorder destroys the coherence of lattice vibrations and thus the mean free path of phonon should be limited to a few lattice spacing at most. Consequently, the thermal conductivity in amorphous solid becomes extremely low and is often referred to as the amorphous limit[2]. Typically, the thermal conductivity of amorphous oxides fall in the range 1.3 W/mK < k < 3.0 W/mK at room temperature [39, 40]. These properties can be very useful for technological application and presents fundamental questions about the interaction of heat transfer and microstructure in this sort of material.

In general, the major distinctions between thermal conductivities of glasses and crystalline solids can be simplified in terms of lower thermal conductivities with positive temperature coefficients ($d\kappa/dT$) for glasses and negative for crystalline solids. This is in sharp contrast with the Umklapp processes[3], where the thermal conductivity for crystals decreases as 1/T due the dominant phonon-phonon Umklapp process. Whereas, in amorphous solids Umklapp processes are not allowed due to the lack of long range periodic structure. For example, at room temperature the thermal conductivity of crystalline SiO_2 is about 10 W/m.K, while that of amorphous SiO_2 is about 1 W/m.K [41]. (This is a general simplification, in some cases crystalline materials can have low thermal conductivities with positive coefficients $d\kappa/dT$).

It has been shown that the thermal conductivity κ exhibits a universal temperature dependence in several glasses (see Fig. 1.6). At low temperature (T < 1 K), κ have a positive slope, and then a plateau between 1 K and 20 K, followed by a region of positive $d\kappa/dT$ above 20 K. Below the plateau, the thermal conductivity varies as T^n, with $n \sim 2$ associated to the scattering of phonons from low lying energy states [36, 37]. In this limit, only the lowest branch of each polarization is populated. This behavior is explained by the presence of the TLS.

1.2.2.2 Thermal conductivity of nano-structured material

Thermal properties of silicon nitride membrane have been measured in various geometries by different groups [20, 43–45]. The heat flux along the SiN_x membrane depends on the quality (technique of deposition, roughness, etc..), the dimensions of the samples, and the temperature range in which the measurement is done. Thus, the phonon transport can be either diffusive or ballistic. Moreover, the measurement method plays an important role in terms of sensitivity and temperature range. For the SiN suspended membrane, there is still no measurement with high sensitivity extended from low temperature to room temperature, to describe the different diffusion regimes of phonon as function of temperature within the membrane. In the following

---

[2]The amorphous limit (or alloy limit) corresponds to a mean free path on the order of the atomic distance thus below 1 nm.

[3]If $k_3 = k_1 + k_2$ the resultant wave vector of phonon-phonon scattering ends up in other BZ, then the process is called "Umklapp process".
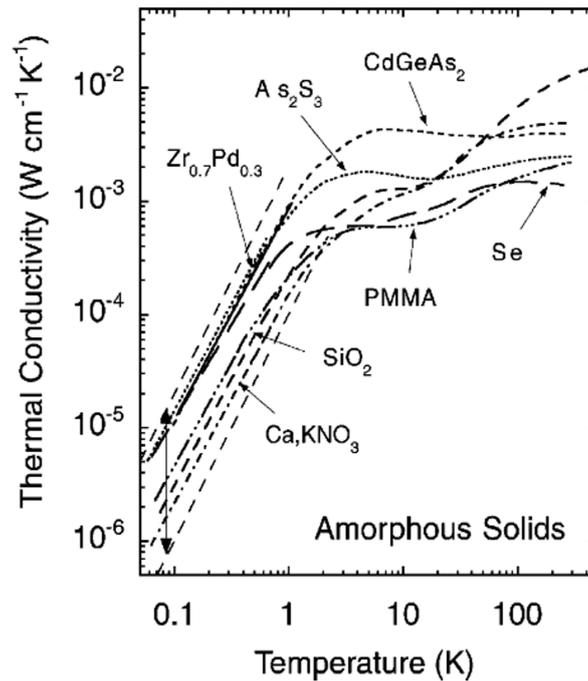
Figure 1.6: Thermal conductivity of several amorphous solids. The conductivities of all glasses measured to date below 1 K lie in the range spanned by the two dashed straight lines shown here, separated by the double arrow, which we call the glassy range [42].

section, we discuss the different diffusion limits as function of the temperature and the dimension of the sample.

1.2.3   Phonon diffusion limits in thin membrane

The heat carriers may have different behavior according to the spatial and temporal regimes in materials, which can be subdivided into four cases:

- Macroscale;

- Mesoscale;

- Microscale;

- Nanoscale.

There are two major areas in heat conduction that can be distinguished, namely:

1. The macroscale: in this regime, thermal properties are given by the bulk behavior, there is no effects linked to the surface or the size.

2. The microscale: where all the thermal properties are affected by reduced size effects.

In the study of phonons transport in finite thickness membrane, the temperature of interest has a big importance. At highly enough temperature, phonons behave like a three dimensional (3D) phonon gas. At low temperature, the phonon gas becomes quasi two dimensional (2D). The dimensionality of the phonon gas has a high influence on the properties. For example, in isotropic 3D bulk systems the phonon dispersion relation is a linear relation, $\omega = ck$. At enough low temperature, the thermal properties of the system are determined only by the acoustic phonons, where the optical modes are not excited. In this case, at low temperature ($T \ll \theta_D$), the heat capacity C_V follows the Debye model and is proportional to T^3. However, in 2D system where the mobility is restricted into a plane, only one transversal and one longitudinal mode exist and thus C_V would be proportional to T^2. In this microscopic regime, heat conduction can be governed by two important characteristic lengths. The phonon mean free path l, and the characteristic dimension to the material [46].

The phonon gas is confined in a lower dimensions than 3D, when the dominant phonon wavelength λ_{dom} becomes smaller than the system size, in the limit of very small size or low temperature. In the case of the membrane, phonon gas behaves like 3D, if λ_{dom} is much shorter than the membrane thickness. However in the opposite case, where λ_{dom} is much larger than the membrane thickness, the phonon gas becomes 2D. This change in dimensionality has direct influence on the thermal properties, it can be seen in the temperature dependence of the thermal conductance and the heat capacity.

In the following, the different limits in term of phonon mean free path are discussed, (see Fig. 1.7). When the characteristic dimension of the material is much larger than the mean phonon free path ($l \ll L$), the heat transport regime is macroscopic and is purely diffusive. Then, Fourier law is accurately applicable. When the characteristic dimension of the material is on the order or much lower than the phonon mean free path ($l \sim L$ or $l \gg L$), the heat transport regime becomes microscopic. At this limits, Fourier law breaks down and the heat transport change from a partially diffusive - ballistic to purely ballistic nature.

In the purely ballistic regime, the temperature gradient cannot be defined within the film [15]. It is impossible to describe the thermal conductivity according to the Fourier law. It was observed that the temperature at the boundaries governs the heat transport, and not the temperature gradient within the film. The heat conduction is suggested to be similar to photons, since the thermodynamic equilibrium is reestablished due to the scattering of phonon from the boundaries. Thus, they can be analyzed as a radiative transfer model where the heat flux across the film can be described by:

$$q = \sigma \left(T_1^4 - T_2^4 \right) \tag{1.22}$$
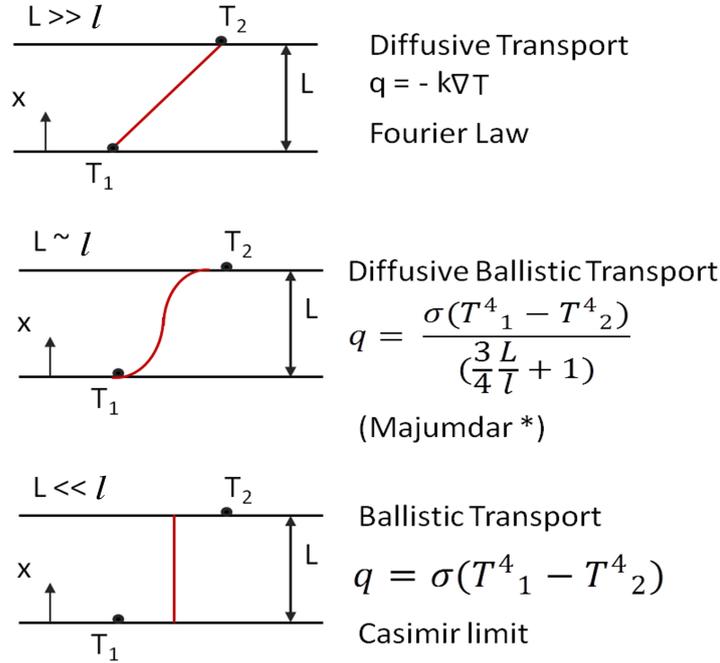
Figure 1.7: Schematic diagram showing qualitatively the steady-state temperature profiles under diffusive and ballistic phonon transport. Diffusive-Ballistic model of transport is given by Majumdar [47]

where σ is the phononic Stefan-Boltzmann constant, T_1 and T_2 are the boundaries temperature of a thin film. This is commonly referred to as the Casimir limit.

At this limit, the surface roughness plays an important role, it defines if the scattering is diffusive or specular. The effective boundary mean free path, is defined as:

$$l_{Casimir} = \frac{3}{4\pi S_c} \int \int |r - r_B| \cos\theta d\Omega dS_c \tag{1.23}$$

where S_c is the cross sectional area, $|r - r_B|$ is the distance between a point r and a surface point r_B, and θ is the angle between $|r - r_B|$ and ∇T. $l_{Casimir}$ depends on the geometry of the studied system. For example, $l_{Casimir} = 2R$ for a long circular rod of radius R and $l_{Casimir} = 1.12$ A for a long square rod of cross section A [21].

In the case of 3D ballistic phonon in a thin membrane, the radiated power has a form [27,48]:

$$P_{3D} = \frac{2ld\pi^5}{15h^3} \left(\frac{2}{c_t^2} + \frac{1}{c_l^2} \right) \left(\frac{k_B T}{\hbar} \right)^4 \tag{1.24}$$

where d is the thickness of the membrane, c_t and c_l are speeds of sound of transverse and longitudinal phonon modes. As expected from the phonon radiative model discussed above, $P \propto T^4$.

However, there is a big difference to the usual 3D bulk phonons that the purely longitudinal and transverse modes couple due to the presence of boundaries. Thus forming a new set of eigenmodes: horizontal shear modes (h) and symmetric (s) and antisymmetric (a) Lamb modes [49]. In thin membranes, the three lowest branches are dominant at low temperatures, giving the following dispersion relations [27]:

$$\omega_{h,0} = c_t k_{||}$$

$$\omega_{s,0} = 2\frac{c_t}{c_l}\sqrt{c_l^2 - c_t^2}\, k_{||} \equiv c_s k_{||}$$

$$\omega_{a,0} = \frac{\hbar}{2m^*} k_{||}^2$$

$$m^* = \hbar \left[2 c_t d \sqrt{(c_l^2 - c_t^2)/3c_l^2}\right]^{-1}$$

with d the thickness of the membrane and $k_{||}$ the component of the wave vector pointing along the membrane surfaces. Note that the lowest a–mode behaves like a particle with an effective mass m^* which means the particle-like behavior becomes stronger, when the membrane thickness decreases.

For even lower temperature or thinner membrane, phonons reach the 2D limit and the radiated power has the following form [27, 48]:

$$P_{2D} = \frac{l\hbar}{2\pi^2}\left[\left(\frac{1}{c_t^2} + \frac{1}{c_l^2}\right)\Gamma(3)\zeta(3)\left(\frac{k_B T}{\hbar}\right)^3 + \sqrt{\frac{2m^*}{\hbar}}\Gamma(\tfrac{5}{2})\zeta(\tfrac{5}{2})\left(\frac{k_B T}{\hbar}\right)^{5/2}\right] \qquad (1.25)$$

in the low temperature limit, the second term starts to dominate, and $P_{2D} \propto \left(1/\sqrt{d}\right) T^{5/2}$, because the effective mass depends on the membrane thickness.

The pure $P \propto T^4$ dependence predicted by the theory in 3D limit is not observed in suspended SiN_x membranes [44, 50]. The value of the exponent of T is systematically lower. Note that in the previous experimental studies, phonons are in the 3D limit, and no trend to reach the 2D limit have been reported. Thus, the experimental observations cannot be explained exhaustively by the radiative model, and this indicates the contribution of another scattering mechanism partly of dominantly to the heat transport.

1.3 Amorphous silicon nitride

Amorphous silicon nitride (Si_3N_4) is a material of great technological importance because of its chemical and mechanical properties. This make it very useful for several applications. It is widely used in Micro-electro-mechanical systems (MEMS) [51], bolometric millimeter wave dectectors [52] and microcalorimeters [53]. It is also often used as an etch stop in multilayered devices due to its magnificent chemical resistance. Since it is very resilient, Si_3N_4 is an ideal material for thin film growth support. Silicon micro-machining combined with nanolithography provides great possibilities for applications in calorimetry and thermometry on micron and even submicron scale. Silicon nitride allows an essential function used as thin amorphous membrane. Thus, present an excellent chance to study the phonon gas in two dimensional reduced systems, which is attracting lots of attention today.

There are different ways for the deposition of silicon nitride films, with which the properties of films can differ significantly. Current production technologies use the low pressure chemical vapor deposition (LPCVD) at temperatures > 700 °C or plasma enhanced chemical vapor deposition (PECVD) at temperatures below 450 °C. In this work, the thermal properties of silicon nitride having high and low stress deposited by (LPCVD) has been studied. In the following sections we explain the different properties specific to this kind of films.

1.3.1 Physical properties of silicon nitride

The basic atomic structure of stoichiometric amorphous silicon nitride (Si_3N_4) is a silicon-nitrogen tetrahedron in which a silicon atom lies at the centre of a tetrahedron, and four nitrogen atoms at each corner (see Fig. 1.8). The silicon atom is linked by a covalent bonds to the nitrogen atoms at the corners.
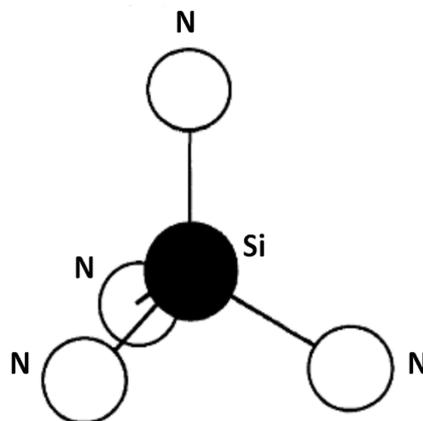
Figure 1.8: Schematic of microscopic structure of silicon nitride.

The different tetrahedrons are joined by sharing the nitogen atoms in such a way that each

one is common to three tetrahedrons. Thus, each silicon atom has four nitrogen atoms as nearest neighbours, and each nitrogen has three silicon atoms as neighbours.

Silicon nitride films properties depend essentially on the details of the fabrication process or geometry (e.g., film thickness) and measurement procedure, thus we cannot define a unique physical properties. To give an idea, Table. 1.1 shows a comparative properties of silicon nitride deposited by LPCVD and PECVD techniques. The indicated values give an order of magnitude of measured values and not necessary the maximal or minimal limits.

Table 1.1: Physical properties of Si_3N_4 LPCVD [54] and PECVD [55]

Properties	Si_3N_4 LPCVD	Si_3N_4 PECVD
Density [g.Cm^{-3}]	2.7/3.1	2/2.8
Hydrogen Concentration [10^{22} atom.Cm^{-3}]	0	1.1/3.3
Mechanical Stress [GPa]	1.2/1.8	-3/+2
Young's Modulus, E [GPa]	285	90/230

where the mechanical stress (σ) is the force per unit area that is acting on a surface of a solid, more commonly expressed in Pascals (Pa) or (N/m^2), and Young's Modulus (E) tells us how much a material is elongated under a given load. The density of PECVD SiN film is always lower than that of LPCVD (in relation with the hydrogen ratio) with a lower Young's modulus, therefore the mechanical stress can be positive or negative, contrary to LPCVD SiN which have always a positive values.

1.3.2   Technique of deposition (LPCVD)

The physical properties of silicon nitride films depend essentially on the process of deposition. LPCVD is performed at high temperature (700 - 800 K) and low pressure ($\sim$ 200 mTorr), under these conditions, a combination of volatile compounds (ammonia and dichlorosilane) are exposed to a silicon wafer. The volatiles reaction near the silicon wafer yield to create the silicon nitride film. According to the conditions of process such as, the temperature and the ratio of the volatile chemicals, the absolute magnitude of the tension can be controlled.

In this work, we study the thermal properties of silicon nitride thin film having high and low stresses. Controlling the stress into SiN film depends on the deposition process. Low stress film is produced using LPCVD recipe which dopes the film with extra nitride. Whereas, high stress silicon nitride is accomplished using a slightly modified recipe [56] which results in a stoichiometric Si_3N_4 chemistry. A tensile stress of $\sim$ 100 MPa is presented in the low stress films, whereas high stress stoichiometric films exhibit a tensile stress of $\sim$ 1.2 GPa. The included stress in our commercial high stress films is closer to $\sim$ 900 MPa.

1.4   Amorphous thin films

With recent developments of nano-structured materials such as the two-dimensional and one dimensional systems, many limits of bulk material (three dimensional) properties has been exceeded. Therefore, the measurement with high accuracy of the thermal properties becomes highly required to study the phonon transport at this reduced scale. Hence, to determine what contribution they can allow to the advancement of technology applications. In addition, amorphous solid exhibits thermal properties behaviors different than that usually seen in crystal solid, given a major asset to study this kind of materials represented here by the silicon nitride.

Typically, two dimensional structures are fabricated by depositing a thin film with the material of interest onto a thick bulk substrate. Determining the thermal properties of this film can be a challenge due to its small thickness. The substrate provides often mechanical strength for the film, consequently the film cannot be removed. Therefore, the film and the substrate must be measured together in order to extract the thermal properties of the film. In the following section, we give an overview of the challenges of the in-plane and cross-plane thermal conductivity measurements.

1.4.1   Experimental techniques

Experimental techniques to measure heat transport in thin film have improved significantly in recent years. Although there are significant advances, thermal properties measurement of thin films remains a challenging task [57].
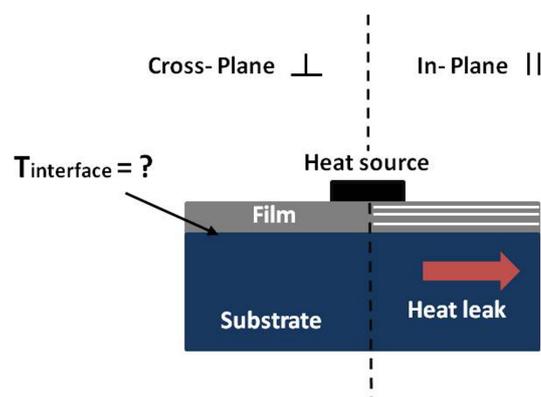
Figure 1.9: Schematic of typical sample configuration using hot strip and present challenges by the thermal conductivity measurement of thin films.

In general, for a direct measurement of the thermal conductivity, the determination of the heat flux and the temperature gradient between two points of the sample are needed. Fig. 1.9 shows the geometry typically used for the thin film thermal transport characterization. The source heater can be electrical by applying a current through a metal strip deposited on the

sample surface, and hence the Joule heating. The other method is to use an optical source to heat the film. Thus, the measurement techniques, based on heating and sensing methods can be divided on three categories: electrical heating and sensing using hot strip, optical heating and sensing methods, and combined electrical/optical methods.

According to experimental requirements, the thermal conductivity measurement can be in plane or out of plane. In general, the in plane measurement is more popular due to the assumption that the transport of heat should be more efficient when parallel to the layers. Further, advantages and limitations of used technique depend on different parameters. For instance, if a steady state method is used to measure the in-plane thermal conductivity, errors can be introduced by the parasitic heat flow through the substrate (or heat leakage). In the case where the thermal conductivity of the substrate is relatively high, heat flow through the substrate will be large as compared to the heat flow through the film. Thus, subtraction of the contribution of the substrate to the heat conduction will significantly increase the measurement errors. In addition, the thermal resistance at the interface between the film and the substrate should be taken into account. However this resistance is not easy to measure and it depends significantly on the material. Whereas, for the cross plane thermal conductivity measurement, the difficulties are exhibit by creating an adjusted temperature gradient across the film without a large increase of the substrate temperature.

To overcome these difficulties, several methods have been developed allowing the measurement of thermal properties in the different directions of the film. Fig. 1.9 shows the geometry typically used to measure thermal properties of thin films. For instance, for the cross plane measurement, by minimizing the width of the heater source, the heat flux through the film becomes large, and this reduces significantly the temperature gradient inside the substrate. Another technique consists to limit the heating to a small region within the film by using transient or modulated heating. However for the in plane direction, to minimize the heat leakage, the films can be deposited on thin and low thermal conductivity substrate. The most used technique in this case is to remove the substrate. The obtained membrane is suspended between the edges by a massive frame, which also plays the role of heat sink. Therefore, the heat flux passes only through the film. Thus, using a suspended membrane geometry is the best choice for a very sensitive experiment.

In this work we study the heat transport in amorphous silicon nitride by coupling the 3ω method to the Völklein geometry (suspended membrane). This method allows the measurement of both thermal conductance and specific heat of suspended membrane. This method will be explained in details in the next chapters 2 and 3.

Chapter 2

Implementation of the 3ω-Völklein method

In this thesis, we have been interested in studying the thermal properties of silicon nitride thin film. To attain this objective, we have developed a system designed to measure with a high sensitivity both the thermal conductance and the heat capacity of suspended membrane. This method is based on the 3ω method coupled to the Völklein geometry (suspended membrane). In order to implement this method, the transducers are connected to a Wheatstone bridge to detect the weak 3ω voltage. A lock-in amplifier is used to measure the voltage at the output of the bridge. The whole system is controlled by a computer using a LabVIEW program. In the following sections we discuss in details this method.

2.1   Principle of the 3ω method

Originally, the 3ω technique has been proposed and developed in 1910 by O. Corbino to measure the thermal diffusivity of metal filaments for use in light bulbs [58, 59]. In 1987, it was used by O. Birge and Nagel to measure frequency-dependent specific heat of a liquid [60]. It was later in 1990 [10], that Cahill has used the 3ω method to measure the thermal conductivity of dielectric solid film. Although it was initially developed to measure the thermal conductivity of bulk materials, the 3ω method has been extended later to the measurement of thin films down to 20 nm thick [14]. Further, the 3ω method has been adapted to measure the thermal conductivity of the in plane and cross plane (it is one of the most used methods) of anisotropic films [61, 62], nanowire and carbon nanotube [63, 64], liquid and gases [65], and free standing membrane geometry [24].

In principle, the 3ω method requires a thin metallic strip to be deposited onto the dielectric sample surface which serves both as a heater and thermometer as shown in Fig. 2.1. For a small temperature changes ΔT, the resistance R of the strip varies with temperature as
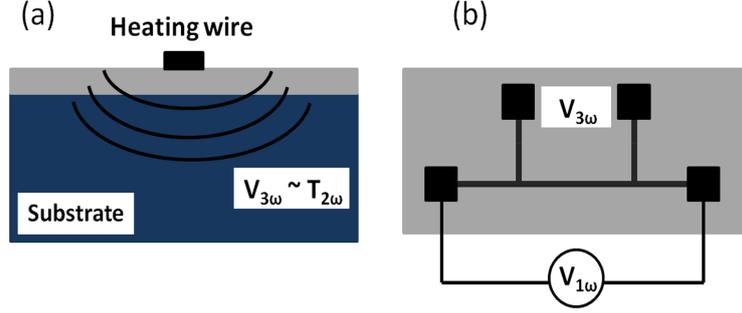
Figure 2.1:   Schematic shows (a) cross-sectional view and (b) top view of the heater/thermometer deposited on the film on substrate sample in the 3ω method.

$$R = R_0(1 + \alpha \Delta T) \tag{2.1}$$

where α is the temperature coefficient of resistance (TCR) for the metallic heater, R_0 and R are the resistances at temperatures T_0 and $T_0 + \Delta T$, respectively. Moreover, R_0 is the initial resistance where there is no heating effect. The expression of TCR is given by:

$$\alpha = -\frac{1}{R_0}\frac{dR}{dT}. \tag{2.2}$$

An ac current,

$$I = I_0 cos(\omega t) \tag{2.3}$$

with angular frequency ω and amplitude I_0 passes through the strip, generates a heating source with power:

$$P = R_0 I_0^2 cos^2(\omega t) = \left(\frac{R_0 I_0^2}{2}\right)_{DC} + \left(\frac{R_0 I_0^2 cos(2\omega t)}{2}\right)_{AC} \tag{2.4}$$

therefore, the corresponding temperature rise in the sample is also the addition of a DC component and an AC component with angular frequency 2ω, which can be given by:

$$\Delta T = \Delta T_{DC} + |\Delta T_{AC}| \, cos(2\omega t + \varphi) \tag{2.5}$$

where $|\Delta T_{AC}|$ is the amplitude of the AC temperature rise and φ is the thermal phase. ΔT_{DC} is the steady-state temperature increase due to the power dissipated by the strip.

As the resistance of the heater depends strongly on temperature, the AC temperature oscillations in the metal filament produces harmonic variations in the resistance given by

$$
\begin{aligned}
R &= R_0 \left[1 + \alpha \Delta T_{\mathrm{DC}} + \alpha \mid \Delta T_{\mathrm{AC}} \mid cos(2\omega t + \varphi) \right] \\
&= R_0(1 + \alpha \Delta T_{\mathrm{DC}})_{\mathrm{DC}} + (R_0 \alpha \mid \Delta T_{\mathrm{AC}} \mid cos(2\omega t + \varphi))_{\mathrm{AC}}
\end{aligned}
\tag{2.6}
$$

The expression of the voltage across the heater can be calculated using the current from Eq. 2.3 and the resistance from Eq. 2.6:

$$
\begin{aligned}
V = RI =& R_0 I_0 (1 + \alpha T_{DC}) cos(\omega t) \\
&+ \left(\frac{R_0 I_0 \alpha \mid \Delta T_{\mathrm{AC}} \mid}{2} cos(\omega t + \varphi) \right)_{1\omega} \\
&+ \left(\frac{R_0 I_0 \alpha \mid \Delta T_{\mathrm{AC}} \mid}{2} cos(3\omega t + \varphi) \right)_{3\omega}
\end{aligned}
\tag{2.7}
$$

According to this expression, the measured voltage across the heater contains the voltage based on the DC resistance of the heater and two components proportional to the amplitude of the temperature oscillation in the heater, at 1ω and 3ω frequencies respectively.

The 3ω voltage can be measured by a lock in amplifier and is used to determine the amplitude of the temperature of the heater:

$$
\mid \Delta T_{2\omega} \mid = \frac{2V_{3\omega}}{R_0 I_0 \alpha} \simeq \frac{2V_{3\omega}}{V_{1\omega} \alpha}
\tag{2.8}
$$

where, $V_{1\omega}$ is the applied voltage across the heater. Usually, the 3ω voltage is very small as compared to the 1ω voltage. The challenge of the 3ω method is to measure the small 3ω signal.

Moreover, to link the temperature oscillation $\mid \Delta T_{2\omega} \mid$ of the sample to the measured 3ω voltage, a heat model specific to the geometry of the sample is required. In this thesis, we used a suspended membrane geometry. Specimen preparation is explained in details in the next sections.

2.2   Specimen preparation

In this section, the fabrication methods and the measurement setup used in this work are presented. With the exception of silicon nitride film deposition which is a commercial product, all

the other steps have been done at the laboratory using clean room techniques. The suspended silicon nitride membranes, are fabricated by using optical and laser lithography. The transducers used in this work are in NbN (niobium nitride), which presents a high sensitivity; its TCR can be tailored over a wide temperature range.

2.2.1 SiN membrane preparation

The silicon nitride membranes used in this work are fabricated by using positive photolithography and anisotropic chemical etching on [100] oriented silicon wafers (of 300 or 500 μm thick) with aqueous KOH solution. In Fig. 2.2, the main steps of the fabrication process are shown. On both sides of the wafer, high or low-stress silicon nitride (Si$_3$N$_4$ thickness is 50 or 100 nm) was grown by Low Pressure Chemical Vapor Deposition (LPCVD) at LioniX BV[1]. The wafer of 4 inches is undercut on sample of 15$\times$15 mm^2. Before spreading the resist, the chip is cleaned by acetone, alcohol and deionized water and finally dried by nitrogen gas. The used photoresist is the S1818 and it was usually spun at a speed of $\sim$ 4000 rpm and baked at 150 $^\circ$C for 1 minute. Firstly, exposure was done by using a mask aligner with an UV-lamp and a plastic photomask, which has 12 rectangular windows with 1.5 mm long and 300 μm large (see Fig. 2.3). Afterward, we used Maskless Laser Lithography technology to create high quality microstructures. After exposure, the photoresist is developed with Microposit developer. Next, silicon nitride is removed from the developed areas by plasma etching in RIE using the SF$_6$ Gas, with a etching rate $\sim$ 50 nm/min. Crystalline silicon is then wet etched in 40 % KOH at 80 $^\circ$C with an etching rate of 40 μm/h, after which, the chips are cleaned in hot, deionized water, and lastly, rinsed with acetone/alcohol and dried with nitrogen gas.

2.2.2 NbN transducer deposition

The transducers are fabricated by using negative photolithography with the UV-lamp mask aligner; the transducer width was set to 15 μm. For thermometer width less than 15 μm, photolithography with photomask broke down. Thus, we used the laser photolithography for the next where the thermometer width was set to 5 μm. The measurement is performed using two transducers, the first one is centred on the membrane and is used to create an oscillation of the heat flux as well to measure the voltage oscillation at the third harmonic. The other thermometer is deposited on the bulk region of the chip; it has the same geometry and is deposited in the same run. Fig 2.3 shows two transducers used during the measurement. The transducer deposited on the bulk part of the wafer is used as a simple dependent temperature resistor in the measurement chain based on a Wheatstone bridge.

The transducers consist of niobium nitride and are grown using a dc-pulsed magnetron sputtering from a high purity (99%) Nb target in a mixture of Ar/N2 [66]. Hence, depending on the

---

[1]Micro/Nano Technology company.
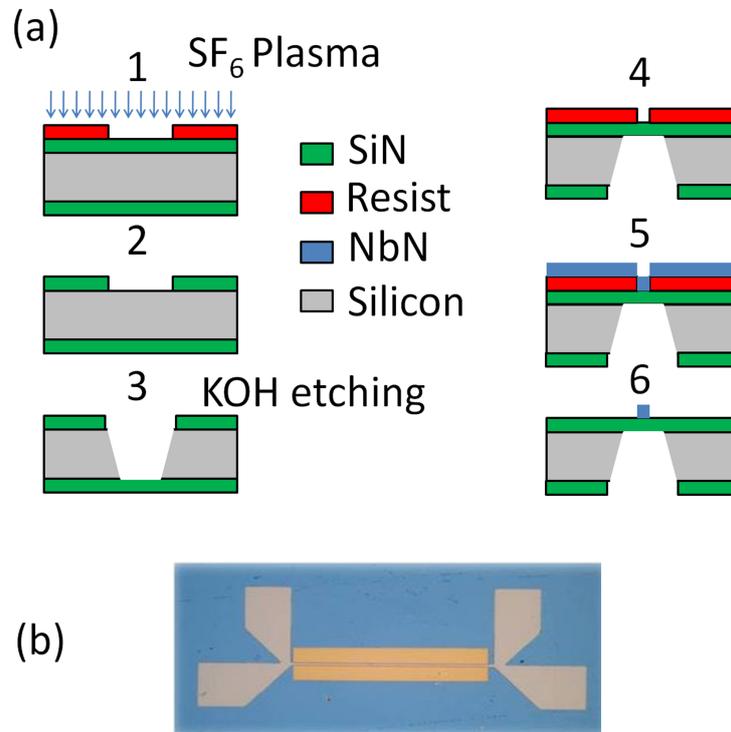
Figure 2.2: Schematic of the SiN (a) membrane fabrication. (a) (1) The patterns of the membranes are created by photolithography. (2) The nonprotected SiN is removed by SF6 RIE. (3) The silicon is anisotropically etched in a KOH solution. (4) The thermometers are obtained by a lift-off process; the area is patterned by photolithography. (5) NbN is deposited by reactive sputtering. (6) The resist and NbN layer is removed using a wet procedure. (b) A photograph of the sample is shown: the NbN is grey and the membrane is yellow (1.5 mm long, 300 μm wide and 40 nm thick).
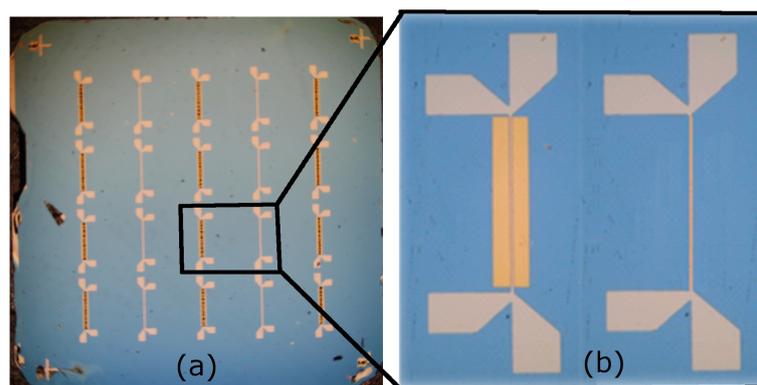
Figure 2.3: (a) Photograph shows the total chip 15x15 mm^2 with the 12 SiN suspended membranes and the reference transducers which are deposited on the same run onto the bulk region. (b) Photograph shows an example of two transducers used to perform the measurement of the thermal properties of SiN membranes.

stoichiometry, the electrical properties (electrical resistance) of the NbN can vary a lot. For the SiN thermal measurement, the thermometers have been designed for the 10 K - 300 K temperature range.

2.2.3   Specimen setup

Fig. 2.3 (a) shows an example of the chip used for the measurement. Firstly, the chip is fixed onto the sample holder (see Fig. 2.4) using photoresist and cryogenic grease to ensure a good thermal contact with the sample. Then, the transducers are connected to the sample holder pads using a micro wire bonding. Then, the sample holder is fixed on the cryostat. Lastly, a cryogenic vacuum up to 10^{-5} Torr is performed inside the cryostat to avoid any parasitic convective heat transfer with the sample. Moreover, the device is protected by a thermal copper shield maintained at the regulated temperature to limit thermal transfer by heat radiation. The thermal gradient between the thermal shield and the sample has been estimated to be much less than 1K, it is given by the temperature oscillation ΔT of the transducer. The equivalent parasitic thermal conductivity is calculated using the Stefan-Boltzmann law is less than 10^{-7}W/m.K.
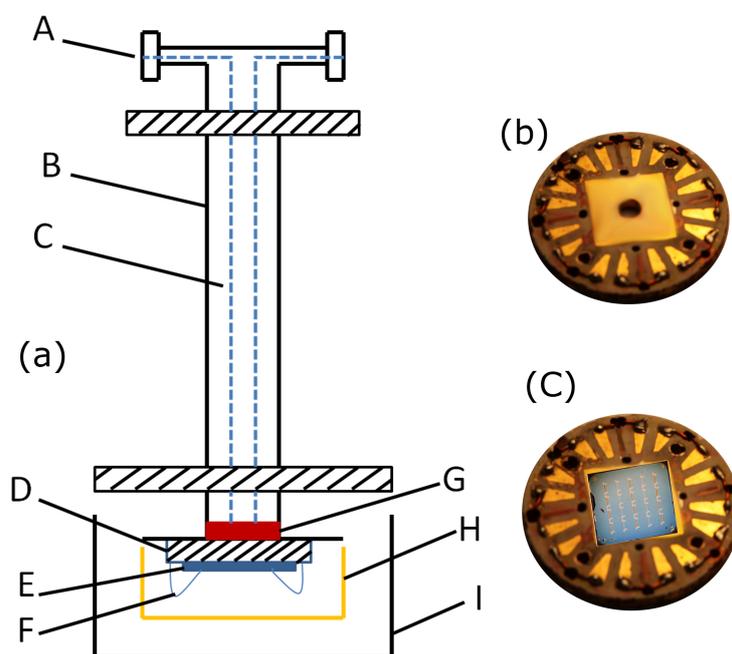
Figure 2.4: (a) Schematic shows the cryostat used to perform the measurement, A: Feed through for the electric leads; B: stainless steel tube; C: connection wires; D: sample holder; E: the chip of 15x15 mm; F: wires of bonding; G: regulated stage; H: thermal copper shield; I: external shield. (b) Photograph shows the sample holder. (c) Photograph shows the chip fixed on the sample holder.

2.3   Electrical setup

In order to link up the transducers to the measurement chain, contact pads are patterned at both ends of the strip. The transducer is patterned is such manner to have four pads in order to disjoint the current and voltage leads, and then to reduce the connection wire contribution. The ac current through the transducer deposited on the membrane, induces temperature oscillations of the membrane with an angular frequency 2ω. Consequently, the thermometer resistance varies with the same angular frequency. Therefore due to the thermal oscillations, the measured voltage contains a new "thermal" AC component which varies with an angular frequency 3ω. This $V_{3\omega}$ voltage depends on the geometry, the thermal conductance, and the heat capacity of the membrane. However, the $V_{1\omega}$ signal is still present and is much larger than the $V_{3\omega}$ signal by a factor of 10^3 to 10^5. In the following, we explain how by using a specific Wheatstone bridge [60], we strongly reduce the component of the measured voltage at angular frequency 1ω.
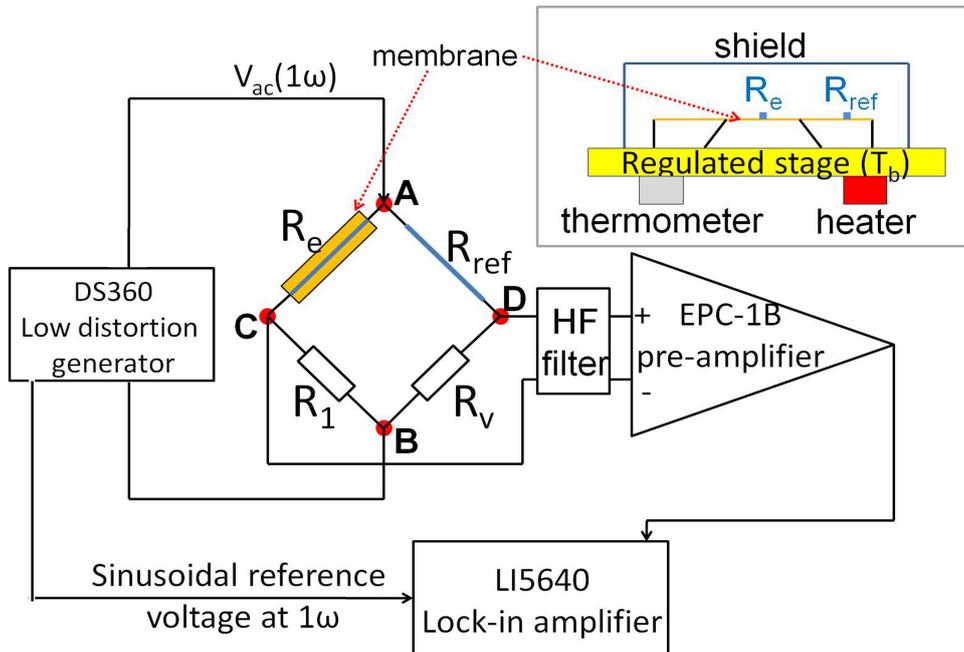
Figure 2.5: Schematic of the electrical measurement system including HF filter, preamplifier, and lock-in amplifier. A, B, C, and D represent the nodes of the Wheatstone bridge. The $V_{3\omega}$ is measured between C and D. The transducer is referred to as R_e and the reference resistance as R_{ref}. The inset presents a schematic of the membrane fixed on the temperature regulated stage covered by the thermal copper shield.

The Wheatstone bridge consists of the measured sample with a resistance R_e, which is the NbN thermometer on the SiN membrane, the reference thermometer R_{ref}, an adjustable resistor R_v, and an equivalent nonadjustable resistor $R_1 = 50$ KΩ as schematized in Fig. 2.5. The adjustable resistor is an IET-488 programmable resistor with a resolution of 1mΩ, an accuracy of 0.1% and it can be controlled by an Labview program. During the experiment, the Wheatstone

bridge is balanced at each temperature of measurement via R_v.

The heating current is generated by applying an alternative voltage V_{ac} between A and B with the oscillation output of the DS 360 low distortion generator. The measured voltage is frequency filtered (for f ≥ 50 kHz) and preamplified by a factor of 100 with a low noise preamplifier EPC-1B[2].

The reference thermometer (or reference transducer) has the same geometry and is deposited in the same run as the transducer on the membrane. The two resistors R_v and R_1 are positioned outside the cryogenic system. If $R_e = R_{ref}$ and $R_1 = R_v$, the electrical potential at angular frequency 1ω is the same in C and D. Consequently, there is no voltage at the angular frequency of 1ω between C and D. Since the reference thermometer is not on the membrane, its temperature remains at T_b (bath temperature) and therefore, its resistance does not change. The elevation of temperature of the reference transducer has been estimated to be less than 10^{-6}K for a dissipated power in the order of 1μW at room temperature [67]. Thus this elevation is neglected, thanks to the infinite reservoir of the bulk silicon as compared to the membrane.

In that geometry, the voltage at 1ω ($V_{1\omega}$) has been reduced by a factor of 10^3. For instance, with a thermometer of resistance $R_e \sim 70$ KΩ at room temperature, an applied ac voltage $V_{ac} =$ 0.39 V of a frequency f = 4.67 Hz, the measured 1ω and 3ω voltage on the Wheatstone bridge output are respectively $V_{1\omega} = 0.14$ mV and $V_{3\omega} = 0.03$ mV. However, without the Wheatstone bridge, the measured voltage equal to the applied voltage, $V_{1\omega} = 0.39$ V. Therefore, the 1ω is reduced by a factor more than 2×10^3 in the presence of the Wheatstone bridge. Note that the 3ω voltage is directly proportional to the TCR, thus it is very small at room temperature. The balancing of the Wheatstone bridge will be explained in details in section 2.4.2.

2.3.1   Lock in amplifier

Lock-in amplifier is designed to detect and measure (in the presence of large amount of noise) a very small AC signals in the range down to a few nanovolts. Since the 3ω voltage is much smaller than the fundamental 1ω voltage, lock-in amplifier is used to detect and measure both the amplitude and the phase. Here, the Ametek 7124 is used to measure simultaneously the dual harmonics 1ω and 3ω.

The technique commonly used to attain this objective is called phase-sensitive detection (PSD), which separates the components of the input signal at a specific reference frequency and phase. Phase-sensitive detectors (PSD) requires a frequency reference to which it "locks-in". The reference signal can be generated either internally by the lock-in internal oscillator, or externally through a function generator. As the 3ω voltage is very small and is proportional to V_{ac}^3 as we will see later, the input current should be as perfect as possible. In these measurements, the DS 360 low distortion function generator was used as external generator. The DS 360 deliv-

---

[2]EPC-1B is a preamplifier developed at the Institut Néel with an input noise around 1 nV/$\sqrt{\text{Hz}}$ between 1 Hz and 1 kHz

ers signals with total harmonic distortion (THD) less than 0.001 % with a frequency accuracy of 25 ppm. Note that the Wheatstone bridge have the advantage to remove the different harmonics which do not have a thermal origin, this is true when it is well balanced.

If the sine output from the function generator with the frequency ω_r is used to excite the experiment, thus the response is defined as followed:

$$V_{sig}sin(\omega_r t + \theta_{sig}) \tag{2.9}$$

where, V_{sig} and θ_{sig} are the signal amplitude and the signal phase respectively. Due to orthogonality of sinusoidal signals of different frequencies to each other, the average of the product of two signal components is zero unless their frequencies are the same. Thus, by multiplying a noisy signal from the experiment by a reference signal at given frequency ω_L generated by the lock-in amplifier as $sin(\omega_L t + \theta_{ref})$, the product is proportional to the noisy signal at that frequency and is given by:

$$V_{psd} = V_{sig}sin(\omega_r t + \theta_{sig})sin(\omega_L t + \theta_{ref}) \tag{2.10}$$

where, V_{psd} is the phase sensitive detection output. Using product to sum trigonometric identities, the product can be given by:

$$V_{psd} = \frac{1}{2}V_{sig}\left[cos[(\omega_r - \omega_L)t + (\theta_{sig} - \theta_{ref})] - cos[(\omega_r + \omega_L)t + (\theta_{sig} + \theta_{ref})]\right] \tag{2.11}$$

as shown in equation 2.11, by adjusting the lock-in frequency to be same as the reference one ($\omega_L = \omega_{sig}$), and by applying a low pass filter to the PSD output, the AC signals will be removed. As a result, the output of the PSD yields a DC signal as follows:

$$V_{psd} = \frac{1}{2}V_{sig}cos(\theta_{sig} - \theta_{ref}). \tag{2.12}$$

However, to determine the magnitude of the signal, the out of phase component of the signal with the reference will be measured. To attain this objective, a second DSP is used with a reference signal phase angle of $\pi/2$ from the first. Then by combining the two components, the magnitude and phase angle can be obtained:

$$V_{psd2} = \frac{1}{2}V_{sig}cos[\theta_{sig} - (\theta_{ref} + \pi/2)] = \frac{1}{2}V_{sig}sin(\theta_{sig} - \theta_{ref}) \tag{2.13}$$

and then,

$$R = \sqrt{V_{psd}^2 + V_{psd2}^2}$$
$$\theta = \theta_{sig} - \theta_{ref} = tan^{-1}\left(\frac{V_{psd}}{V_{psd2}}\right) \tag{2.14}$$
$$V_{psd} \equiv V_x$$
$$V_{psd2} \equiv V_y$$

where R is the magnitude of the signal, and θ defines the phase between the signal and the lock-in reference.

2.4   Experimental procedure

In order to extract thermal properties of silicon nitride membrane, there are different independent measurements that need to be achieved. First of all, the calibration of transducers versus temperature, which leads to determine the law of variation of the resistance with temperature, and permits to calculate the temperature coefficient of resistance of thermometer. Then the 3ω voltage is measured to estimate the temperature oscillation at 2ω of the thermometer as shown in Eq. 2.8. This measurement is realized in two steps. One at low frequency and another by a scan with the frequency at a given temperature, to finally reach the value of the thermal conductivity and the specific heat respectively. In the following we show a detailed explanation of these measurements.

2.4.1   Thermometer calibration and TCR measurement

The thermometer constitutes the key element in thermal measurement. The accuracy of the measured thermal properties depends essentially on the temperature sensitivity and stability of this element. By definition, a thermometer has some physical properties which depends strongly on the temperature. In the case of resistive thermometry used in these experiments, the physical property is the electrical resistance of the thermometer. The temperature coefficient of resistance TCR in K^{-1} expresses the sensitivity of the resistive thermometer, and symbolizes the resistance change factor per degree of temperature change as mentioned by Eq. 2.2.

The TCR is principally related to the intrinsic properties of the transducer. Metals have positive TCR, where the resistance varies linearly with temperature and generally saturates around 30 K, so metals cannot be used at low temperatures. However, semiconductors and materials

with a Mott-Anderson transition have negative temperature coefficients, making them partic-
ularly effective at low temperatures. At low enough temperature, the Mott-Anderson material
(e.g NbN [66], NbSi [68, 69]) becomes insulating, with an exponential increase in their resis-
tance. Therefore, the Mott-Anderson insulator materials are the most useful for low temperature
thermometric applications.

As mentioned above, the NbN transducers are used in these experiments. This kind of
transducers has a big advantage, where its TCR reaches 10^{-1} K^{-1} at low temperature and 10^{-2}
K^{-1} at room temperature, a high values as compared to regular thermometer like platinum
($\sim 0.4 \times 10^{-2}$ K^{-1} at room temperature). Moreover, it can be tailored over a wide temperature
range, from low temperature [9] to high temperature [70]; this cannot be done with NbSi, a less
versatile material.

In order to get access to the TCR of thermometer, the resistance of the thermometer should
be measured versus temperature. This calibration will serve also to calculate the thermal proper-
ties. To attain this objective, the resistance of the thermometer is calibrated using a standard four
probe technique between 4 K and 330 K in a ^{4}He cryostat. This connection configuration allows
spatial separation of the current and voltage leads, so that one can extract only the resistance of
the thermometer, without including the contribution of the connecting wires in the final value
of the resistance. This configuration is very widely used in thermometry because it provides a
highly reliable and reproducible low noise measurement. Fig. 2.6 shows an experimental data
of a thermometer calibration, and the respective TCR versus temperature.
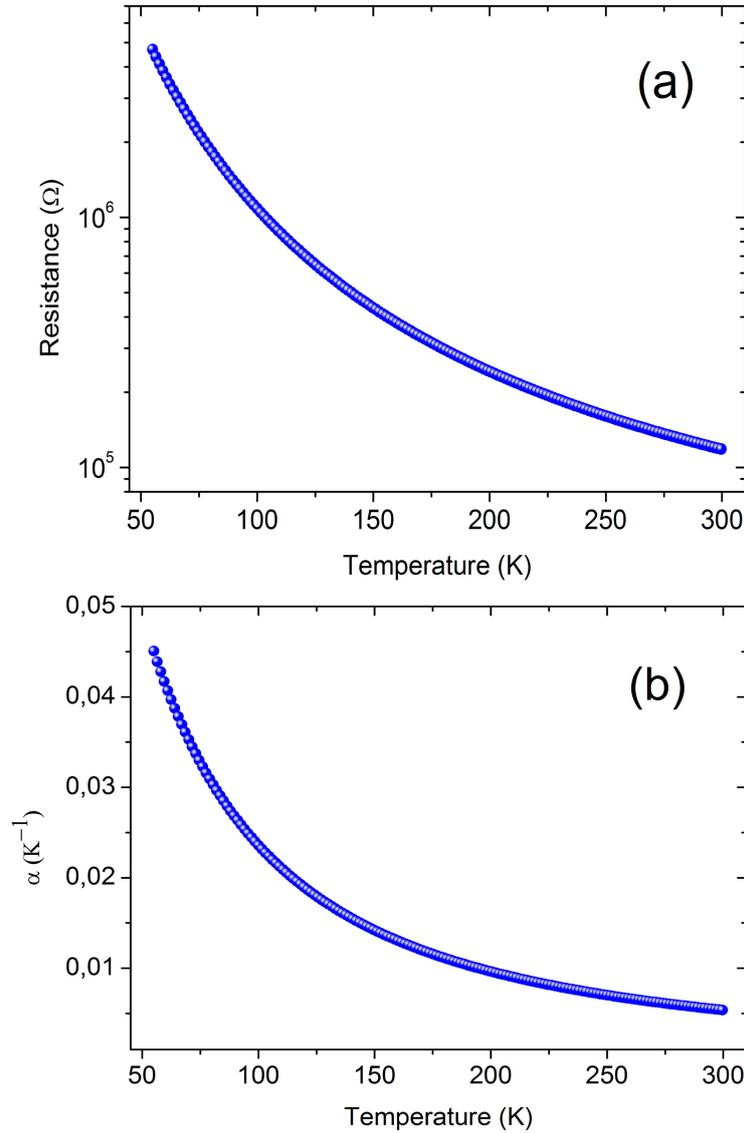
Figure 2.6: Evolution of the resistance (a) and the temperature coefficient of resistance (b) of the thermometer R_e versus temperature.

2.4.2 Wheatstone bridge balance and $V_{3\omega}$ expression

The two NbN thermometers have practically the same temperature behavior as they have been deposited simultaneously on the SiN substrate. However, due to the presence of inhomogeneity in the deposition process, there is a slight difference of resistance. Thus, the R_v resistor is used to balance the bridge. However, the measured $V_{1\omega}$ between C and D will never be equal to zero after balancing the bridge. As shown in Fig. 2.7, $V_{min} \neq 0$. Note that this voltage depends on temperature, corresponds to the thermal 1ω signal generated by the thermometer as given by Eq. 2.7, to the parasitic voltage corresponding to the resistance of contacts and to the electrical capacities by the terms $R_1 C'_4$, $R_v C'_3$ as given by Eq. 2.15.
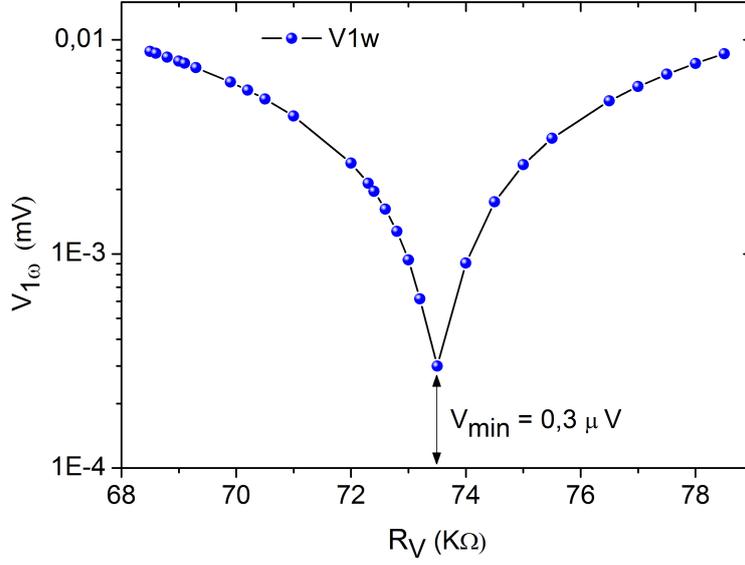
Figure 2.7: $V_{1\omega}$ versus R_v measured between C and D. This measurement is performed at T= 150 K, with V_{ac} = 1 V and f = 7.56 Hz.

The heating current is generated by applying an alternative voltage V_{ac} between A and B with the oscillation output, $V_{ac}e^{j\omega t}$. As the distance between the thermometer and the resistances R_v and R_1 is not negligible, we assume that there is line electrical capacities (C_l) in parallel, as schematized on the Fig. 2.8. We assume also that the two thermometers present an electrical capacity: $C'_3 = 2C_l + C_3$ for the reference and $C'_4 = 2C_l + C_4$ for the sample. Following the schemes given in Fig. 2.8, the absolute value of $V_{1\omega}$ between C and D can be written as follows:

$$|V_{1\omega}(\omega)| = \frac{V_{ac}\left[\varepsilon^2 + R_e^2 R_{ref}^2 \omega^2 (R_1 C'_4 - R_v C'_3)^2\right]^{1/2}}{\left[(R_v + R_e)^2 + (R_v R_e C'_3 \omega)^2\right]^{1/2}\left[(R_{ref} + R_1)^2 + (R_1 R_{ref} C'_4 \omega)^2\right]^{1/2}} \tag{2.15}$$

with $\varepsilon = R_{ref}R_1 - R_e R_v$ and the phase $\varphi_{V1w}(\omega)$ given by $\varphi_{V1w}(\omega) = \varphi_3 - \varphi_4 - \varphi_5$ where :

$$tg\varphi_3 = \frac{R_{ref}R_e(R_1 C'_4 - R_v C'_3)\omega}{R_1 R_{ref} - R_e R_v} \qquad tg\varphi_4 = \frac{R_v R_{ref}C'_3\omega}{R_{ref} + R_v} \qquad tg\varphi_5 = \frac{R_1 R_e C'_4 \omega}{R_e + R_1} \tag{2.16}$$

Moreover, the measured voltage between C and D can be given by:

$$V_{CD}(t) = V_{AD}(t) - V_{AC}(t) \tag{2.17}$$

As the temperature elevation of the reference thermometer is neglected, thanks to the infinite reservoir of the bulk silicon as compared to the membrane; thus there is no term at 3ω coming from $V_{AD}(t)$.
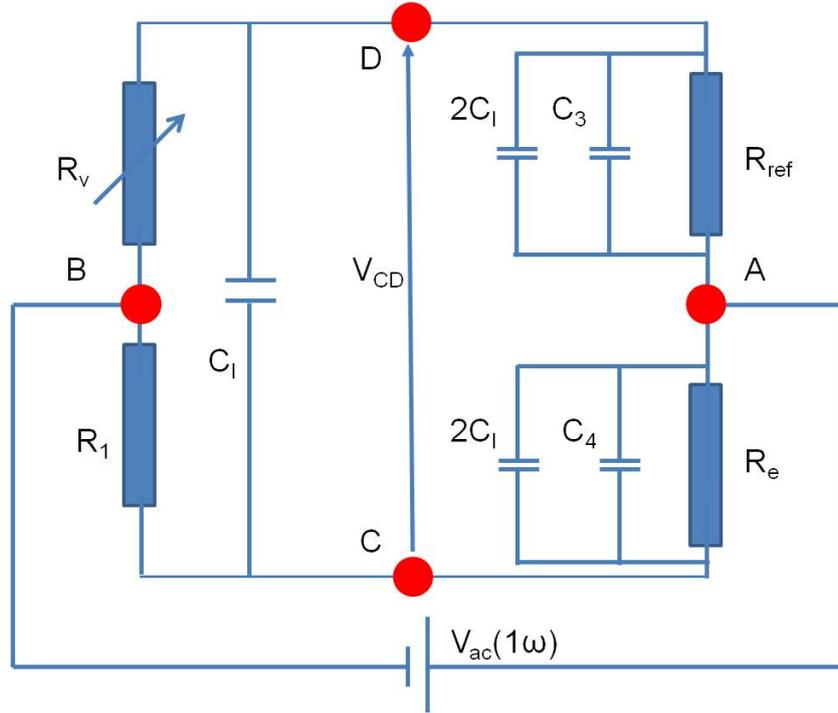
Figure 2.8: Electrical schematic of the Wheatstone bridge. V_{CD} is the output measured voltage.

The expression of the voltage drop across the thermometer, $V_{AC}(\omega)$ is given by:

$$V_{AC}(\omega) = Z_e I \tag{2.18}$$

with $Z_e = R'_e / (1 + jR'_e C'_4 \omega), \quad R'_e = R_e \left[1 + \alpha \left| \triangle T_{2\omega} \right| cos\left(2\omega t + \varphi \right) \right]$

$\left| \triangle T_{2\omega} \right|$ is the average of temperature oscillation at 2ω of the membrane, I the current coming through the impedance Z_e, and Z_e represents the ac impedance of the thermometer including the electrical leads.

$\left| \triangle T_{2\omega} \right|$ depends on the geometry of the membrane and its thermal properties, it will be calculated later by an appropriate thermal transfer model.

Using the relations between the currents in the Wheatstone bridge, we can obtain the following equation:

$$I = \frac{V_{ac} \left(1 + jR_e C'_4 \omega \right)}{\left(R_1 + R_e + jR_e R_1 C'_4 \omega \right)} \tag{2.19}$$

Then, the general expression of the voltage, between A and C, can be written as follows:

$$V_{AC}(t) = \frac{\sqrt{2}V_{ac}^{rms}R_e\left[1+\alpha\left|\triangle T_{2\omega}\right|\cos\left(2\omega t+\varphi\right)\right]\cos(\omega t-\varphi_5)}{\left(\left[R_1+R_e\left[1+\alpha\left|\triangle T_{2\omega}\right|\cos\left(2\omega t+\varphi\right)\right]\right]^2+\left[R_1R_eC_4'\omega\right]^2\right)^{1/2}} \quad (2.20)$$

with V_{ac}^{rms} the voltage put on the Wheatstone bridge (between A and B),φ the thermal phase, C_l the line capacity, C_3 and C_4 being the electric capacity of the reference thermometer and of the thermometer on the membrane respectively.

After development in Taylor expansion of the denominator of Eq. 2.20, the rms value of the 3ω voltage $V_{3\omega}^{rms}$ is given by:

$$V_{3\omega}^{rms}(\omega) = \frac{V_{ac}^{rms}\alpha R_e\left|\triangle T_{2\omega}\right|}{2}\left[\frac{1}{\left[(R_1+R_e)^2+(R_1R_eC_4'\omega)^2\right]^{1/2}}-\frac{R_e}{(R_1+R_e)^2}\right] \quad (2.21)$$

Fig. 2.9 shows an experimental measurements of both the voltage and the phase of the 1ω voltage, and their respecting fits using Eqs. 2.15 and 2.16 to determine C_3' and C_4'. An electrical cutoff frequency is observed at 1 kHz, whereas the thermal cutoff frequency is observed around 100 Hz which is much lower than the electrical cutoff frequency.
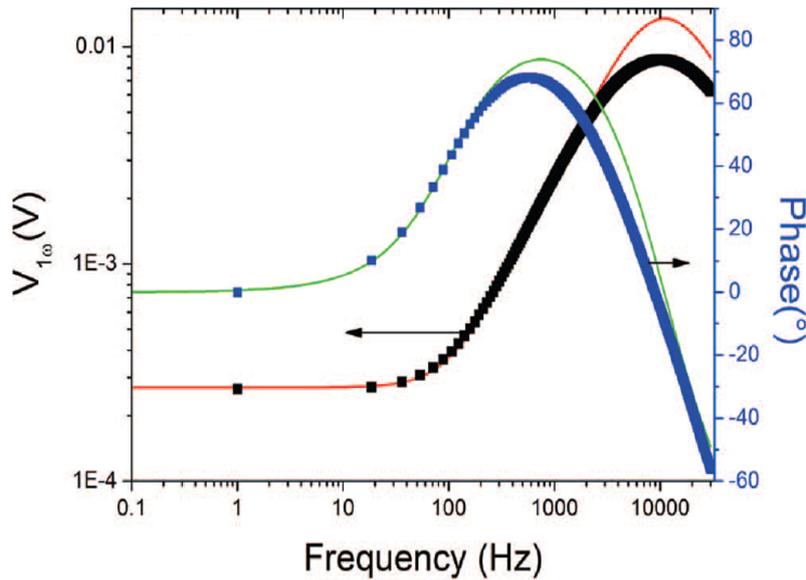
Figure 2.9: Absolute value and phase of $V_{1\omega}$ signal as a function of the frequency and their respecting fits (solid lines) using the following parameters: V_{ac}^{rms} = 0.06 V, R_v = 70.5 KΩ, R_e = 267.81 KΩ R_{ref} = 390.77 KΩ, C_3' = 185 pF, and C_4' = 450 pF.

Therefore, the electrical capacities of the thermometers are negligible as compared to the thermal effects. Thus, in order to give a clearer and more physical description of the method, we can consider that $C_3'=C_4'=C_l=0$. Then the expression of $V_{3\omega}$ becomes:

$$V_{3\omega}^{rms}(\omega) = \frac{V_{ac}^{rms}\alpha R_e \left| \triangle T_{2\omega} \right|}{2} \frac{R_1}{(R_1 + R_e)^2} \qquad (2.22)$$

After the specimen reaches thermal equilibrium and the Wheatstone bridge is balanced, the magnitude and phase of the 3ω voltage are measured between C and D by the lock-in amplifier. As shown in Eq. 2.22, the magnitude of the 3ω voltage depends on the temperature oscillation of the membrane $\left| \triangle T_{2\omega} \right|$. Moreover, the expression of $\left| \triangle T_{2\omega} \right|$ depends on the geometry of the membrane and contains its thermal properties such as the thermal conductance and the heat capacity.

In the following chapter, we present the thermal model of heat transfer across the membrane used to calculate $\left| \triangle T_{2\omega} \right|$. Then we explain how through an approximation of Eq. 2.22 at low and high frequency one can extract the thermal conductance and the heat capacity respectively.

Chapter 3

Heat transfer model and data treatment

The thermal properties of the membrane are related to the 3ω voltage through the temperature oscillation as shown by Eq. 2.22. In this chapter, we will provide the heat transfer model specific to the suspended membrane geometry. The analytical solution of the temperature oscillation for a 2-dimensional model is first derived. Then to simplify, the 1-dimensional solution is derived using some assumptions. The difference between the two models on the extracted thermal properties will then be presented. Afterwards, the effect of a finite transducer width will be discussed. Finally in order to validate the 3ω-Völklein method, we present experimental measurements fitted by the theoretical model, the sensitivity of this method will be discussed.

3.1   Two dimensional model

Consider the geometry shown in Fig. 3.1. The thin membrane is supported by the substrate. The geometry of the membrane is assumed to be rectangular with the dimensions 2ℓ and L. The thickness of the membrane is e. The heater/thermometer of width w and height h is patterned in the centre of the membrane. The heater width w is small as compared to membrane width (on the order of $1/60$), and the heat transfer within the heater may be neglected (which can be calculated using the Wiedmann-Franz law). Thus, the heater may be treated as a line source of heat. A sinusoidal electric current of amplitude I and frequency ω passes through the heater. The electrical resistance of the metal heater is R. As the measurement is performed under a cryogenic vacuum and the sample is protected by a thermal shield, convection and radiation are negligible compared to conduction in the membrane plane. Further, the out of plane thermal resistance is assumed to be small compared to the in plane thermal resistance, thus the membrane may be treated as isothermal is the z-direction. This will be confirmed by a numerical simulation of the system by finite element analysis (see Fig. 3.5).
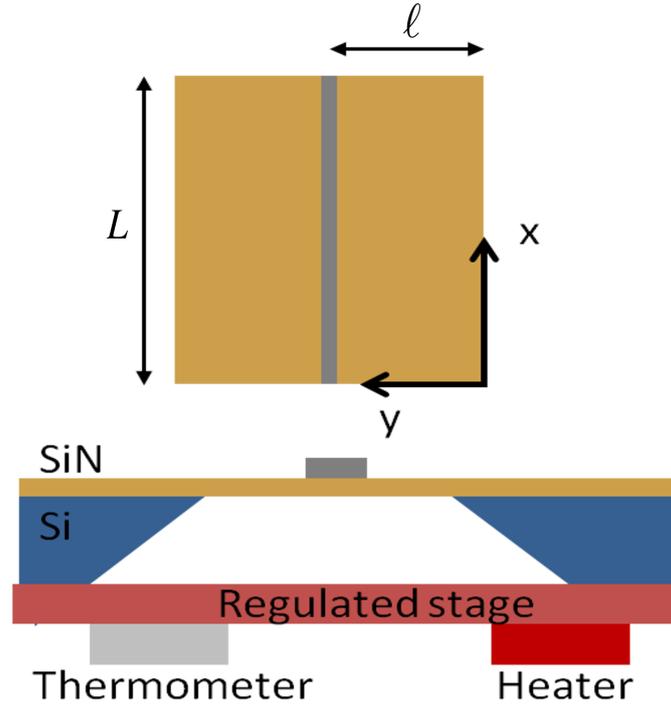
Figure 3.1: Schematic showing the geometry of the freestanding thin film installed on the controlled temperature stage.

3.1.1 General equation of heat transfer

Under these assumptions, the equation of heat transfer through the membrane may be written as:

$$\frac{\partial^2 T}{\partial x^2} + \frac{\partial^2 T}{\partial y^2} = \frac{1}{D}\frac{\partial T}{\partial t} \tag{3.1}$$

where $D = \frac{\kappa}{\rho c}$ is the thermal diffusivity, κ is the thermal conductivity, ρ is the density and c is the specific heat.

The initial and boundary conditions for Eq. (3.1) may be written as:

$$\begin{cases} T(x,y,0) = 0 \\ T(0,y,t) = T(L,y,t) = T(x,0,t) = 0 \\ \left.\frac{\partial T}{\partial y}\right|_{y=\ell} = \frac{RI^2 sin^2(\omega t)}{2\kappa s} = \frac{RI^2}{4\kappa s}[1 - cos(2\omega t)] \end{cases} \tag{3.2}$$

where $s = eL$ is the cross section of the membrane.

In order to solve this differential equation, we assume that the solution is the sum of a steady-state component $U_{ss}(x,y)$ corresponding to the steady component of Joule heating due to sinusoidal current, and a transient component $V_{tr}(x,y,t)$ that consists of the time dependent and sinusoidal terms.

Thus, the general solution of Eq. 3.1 can given by:

$$T(x,y,t) = U_{ss}(x,y) + V_{tr}(x,y,t) \tag{3.3}$$

for the next, we will use U and V instead U_{ss} and V_{tr} respectively. The initial and boundary conditions can be written as:

$$\begin{cases} V(x,y,0) = 0 \\ U(0,y) + V(0,y,t) = 0 \\ U(x,0) + V(x,0,t) = 0 \\ U(L,y) + V(L,y,t) = 0 \\ \left.\frac{\partial U}{\partial y}\right|_{y=\ell} + \left.\frac{\partial V}{\partial y}\right|_{y=\ell} = \frac{RI^2}{4\kappa s} - \frac{RI^2}{4\kappa s}cos(2\omega t) \end{cases} \tag{3.4}$$

$$\Rightarrow \begin{cases} V(x,y,0) = 0 \\ U(0,y) = 0, \, V(0,y,t) = 0 \\ U(x,0) = 0, \, V(x,0,t) = 0 \\ U(L,y) = 0, \, V(L,y,t) = 0 \\ \left.\frac{\partial U}{\partial y}\right|_{y=\ell} = \frac{RI^2}{4\kappa s}, \, \left.\frac{\partial V}{\partial y}\right|_{y=\ell} = -\frac{RI^2}{4\kappa s}cos(2\omega t) \end{cases} \tag{3.5}$$

moreover, Eq. 3.1 becomes:

$$\begin{aligned} \frac{\partial^2 U}{\partial x^2} + \frac{\partial^2 U}{\partial y^2} &= 0 & \text{steady state (ss)} \\ \frac{\partial^2 V}{\partial x^2} + \frac{\partial^2 V}{\partial y^2} &= \frac{1}{D}\frac{\partial V}{\partial t} & \text{transient (tr)} \end{aligned} \tag{3.6}$$

3.1.1.1 General solution of steady-state equation

The solution of the steady-state component can be determined using the method of separation of variables. We can assume that the solution is given by:

$$U(x,y) = X(x)Y(y) \tag{3.7}$$

by substituting Eq. 3.7 into the steady-state part of Eq. 3.6 we obtain:

$$
\begin{aligned}
X''Y + XY'' &= 0 \\
\frac{X''}{X} + \frac{Y''}{Y} &= \pm\lambda^2
\end{aligned}
\tag{3.8}
$$

where λ is a constant.

the solution of Eq. 3.8 can be given by:

$$
\begin{cases}
X(x) = A\cos(\lambda x) + B\sin(\lambda x) \\
Y(y) = C\cosh(\lambda y) + D\sinh(\lambda y)
\end{cases}
\tag{3.9}
$$

where, A, B, C and D are constant coefficients which are determined using the boundary conditions given by Eq. 3.4. Thus we find:

$$
\begin{cases}
A = C = 0 \\
B\sin(\lambda L) = 0 \Rightarrow \lambda L = n\pi \Rightarrow \lambda_n = \frac{n\pi}{L}
\end{cases}
\tag{3.10}
$$

with n an integer number. The steady-state solution becomes:

$$
U(x,y) = \sum_{n=0}^{\infty} E_n \sin(\lambda_n x)\sinh(\lambda_n y)
\tag{3.11}
$$

with E_n a constant coefficient to be determined, $\left.\frac{\partial U}{\partial y}\right|_{y=\ell} = \frac{RI^2}{4\kappa s}$ implies:

$$
\sum_{n=0}^{\infty} E_n \lambda_n \sin(\lambda_n x)\cosh(\lambda_n \ell) = \frac{RI^2}{4\kappa s}
\tag{3.12}
$$

by multiplying the two sides of Eq. 3.12 by:

$\int_0^L \sin(\lambda_m x)dx$ one obtains:

$$
\int_0^L E_n \lambda_n \sin(\lambda_n x)\sin(\lambda_m x)\cosh(\lambda_n \ell)dx = \int_0^L \frac{RI^2}{4\kappa s}\sin(\lambda_m x)dx
\tag{3.13}
$$

the left side of Eq. 3.13 is different of zero only if $n = m$, thus:

$$\int_0^L E_n\lambda_n sin^2(\lambda_n x)cosh(\lambda_n \ell)dx = \int_0^L \frac{RI^2}{4\kappa s}sin(\lambda_n x)dx \tag{3.14}$$

$$E_n = \frac{RI^2[1-cos(\lambda_n L)]}{2\kappa e(n\pi)^2 cosh(\lambda_n \ell)} \tag{3.15}$$

then the solution of the steady-state equation becomes:

$$U_{ss}(x,y) = \sum_{n=1}^{\infty} \frac{RI^2[1-cos(n\pi)]}{2\kappa e(n\pi)^2 cosh(\frac{n\pi \ell}{L})}sin(\frac{n\pi}{L}x)sinh(\frac{n\pi}{L}y). \tag{3.16}$$

U_{ss} represents the average heater temperature rise due to Joule heating. Note that this equation can be used to determine the thermal conductivity of the membrane, as κ is the only unknown parameter. Here we will use it to determine the profile of the steady state temperature elevation of the membrane. This is a convergent series, we find that the first tens orders are sufficient and do not need to go to higher orders. Fig. 3.2 shows U_{ss} at room temperature for a dissipated power of 1 μW, the temperature elevation on the centre of the membrane is $\Delta T \sim 40$ mK.
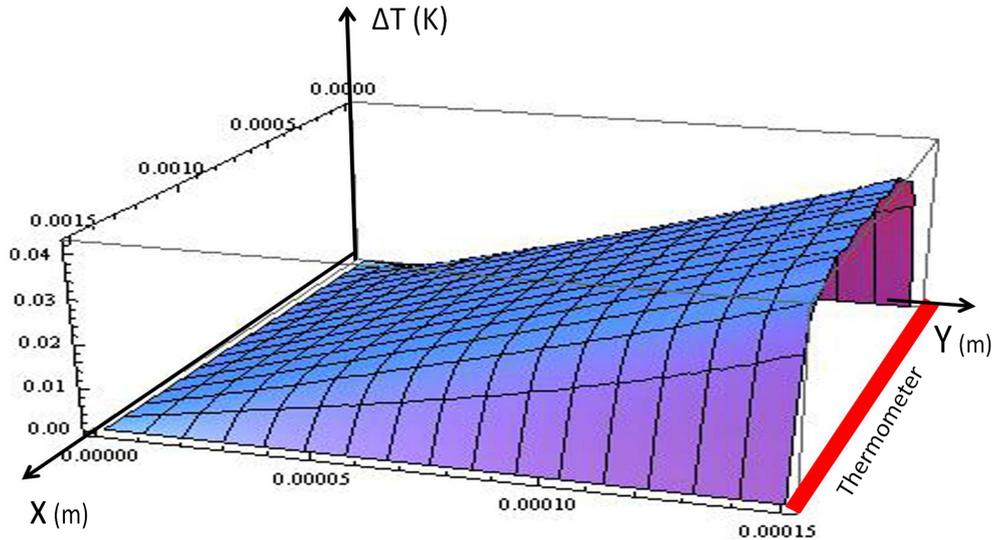
Figure 3.2: Schematic shows the steady state temperature profile on half of the membrane, at room temperature for a dissipated power of 1 μW and thermal conductivity $\kappa \sim 3$ W/m.K. The temperature elevation on the centre of the membrane is $\Delta T \sim 40$ mK.

3.1.1.2   General solution of transient equation

To derive the solution for the transient equation, the method of integral transforms [71] is used. This method consists to solve firstly the homogeneous equation, thus with:

$$\left.\frac{\partial V}{\partial y}\right|_{y=\ell} = 0$$

and then to calculate the dependence of time coefficient using:

$$\left.\frac{\partial V}{\partial y}\right|_{y=\ell} = -\frac{RI^2}{4\kappa s}cos(2\omega t).$$

Using the first assumption, all the boundary conditions are homogeneous, thus the transient equation can be solved by the method of separation of variables. We can assume that the solution is given by:

$$V(x,y,t) = X(x)Y(y)Z(t) \tag{3.17}$$

by substituting Eq. 3.17 into the transient part of Eq. 3.6 we obtain:

$$\frac{X''}{X} + \frac{Y''}{Y} = \frac{1}{D}\frac{Z'}{Z} = \pm(\lambda^2 + \beta^2) \tag{3.18}$$

where λ and β are two constants to be determined. Eq. 3.18 can be written as a system of two differential equations:

$$\begin{cases} X'' + \lambda^2 X = 0 \\ Y'' + \beta^2 Y = 0 \end{cases} \tag{3.19}$$

the solutions can be written as:

$$\begin{cases} X(x) = Acos(\lambda x) + Bsin(\lambda x) \\ Y(y) = Ccos(\beta y) + Dsin(\beta y) \end{cases} \tag{3.20}$$

where, A, B, C and D are constant coefficients which are determined using the boundary conditions given by Eq. 3.4. Thus we find:

$$\begin{cases} X(0) = Y(0) = 0 \\ X(L) = 0 \\ \left.\frac{\partial Y}{\partial y}\right|_{y=\ell} = 0 \end{cases} \tag{3.21}$$

$$\Rightarrow \begin{cases} A = C = 0 \\ B sin(\lambda L) = 0 \Rightarrow \lambda_n = \frac{n\pi}{L} \\ D\beta cos(\beta\ell) = 0 \Rightarrow \beta_m = (m + \frac{1}{2})\frac{\pi}{\ell} \end{cases} \tag{3.22}$$

then the solution of $V(x,y,t)$ becomes:

$$V(x,y,t) = \sum_{m=0}^{\infty}\sum_{n=1}^{\infty} Z_{mn}(t) sin(\frac{n\pi}{L}x) sin\left[(m + \frac{1}{2})\frac{\pi}{\ell}y\right] \tag{3.23}$$

the next step is to calculate $Z_{mn}(t)$ using the boundary and initial conditions:

$$\left.\frac{\partial V}{\partial y}\right|_{y=\ell} = -\frac{RI^2}{4\kappa s}cos(2\omega t)$$

$$V(x,y,0) = 0 \tag{3.24}$$

by multiplying the two sides of Eq. 3.23 by:

$\int_0^\ell \int_0^L sin(\frac{n'\pi}{L}x) sin\left[(m' + \frac{1}{2})\frac{\pi}{\ell}y\right] dxdy$

one obtains:

$$\int_0^\ell \int_0^L V(x,y,t) sin(\frac{n'\pi}{L}x) sin\left[(m' + \frac{1}{2})\frac{\pi}{\ell}y\right] dxdy =$$
$$\int_0^\ell \int_0^L \sum_{m=0}^{\infty}\sum_{n=1}^{\infty} Z_{mn}(t) sin(\frac{n\pi}{L}x) sin(\frac{n'\pi}{L}x) sin\left[(m + \frac{1}{2})\frac{\pi}{\ell}y\right] sin\left[(m' + \frac{1}{2})\frac{\pi}{\ell}y\right] dxdy \tag{3.25}$$

$$where \int_0^L sin(\frac{n\pi}{L}x) sin(\frac{n'\pi}{L}x)dx = \begin{cases} \frac{L}{2} & if \ n = n' \\ 0 & otherwise \end{cases}$$

$$and \int_0^\ell sin\left[(m + \frac{1}{2})\frac{\pi}{\ell}y\right] sin\left[(m' + \frac{1}{2})\frac{\pi}{\ell}y\right] dy = \begin{cases} \frac{\ell}{2} & if \ m = m' \\ 0 & otherwise \end{cases}$$

thus,

$$Z_{mn}(t) = \frac{4}{\ell L} \int_0^\ell \int_0^L V(x,y,t) sin(\lambda_n x) sin(\beta_m y) dx dy \tag{3.26}$$

$$\begin{aligned}
\frac{dZ_{mn}}{dt} &= \frac{4}{\ell L} \int_0^\ell \int_0^L \frac{\partial V}{\partial t} sin(\lambda_n x) sin(\beta_m y) dx dy \\
&= \frac{4D}{\ell L} \int_0^\ell \int_0^L \left[\frac{\partial^2 V}{\partial x^2} + \frac{\partial^2 V}{\partial y^2} \right] sin(\lambda_n x) sin(\beta_m y) dx dy \\
&= \frac{4D}{\ell L} \left[\int_0^\ell \int_0^L \frac{\partial^2 V}{\partial x^2} sin(\lambda_n x) sin(\beta_m y) dx dy + \int_0^\ell \int_0^L \frac{\partial^2 V}{\partial y^2} sin(\lambda_n x) sin(\beta_m y) dx dy \right] \\
&= \frac{4D}{\ell L} [I + J]
\end{aligned} \tag{3.27}$$

by the first integration by parts of I according to x one obtains:

$$\begin{aligned}
I &= \left\{ \left[\frac{\partial V}{\partial x} sin(\lambda_n x) \right]_0^L - \int_0^L \lambda_n \frac{\partial V}{\partial x} cos(\lambda_n x) dx \right\} \int_0^\ell sin(\beta_m y) dy \\
&= - \int_0^L \lambda_n \frac{\partial V}{\partial x} cos(\lambda_n x) dx \int_0^\ell sin(\beta_m y) dy
\end{aligned} \tag{3.28}$$

the second integration by parts according to x of I yields:

$$\begin{aligned}
I &= \left\{ -\lambda_n [V cos(\lambda_n x)]_0^L - \int_0^L \lambda_n^2 V sin(\lambda_n x) dx \right\} \int_0^\ell sin(\beta_m y) dy \\
&= -\lambda_n^2 \int_0^\ell \int_0^L V(x,y,t) sin(\lambda_n x) sin(\beta_m y) dx dy \\
&= -\lambda_n^2 \frac{\ell L}{4} Z_{mn}(t)
\end{aligned} \tag{3.29}$$

and by the first integration by parts of J according to y one obtains:

$$\begin{aligned}
J &= \left\{ \left[\frac{\partial V}{\partial y} sin(\beta_m y) \right]_0^\ell - \int_0^\ell \beta_m \frac{\partial V}{\partial y} cos(\beta_m y) dy \right\} \int_0^L sin(\lambda_n x) dx \\
&= \left\{ -\frac{RI^2}{4\kappa s} sin(\beta_m \ell) cos(2\omega t) - \int_0^\ell \beta_m \frac{\partial V}{\partial y} cos(\beta_m y) dy \right\} \int_0^L sin(\lambda_n x) dx
\end{aligned} \tag{3.30}$$

the second integration by parts according to *y* of *J* yields:

$$
\begin{aligned}
J &= \left\{ -\frac{RI^2}{4\kappa s}\sin(\beta_m\ell)\cos(2\omega t) - \beta_m\left[V\cos(\beta_m y)\right]_0^\ell - \beta_m^2\int_0^\ell V\sin(\beta_m y)dy \right\}\int_0^L \sin(\lambda_n x)dx \\
&= -\frac{RI^2}{4\kappa s}\sin(\beta_m\ell)\cos(2\omega t)\int_0^L \sin(\lambda_n x)dx - \beta_m^2\int_0^\ell\int_0^L V\sin(\lambda_n x)\sin(\beta_m y)dxdy \\
&= -\frac{RI^2}{4\kappa s}\sin\left[(m+\frac{1}{2})\pi\right]\left[-\frac{\cos(n\pi)-1}{\lambda_n}\right]\cos(2\omega t) - \beta_m^2\frac{\ell L}{4}Z_{mn}(t) \\
&= \frac{RI^2 L}{4\kappa sn\pi}(-1)^{m+1}\left[1-(-1)^n\right]\cos(2\omega t) - \beta_m^2\frac{\ell L}{4}Z_{mn}(t)
\end{aligned}
\tag{3.31}
$$

therefore, Eq. 3.27 becomes:

$$
\begin{aligned}
\frac{dZ_{mn}}{dt} &= \frac{4D}{\ell L}[I+J] \\
&= -D(\lambda_n^2 + \beta_m^2)Z_{mn}(t) + \frac{RI^2 D}{\pi\kappa ns\ell}(-1)^{m+1}\left[1-(-1)^n\right]\cos(2\omega t) \\
&= -\gamma_{mn}Z_{mn}(t) + \xi_{mn}\cos(2\omega t)
\end{aligned}
\tag{3.32}
$$

where,

$$
\gamma_{mn} = D\pi^2\left[\left(\frac{n}{L}\right)^2 + \left(\frac{m+\frac{1}{2}}{\ell}\right)^2\right]
$$

$$
\xi_{mn} = \frac{RI^2 D}{\pi\kappa ns\ell}(-1)^{m+1}\left[1-(-1)^n\right].
$$

Consequently, we obtain the differential equation which permits to calculate the coefficient $Z_{mn}(t)$:

$$
\frac{dZ_{mn}}{dt} + \gamma_{mn}Z_{mn}(t) - \xi_{mn}\cos(2\omega t) = 0
\tag{3.33}
$$

the general solution of Eq. 3.33 can be written as the sum of the general solution of the equation without the second term and a particular solution of the entire equation,

$$Z_{mn}(t) = \left[He^{-\gamma_{mn}t} \right]_{\text{general solution}}$$
$$+ \left[M\cos(2\omega t) + N\sin(2\omega t) \right]_{\text{particular solution}} \tag{3.34}$$

where, H, M and N are constants to be calculated. By substituting this solution into Eq. 3.33 one obtains:

$$-2\omega M\sin(2\omega t) + 2\omega N\cos(2\omega t) + \gamma_{mn}[M\cos(2\omega t) + N\sin(2\omega t)] = \xi_{mn}\cos(2\omega t) \tag{3.35}$$

$$\Rightarrow \begin{cases} 2\omega N + \gamma_{mn}M = \xi_{mn} \\ -2\omega M + \gamma_{mn}N = 0 \end{cases} \tag{3.36}$$

therefore,

$$M_{mn} = \frac{\gamma_{mn}\xi_{mn}}{4\omega^2 + \gamma_{mn}^2}$$
$$N_{mn} = \frac{2\omega\xi_{mn}}{4\omega^2 + \gamma_{mn}^2}$$

using the initial condition, $V(x,y,0) = X(x)Y(y)Z(0) = 0 \Rightarrow Z(0) = 0$

$$\Rightarrow H_{mn} = -M_{mn}.$$

The general solution of $Z_{mn}(t)$ becomes:

$$Z_{nm}(t) = -\frac{\gamma_{mn}\xi_{mn}}{4\omega^2 + \gamma_{mn}^2}e^{-\gamma_{mn}t} + \frac{\gamma_{mn}\xi_{mn}}{4\omega^2 + \gamma_{mn}^2}\cos(2\omega t) + \frac{2\omega\xi_{mn}}{4\omega^2 + \gamma_{mn}^2}\sin(2\omega t) \tag{3.37}$$

3.1.1.3   Periodic solution at 2ω

By plugging the terms oscillating at 2ω in Eq. 3.37 into Eq. 3.23, the expression of the temperature solution at 2ω becomes:

$$V(x,y,t)_{2\omega} = \sum_{m=0}^{\infty}\sum_{n=1}^{\infty}[M_{mn}\cos(2\omega t) + N_{mn}\sin(2\omega t)]\sin\left(\frac{n\pi}{L}x\right)\sin\left[(m+\frac{1}{2})\frac{\pi}{\ell}y\right] \tag{3.38}$$

then the average of the temperature oscillation at 2ω in the middle of membrane ($y = \ell$) is given by:

$$\triangle T_{2\omega} = \frac{1}{L} \int_0^L \sum_{m=0}^{\infty} \sum_{n=1}^{\infty} [M_{mn}cos(2\omega t) + N_{mn}sin(2\omega t)] \, sin\left(\frac{n\pi}{L}x\right) sin\left[(m+\frac{1}{2})\pi\right] dx \quad (3.39)$$

$$\triangle T_{2\omega} = \sum_{m=0}^{\infty} \sum_{n=1}^{\infty} [M_{mn}cos(2\omega t) + N_{mn}sin(2\omega t)] \, S_{mn} \quad (3.40)$$

where $S_{mn} = \frac{-(-1)^n+1}{n\pi}(-1)^m$.

The expression of $\triangle T_{2\omega}$ can be written as:

$$\triangle T_{2\omega} = \sum_{m=0}^{\infty} \sum_{n=1}^{\infty} \left[(M_{mn}S_{mn})^2 + (N_{mn}S_{mn})^2\right]^{1/2} sin(2\omega t + \varphi_{mn}) = |\triangle T_{2\omega}| \, sin(2\omega t + \varphi_{mn})$$

$$(3.41)$$

where,

$$\varphi_{mn} = \arctan\left[\frac{\sum_{m=0}^{\infty} \sum_{n=1}^{\infty} M_{mn}S_{mn}}{\sum_{m=0}^{\infty} \sum_{n=1}^{\infty} N_{mn}S_{mn}}\right]. \quad (3.42)$$

While $|\triangle T_{2\omega}|$ represents the amplitude of the temperature oscillation at 2ω frequency due to the sinusoidal nature of heating, the measurement of this quantity will provide the thermal properties of the membrane, namely thermal conductivity and heat capacity. $|\triangle T_{2\omega}|$ is determined indirectly by the measure of the 3ω voltage. Then the Eq. 2.22 is used to provide the relation between the two quantities.

At very low frequency, Eq. 3.40 becomes:

$$|\triangle T_{2\omega}| = \sum_{m=0}^{\infty} \sum_{n=1}^{\infty} \frac{S_{mn}RI^2(-1)^{m+1}[1-(-1)^n]}{\pi^3 n\kappa s\ell \left[\left(\frac{n}{L}\right)^2 + \left(\frac{m+1/2}{\ell}\right)^2\right]} \quad (3.43)$$

Note that from Eq. 3.40:

$$|\triangle T_{2\omega}| \longrightarrow 0 \text{ as } \omega \longrightarrow \infty, \quad \frac{d|\triangle T_{2\omega}|}{d\omega} \longrightarrow 0 \text{ as } \omega \longrightarrow 0$$

at low frequency, the temperature oscillation becomes independent of the frequency which lead to the appearance of a plateau at low frequency, while at high frequency, it becomes too small to be measured. Physically, the low frequency behavior is explained by the fact that the temperature of the membrane has sufficient time to equilibrate, and thus the sinusoidal effect of the heating current is lost. This regime is called quasi-static. On the other hand, at high frequency the thermal penetration depth $\lambda = \sqrt{\frac{2D}{\omega}}$ (with D the thermal diffusivity) becomes comparable to the membrane thickness, then the boundary condition at the other side of the thin film begins to play an important role in the heat transfer problem. As the length of the membrane is sufficiently long as compared to the width, and in order to simplify the heat transfer model, the 1-dimensional model is then developed using some assumptions. In the next sections we show this model and then a comparison between the two models.

3.2   One dimensional model

For simplification, as the membrane is thin ($e \sim 100$ nm), we assume that the part of the membrane just beyond the NbN transducer is heated like the thermometer. The membrane is represented in Fig. 3.3. As there is a symmetric axis coming through the middle of the transducer, the thermal system can be modeled using half the membrane and half the heating power. As the membrane is suspended in vacuum, we assume that the heat can only diffuse through the membrane toward the silicon substrate which is at constant temperature T_b. Thus, we consider a one dimensional model, where the heat flow is diffused from the center of the membrane toward the edges according to the x axis. The radiative heat loss is neglected as a thermal shield is put between the sample and the calorimeter wall. Therefore, the system can be modeled as a volume of matter with a total specific heat C' and bonded to the thermal bath by the membrane with a thermal conductivity κ. The thermal system is schematized in Fig. 3.3. The total specific heat C' takes into account both the NbN thermometer and the part of the membrane below the transducer. C' can be written as

$$C' = \rho_{\text{NbN}} c_{\text{NbN}} L e' \frac{b}{2} + c\rho \frac{b}{2} L e \tag{3.44}$$

with c the specific heat and ρ the density of the SiN membrane.

To determine the temperature gradient in the membrane, we solve the one dimensional thermal diffusion equation for the temperature profile in the membrane:

$$\frac{\partial^2 T(x,t)}{\partial x^2} = \frac{1}{D} \frac{\partial T(x,t)}{\partial t} \tag{3.45}$$

with D the thermal diffusivity of the membrane. In order to calculate the solution of Eq.
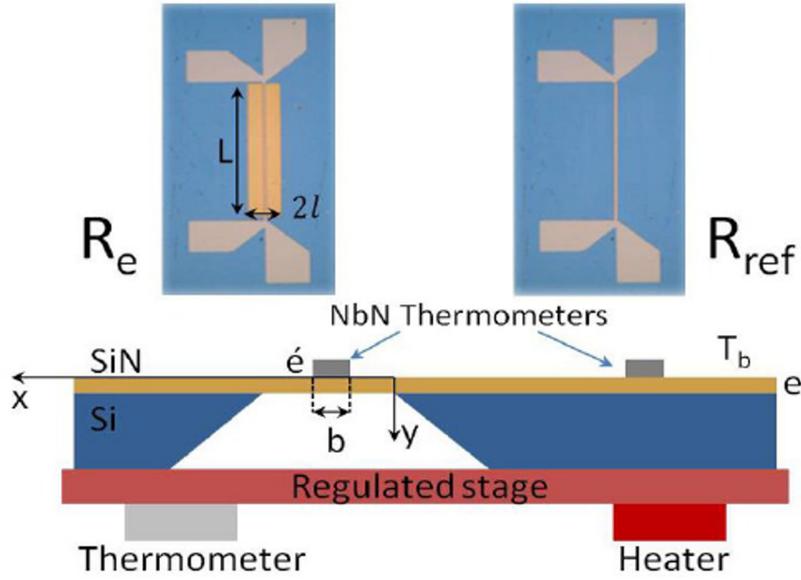
Figure 3.3: Photograph of the two NbN thermometers deposited on the membrane and on the bulk region; below, the schematic of the measurement device installed on the controlled temperature stage.

3.45, we need initial and boundary conditions. Therefore, we assume that at t=0, the temperature of the membrane is T_b since the transducer is not heated. Moreover, we assume that the membrane edge is always at $T=T_b$. The total dissipated power $P(t)$ is used to heat both the thermometer and the part of the membrane under the thermometer, and the rest of the membrane. Thus, the initial and boundary conditions can be written as:

$$\begin{cases} T(x, t=0) = T_b \\ C'(T) \left. \frac{\partial T(x,t)}{\partial t} \right|_{x=\ell} = P(t) - s\kappa \left. \frac{\partial T}{\partial x} \right|_{x=\ell} \\ T(x=0, t) = T_b \end{cases} \tag{3.46}$$

with $s = eL$ the cross section of the membrane. As shown in Fig. 2.5, the thermometer deposited on the membrane is located between A and C, the ac current passed through this thermometer can be expressed as:

$$I = I_0 sin(\omega t) = \left(\frac{V_{ac}}{R_e + R_1} \right) sin(\omega t) \tag{3.47}$$

thus, the expression of the total dissipated power in one half of the membrane is given by:

$$P(t) = \frac{1}{2}R_e I^2 = \frac{R_e}{4}\left(\frac{V_{ac}}{R_e + R_1}\right)^2(1 - cos(2\omega t)) \tag{3.48}$$

for simplification the ac power at 2ω can be written as:

$$P_{2\omega}(t) = \frac{R_e}{4}\left(\frac{V_{ac}}{R_e + R_1}\right)^2 e^{j2\omega t} = \frac{R_e}{2}\left(\frac{V_{ac}^{rms}}{R_e + R_1}\right)^2 e^{j2\omega t} = P_0 e^{j2\omega t} \tag{3.49}$$

using separation of variables, we look for solution at 2ω of Eq. 3.45 with the form:

$$T(x,t) = T(x)e^{j2\omega t} \tag{3.50}$$

where $T(x)$ is the spatial evolution of the temperature oscillations.

By substituting Eq. 3.50 into Eq. 3.45 we obtain:

$$\frac{d^2 T(x)}{dx^2} = \frac{j2\omega}{D}T(x) \tag{3.51}$$

this is a second order of ordinary differential equation, the general solution being:

$$T(x) = Ae^{\sigma x} + Be^{-\sigma x} \tag{3.52}$$

with $\sigma = \sqrt{\frac{j2\omega}{D}} = (1 + j)\sqrt{\frac{\omega}{D}} = (1 + j)\omega'$. A and B are two constant coefficients to be calculated using the boundary conditions. Therefore:

$$T(x,t) = (Ae^{\sigma x} + Be^{-\sigma x})e^{j2\omega t} \tag{3.53}$$

using the first boundary condition:

$T(0,t) = 0 \Rightarrow A = -B$

Eq. 3.53 becomes:

$$T(x,t) = 2Ash(\sigma x)e^{j2\omega t} \tag{3.54}$$

using the second boundary condition:

$$C'(T) \left. \frac{\partial T(x,t)}{\partial t} \right|_{x=\ell} = P(t) - s\kappa \left. \frac{\partial T}{\partial x} \right|_{x=\ell} \Rightarrow$$

$$C'(2Ash(\sigma\ell))j2\omega = P_0 - s\kappa(2A\sigma ch(\sigma\ell)) \tag{3.55}$$

$$A = \frac{P_0}{j4\omega C'sh(\sigma\ell) + 2s\kappa\sigma ch(\sigma\ell)} \tag{3.56}$$

thus the general solution of Eq. 3.45 is given by:

$$T(x,t) = \frac{P_0 sh\left[(1+j)\omega'x\right]e^{j2\omega t}}{j2\omega C'sh\left[(1+j)\omega'\ell\right] + s\kappa(1+j)\omega'ch\left[(1+j)\omega'\ell\right]} \tag{3.57}$$

$$T(x,t) = \frac{P_0}{D_0^{1/2}}\left[sin^2(\omega'x) + sh^2(\omega'x)\right]^{1/2}e^{j(2\omega t+\varphi)} \tag{3.58}$$

with $D_0^{1/2}$ the modulus of the denominator of Eq. 3.57 and φ the phase is given by:

$$\begin{cases} \varphi(\omega) = \varphi_1 + \varphi_2 \\ tg\varphi_1 = -\frac{\omega'\ell\left[ch(\omega'\ell)cos(\omega'\ell)+sh(\omega'\ell)sin(\omega'\ell)\right]+2\omega\tau sh(\omega'\ell)cos(\omega'\ell)}{\omega'\ell\left[ch(\omega'\ell)cos(\omega'\ell)-sh(\omega'\ell)sin(\omega'\ell)\right]-2\omega\tau ch(\omega'\ell)sin(\omega'\ell)} \\ tg\varphi_2 = \frac{tg(\omega'\ell)}{th(\omega'\ell)} \end{cases} \tag{3.59}$$

after development in Taylor expansion in first order in ω, the expression of the modulus of the temperature at the center of the membrane $T_{2\omega}(\ell)$ can be written as followed:

$$\mid T_{2\omega} \mid = \frac{P_0}{K_p\left[1 + \omega^2\left(4\tau^2 + \frac{2\ell^4}{3D^2} + \frac{4\tau\ell^2}{3D}\right)\right]^{1/2}} \tag{3.60}$$

with $K_p = \frac{\kappa s}{\ell}$, $\tau = \frac{C'}{K_p}$ and D the thermal diffusivity.

By substituting the expression of P_0 into Eq. 3.60 we obtain:

$$\mid T_{2\omega} \mid = \frac{R_e(V_{ac}^{rms})^2}{2(R_e+R_1)^2 K_p\left[1 + \omega^2\left(4\tau^2 + \frac{2\ell^4}{3D^2} + \frac{4\tau\ell^2}{3D}\right)\right]^{1/2}} \tag{3.61}$$

3.2.1   Thermal conductivity and specific heat measurement

At low frequency, the ω term in Eq. 3.61 becomes negligible, thus the expression of $|T_{2\omega}|$ can be written as:

$$|T_{2\omega}| = \frac{R_e(V_{ac}^{rms})^2}{2(R_e + R_1)^2 K_p} \tag{3.62}$$

by substituting the expression of $|T_{2\omega}|$ into Eq. 2.22 the expression $V_{3\omega}$ in its simplest form becomes:

$$|V_{3\omega}^{rms}| = \frac{\alpha R_e^2 R_1 (V_{ac}^{rms})^3}{4(R_e + R_1)^4 K_p} \tag{3.63}$$

as the 3ω voltage is measured at fixed temperature and balanced Wheatstone bridge, all the parameters of Eq. 3.63 are constant. Moreover, at low frequency $V_{3\omega}$ is independent of the frequency and depends on the thermal conductance K_P of the membrane. Thus, the measurement of $V_{3\omega}$ at low frequency can allow the calculation of the thermal conductance K_P using Eq. 3.63.

By using Eq. 3.61 and Eq. 2.22 the general expression of $V_{3\omega}$ becomes:

$$|V_{3\omega}^{rms}(\omega)| = \frac{\alpha R_e^2 R_1 (V_{ac}^{rms})^3}{4(R_e + R_1)^4 K_p \left[1 + \omega^2 \left(4\tau^2 + \frac{2\ell^4}{3D^2} + \frac{4\tau\ell^2}{3D}\right)\right]^{1/2}} \tag{3.64}$$

at fixed temperature, the specific heat of the membrane is extracted by fitting the 3ω voltage data versus frequency using Eq. 3.64.

Fig. 3.4 shows an example of experimental measurement of $V_{3\omega}$ versus frequency and its respective theoretical fit. This measurement is performed at $T = 250$ K for a SiN membrane of 100 nm thick. Using the thermal conductivity value determined from Eq. 3.63, fitting the experimental data with Eq. 3.64 yields the value of heat capacity of the SiN membrane.
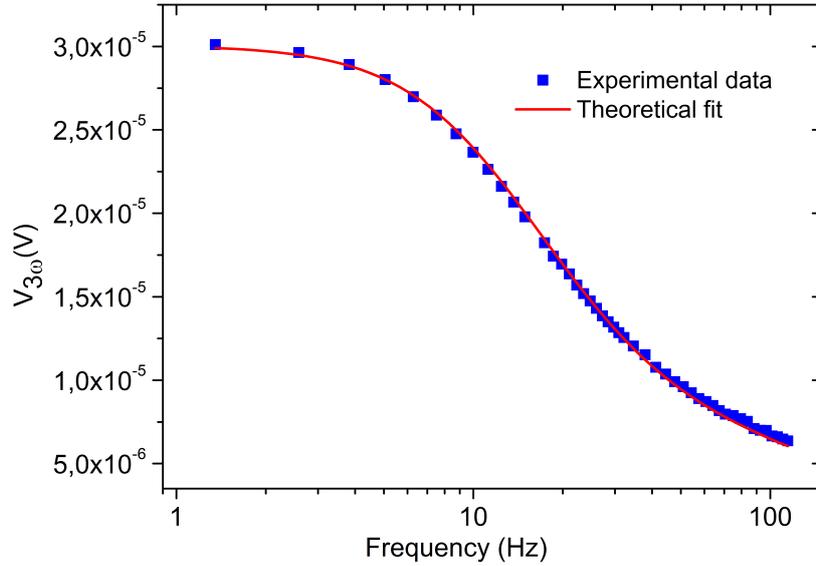
Figure 3.4: 3ω voltage measurement as function of frequency of the heater current. Experimental data agree well with the theoretical model. This measurement is performed at T = 250 K for a membrane 100 nm thick, the extracted values from the fit are $\kappa = 3.19$ W/m.K and $c = 0.68$ J/g.K.

3.3 Comparison between the one and two dimensional model

To summarize, the difference between the two models comes from the fact that the two-dimensional model takes into account the part of heat flow in the direction parallel to the thermometer, whereas just the perpendicular direction to the thermometer of heat flow is taken by the one-dimensional model. However, as the membrane is sufficiently thin, it is assumed that the thermometer and the region of the membrane just underside are at the same temperature. Finite element simulations have been performed to confirm this assumption using the ANSYS platform[1]. Results are displayed on Fig. 3.5. Heat flows from the thermometer to the quasi-infinite reservoir of the bulk silicon. Except at the edges of the membrane, the temperature along the heater is nearly the same. We can also verify on the Fig. 3.5 that the temperature is uniform over the membrane thickness confirming the assumption made for analytical calculations. Moreover, this is in good agreement with the order of magnitude of U_{ss} for the same dissipated power at room temperature as shown in Section. 3.1.1.1.

Fig. 3.6 shows the amplitude of the temperature oscillations at 2ω corresponds to the 1-dimensional and 2-dimensional models, presents in Eq. 3.61 and Eq. 3.41 respectively. A difference of 15% is shown at low frequency, however the two curves are very close at high frequency. Therefore, in the following the 2D model is used to extract thermal conductivity and the 1D model to extract specific heat.

---

[1]multiphysics engineering calculation platform.
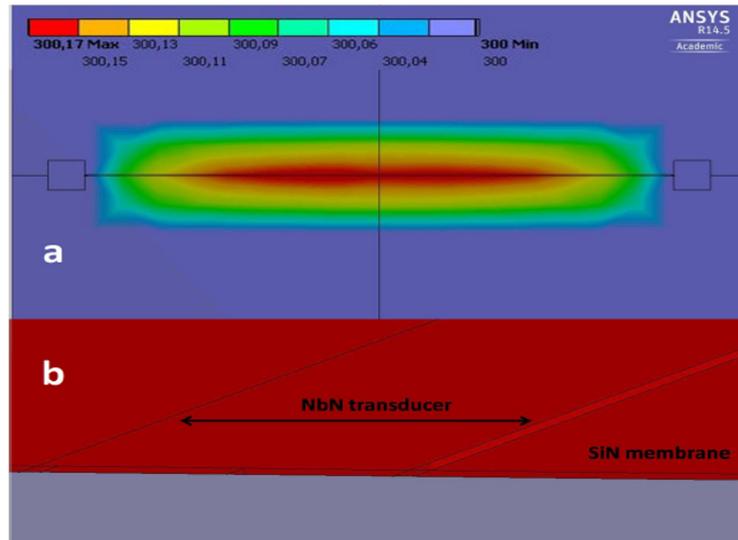
Figure 3.5: Finite element simulation of a 100 nm thick SiN membrane (width 300 μm and length 1.5 mm) including NbN thermometer with a dissipated power of 1 μW: (a) Top view of the membrane. The isotherm lines lie along the thermometer except at the edge of the membrane; (b) temperature profile of the cross-section of the membrane. The NbN thermometer (width 5 μm) and the membrane are at the same temperature; this temperature is constant over the entire thickness of the membrane.
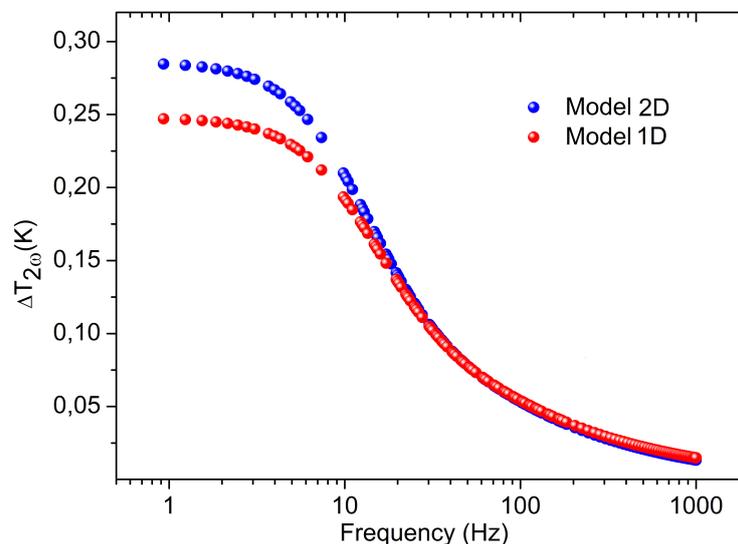
Figure 3.6: Amplitude of temperature oscillation at 2ω calculated using the 1-dimensional and 2-dimensional models. These curves are plotted using theoretical formulas of the two models and with the same fixed parameters.

3.4 Validation of the 3ω-Völklein method

The 3ω-Völklein method has been checked using two different measurements. According to Eq. 3.63, the $V_{3\omega}$ signal depends on the cube of the Wheatstone bridge voltage V_{ac}. Thus, the $V_{3\omega}$ signal has been measured at different temperatures to check this behaviour. As an example, the 250 K measurement is shown in Fig. 3.7. The linear fit gives a slope very close to 3 which confirms the cubic behaviour of the $V_{3\omega}$ signal versus the applied voltage V_{ac}. The second way of verification needs a frequency scan measurement. According to Eq. 3.64, the $V_{3\omega}$ signal depends strongly on the angular frequency ω. At low frequency, the square root term tends to 1 and consequently, the $V_{3\omega}$ signal becomes constant. An example of frequency scan of the 3ω voltage is presented at the Fig. 3.4. As predicted by the theory, a plateau is observed at low frequency for the $V_{3\omega}$ signal. The thermal conductivity κ can be extracted from the low frequency plateau using Eq. 3.63.
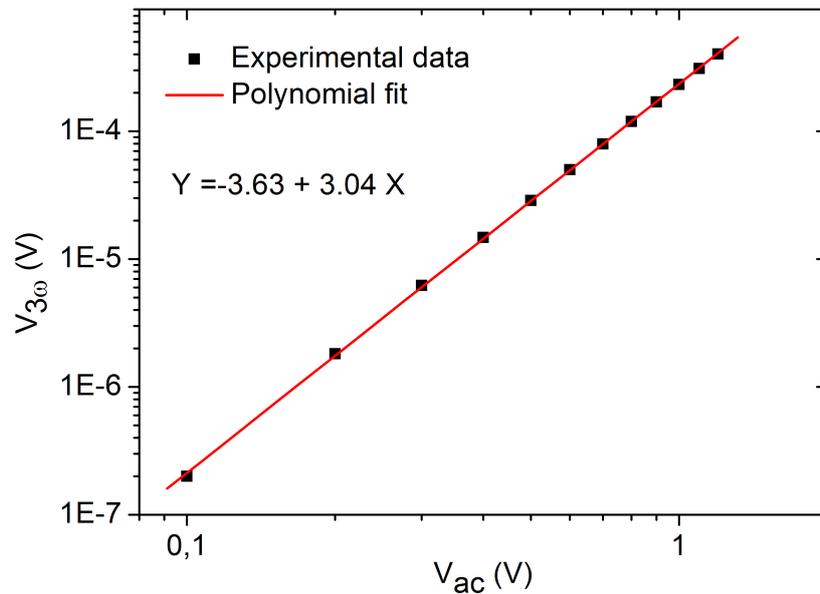
Figure 3.7: 3ω voltage measurement as a function of the voltage applied across the Wheatstone bridge V_{ac} in logarithmic scales (T = 270 K, R_e = 200 KΩ, α =0.0063 K^{-1}). The slope of the linear fit is very close to 3 confirms the cubic behavior of the $V_{3\omega}$ signal versus the applied voltage V_{ac}.

3.4.1   Effect of a finite transducer width

The effect of a finite thermometer width has been studied by the measurement of the 3ω voltage at fixed temperature using different thermometer width. Fig. 3.8 shows experimental measurements of the 3ω voltage as function of frequency of three distinct samples, these measurements are performed at $T = 250$ K for SiN membrane 100 nm thick. Fig. 3.8 exhibits a large difference in thermal frequency cut-off of the 3ω voltage.

Table 3.1: Thermal propertie parameters at 250 K obtained from the theoretical fit of the measured 3ω voltage using different thermometer widths b.

Sample#	b(μm)	k(W/(m.K))	C(J/(g.K))
1	5	3.190	0.698
2	20	2.980	0.710
3	30	3.230	0.786
4	40	3.470	1.155

The thermal properties obtained from the theoretical fit are mentioned in Table. 3.1. The length L of the thermometer is 1500 μm. The extracted thermal conductivity values present a small variation when the thermometer width increases. When the thermometer width is multiplied by a factor of eight, the extracted thermal conductance varies at most by 10 %, which is a weak effect. This effect can be explained by the fact that when the width of the thermometer becomes large as compared to the width of the membrane, a gradient of temperature appears between the center and the extremities of the thermometer, and thus it cannot be considered like a finite line oscillating at the same temperature to solve the heat transfer equation.

On the other hand, a significant effect of the thermometer width on the specific heat values is observed. An increase of 65 % is observed when the thermometer width is multiplied by a factor of eight. This observation is discussed in terms of the thermal penetration depth dependence with the frequency. At low frequency, the temperature oscillation at 2ω is the same for all the membrane, where the thermal penetration depth is larger than the dimension of the membrane. When the frequency increases, λ begins to decrease affecting the overall temperature oscillation of the membrane. At sufficient high frequency, λ becomes comparable to thermometer width and then the 3ω voltage becomes sensitive to the specific heat of the thermometer and the SiN membrane underneath (see Table. 3.1). At 100 Hz, the thermal penetration depth is estimated to be around 55 μm.

In the following, the measurements are performed with a thermometer having a width of 5 μm; the extracted specific heat values are in perfect agreement with the ones extracted from the experiment done with a thermometer having a width of 20 μm. As a conclusion for this part of the study, in order to do a safe experiment, a ratio of at least ten between the width of the membrane and the width of the thermometer has to be respected.
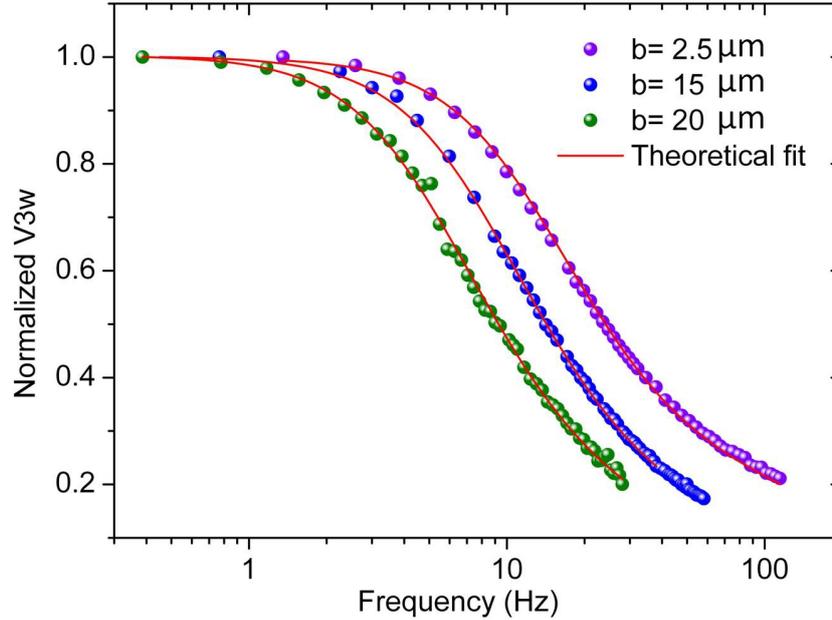
Figure 3.8: 3ω voltage measurements as function of frequency of three different samples. The measurements are performed at $T = 250$ K, of 100 nm SiN membrane. b denotes the half width of the thermometer, where the length is the same and close to 1500 μm.

3.4.2 Noise measurement, sensitivity

For high sensitivity experiment, low noise measurement chain is required. The noise has been evaluated by measuring the $V_{3\omega}$ signal during 500 s. The measurement at 300 K, obtained on a 50 nm thick membrane and a thermometer resistance $R_e \sim 75$ KΩ, is presented in Fig. 3.9. According to this measure, the noise is about 40 nV/$\sqrt{Hz}$ which is the expected Johnson noise. The noise/signal ratio (resolution) is about 6×10^{-3}. Thus, the smaller thermal conductance that can be measured is below 10^{-8} W/K, close to the nanoWatt per Kelvin. These measurements have been obtained with an oscillation of the temperature of the membrane of 150 - 200 mK, so it means that the setup can measure energies far below the nanoWatt. The accuracy of the method is estimated to be less than 1%.
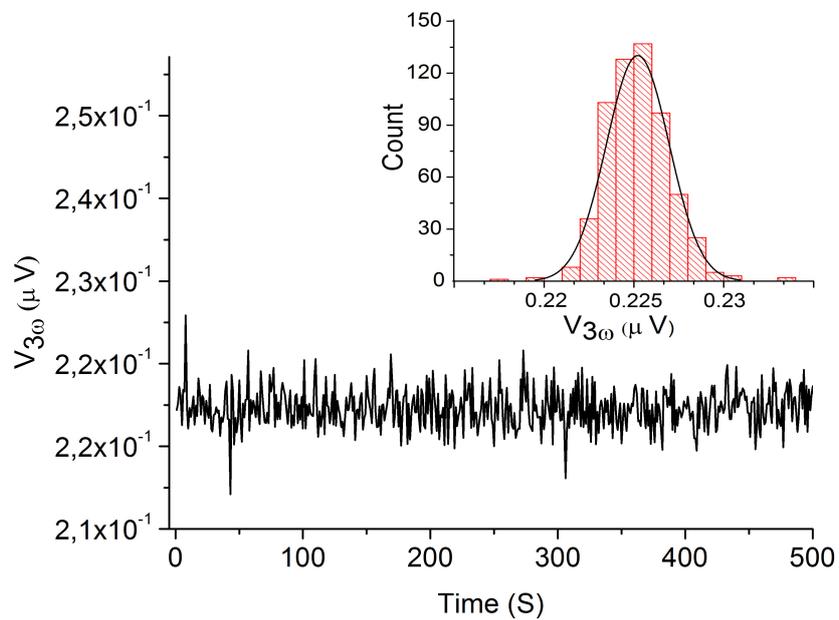
Figure 3.9: Measure of the 3ω voltage as a function of time on an 50 nm thick SiN membrane. The inset shows the signal distribution. The full width at half maximum corresponds to the noise of the measurement. In this case, the noise is evaluated to be around 40 nV/$\sqrt{\text{Hz}}$.

Chapter 4

Thermal properties of silicon nitride membrane

Thermal properties are essential to optimize the performance of many low temperature and/or nanostructure devices. Moreover, multi-domain coupling (electrical, mechanical and thermal) is an essential feature of micro and nanoscale devices [72]. These devices are commonly fabricated out of thin film materials. While electro-mechanical coupling is commonly exploited in microelectronic and other small-scale systems, the thermal domain must also be considered in these applications. Thermo-mechanical coupling in thin films is typically studied in terms of temperature effects on mechanical properties [73], and not from a thermal transport perspective. However, in this study we focus on the influence of mechanical stress on thermal properties of silicon nitride thin film.

According to the type of the material, there is different types of defects which can affect their thermal properties. In pure crystalline solids, the lattice vibrations are described as collective excitations or waves as explained by Debye. Thermal phonons can be scattered by different kind of lattice defects, like impurities, dislocations, vacancies. These defects lead to local changes in lattice vibrations, referred to as defect modes, which are specific to the type and concentration of the defects. Their influence on thermal conductivity and specific heat can be seen at low temperatures (T < 0.1 θ_D).

In amorphous solids such as the silicon nitride, a different kind of defect mode referred to as a "two-level system" exists. Thus, characteristic changes in their low temperature thermal conductivity and specific heat are shown to be universal. These changes include short and long-term thermal relaxation, and also in their time dependent elastic and dielectric functions. These properties have been first reported by Zeller and Pohl [34], and have been successfully described by a phenomenological model which takes into account the contribution from impurity modes [36, 37]. These tunneling states lead to a low temperature plateau in thermal conductivity and acoustic dissipation. In general, the spectral distribution of tunneling states and their coupling energy to the lattice depends on several material parameters, preparation conditions, and nature

of the defects themselves [42,74]. It was observed that stress can affect the universal behavior of mechanical dissipation in silicon nitride [74,75]. According to the tunneling model, the thermal conductivity can be given in term of mechanical dissipation and acoustic attenuation [42]. Thus the fundamental question, is if the stress can affect the tunneling states and then the thermal properties of the silicon nitride.

In this chapter, we present experimental results of thermal properties measurements for 50 nm and 100 nm suspended SiN membranes, in the two cases of low stress and high stress. In order to predict any possible effect of stress on thermal properties, the thermal conductivity and the specific heat will be fitted using the model developed by Wu and Yu [75]. Moreover the phonon diffusion in such system will be discussed in term of temperature, phonon mean free path and roughness. Finally, we present experimental results at low temperature (300 mK - 10 K) of 50 nm and 100 nm high stress silicon nitride membrane.

4.1   Origin of stress

Stress σ is defined by a force per unit area that is acting on a surface of a solid, more commonly expressed in Pascals Pa or N/m^2. Stress can be the result of external applied force. In this case, after the load is removed, the stress is expected to vanish. In the absence of any external mechanical stress, thin films can be still stressed; this stress is called as residual or internal [76]. The residual stress can be compressive or tensile. By convention, stress in first case is expressed with a minus sign and in second case, with a positive sign. The intrinsic stress reflects the internal structure of a material during its deposition. It depends on deposition rate, deposition temperature, pressure in the deposition chamber, incorporation of impurities during growth, grain structure, fabrication process defects, etc [77]. The intrinsic stress within the film can sometimes be annealed out completely. However the anneal temperatures are quite high and may not be practical for the production of micromechanical devices.

The average stress σ of a deposited film can be calculated using Stoney's formula [78]:

$$\sigma = -\frac{1}{6R}\frac{E}{(1-\nu)}\frac{D^2}{d} \qquad (4.1)$$

where (1/R) is wafer curvature shift. E, ν, D and d are the Young modulus, the Poisson ratio, the substrate thickness and the film thickness respectively.

4.2   Dissipation in glass

Dissipation in mechanical resonators has many physical origins. Generally, these can be classified as being of either intrinsic or extrinsic origin. Clamping losses (irreversible energy flow from resonator to resonator support) is an example of extrinsic losses. Loss mechanisms due to the intrinsic dissipation mechanisms include thermoelastic dissipation, dissipation at surfaces and interfaces [79], coupling between acoustic and thermal phonons, and most importantly for this study, stress influence on relaxation of defects (TLS) and consequently the thermal properties. Measuring thermal properties in modified intrinsic dissipation glass can be very useful to understanding the universal behaviors (thermal properties, dissipation) in glass.

Dissipation in oscillatory mechanical systems is frequently characterized by a dimensionless quality factor Q. The quality factor is defined as follows:

$$Q = 2\pi \frac{\text{total energy of system}}{\text{energy loss per cycle of oscillation}} \tag{4.2}$$

the quality factor measures the dampness of a mechanical system, or how long it takes a resonator to decay in amplitude. There are multiple ways of defining Q that are equivalent. Such as,

$$Q = \frac{\omega_0}{\Delta\omega} \tag{4.3}$$

where ω_0 is the resonant frequency of the oscillator, $\Delta\omega$ is the bandwidth of the peak response at half the peak value. When discussed as a physical quantity, the terms "dissipation" or "internal friction" specifically refers to the quantity Q^{-1}. The resultant overall dissipation for a resonator structure is a summation of contributions from individual factors as follows: $1/Q = 1/Q_{\text{intrinsic}} + 1/Q_{\text{extrinsic}}$. In this study, we shall concentrate on the effect of intrinsic dissipation on thermal properties.

Fig. 4.1 shows the internal friction as a function of temperature in many amorphous solids. Interestingly, the intrinsic friction Q^{-1} plateau falls within a factor of 20 for most of the amorphous materials including some amorphous metal, quasi crystals, polymers, and materials with significant proportion of defects [42]. Again this is the same factor as that found in thermal conductivity. The two dashed lines and the double arrow marking the range of the height of the plateau observed in several amorphous solids in which attenuation has been studied. Hence, the dissipation behavior is referred to as "universal" in glass. Moreover it was seen experimentally that the plateau in both thermal conductivity and acoustic dissipation starts at ~ 1 K.

The dropoff at the lowest temperature depends on the frequency of measurement. The dominant phonons which contribute to thermal conductivity at 1 K have frequencies in the THz range, whereas acoustic dissipation in glasses has been measured in low frequency resonators
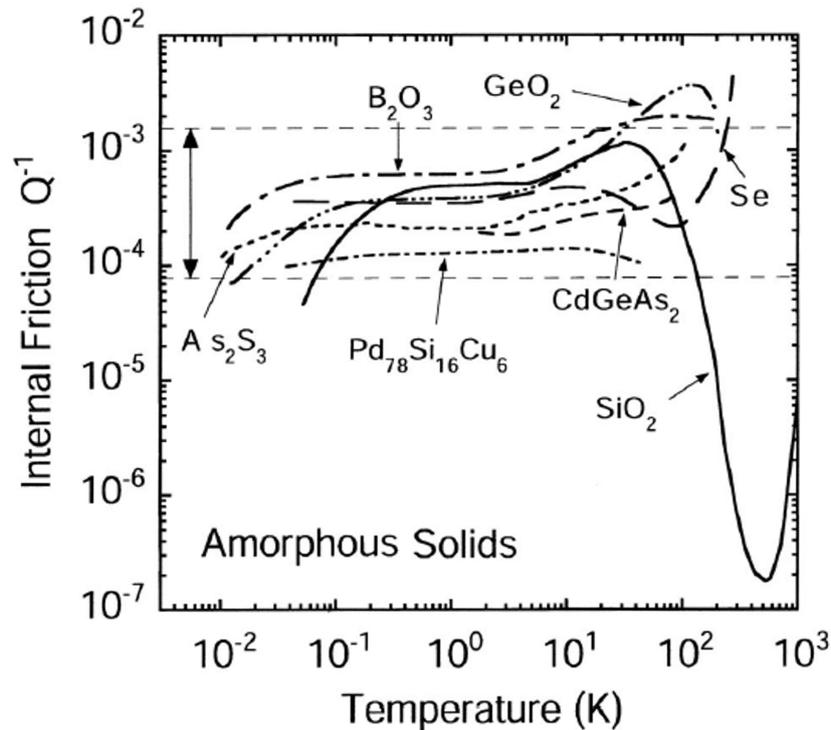
Figure 4.1: Internal friction in different glasses as a function of temperature. At low temperatures most of the amorphous and some crystalline materials with defects show a characteristic plateau which falls within the 10^{-3} and 10^{-4} [42].

down to few hundred Hz. Hence, disorder in the material influences the measured properties up to 10 orders magnitude of frequency. This dropoff are successfully described by the phenomenological tunneling model [36, 37] which takes into account the presence of two level system TLS. In this so-called tunneling model, it is postulated that some atoms or groups of atoms have two equilibrium positions between which they can tunnel. Above 10 K, the internal friction depends strongly on the chemical composition. Below that temperature, it approaches a temperature independent value. Moreover the magnitude of the internal friction plateau is very little affected by the frequency of the measurement.

As the dissipation in glass seems to be universal, the effect of stress on thermal properties of silicon nitride can be treated in term of mechanical dissipation. A phenomenological model was developed by Clare and Freeman [80] to fit both the thermal conductivity and the specific heat of glasses. This model is based on the total expression of mean free path by introducing terms corresponding to TLS, Einstein oscillators. As given above, glasses have a universal behavior concerning mechanical dissipation. Moreover, internal friction is in sharp relation with the mean free path within glass, as given by Pohl [42]: $Q^{-1} = \lambda/2\pi l$ where l is the mean free path and λ is the phonon wavelength. Further, in order to determine the influence of stress on thermal properties, a model is given by Wu and Yu, where the stress is treated as source of acoustic attenuation. In the following section we explain this model, and then we use it to interpret our experimental results.

4.3 Theoretical model for glass thermal properties

Since the new experimental evidences of glass was highlighted by Zeller and Pohl (1971) [34] until today, the study of glass thermal properties attracts considerable theoretical efforts. This leads to understand the properties of glasses, especially at low temperature where they present different behaviors as compared to that of crystals and seems to be universal. The most successful model is known as "tunneling state" or "two level systems" model TLS, and it was proposed independently by Anderson [37] and Phillips [36]. This model remains today by far the most used for the interpretation of the measurements on glasses. However subsequent experiments showed the necessity of more refinement.

4.3.1 Two-level systems and low-temperature heat capacity

The two level system model[1] takes the assumption that, in a glassy system, a certain number of atoms (or groups of atoms) can sit on one of two local equilibrium positions. Such as shown in Fig. 4.2, the atoms can tunnel between these positions and then move within a double well potential. The abscissa describes the position of the "particle" with the mass m or, more generally, reflects its configurational coordinate d.

In general, such a potential will be asymmetric, characterized by a barrier height V, and an asymmetry energy Δ. The energy difference E between the two lowest states E_0 and E_1 of the double well (its excitation energy) is given by:

$$E^2 = \Delta^2 + \Delta_0^2 \qquad (4.4)$$

where Δ_0, is the barrier strength which is related to the parameters of the well by:

$$\Delta_0 = \hbar\omega_0\exp(-\lambda), \text{ with } \lambda = d\left(\frac{2mV}{\hbar^2}\right)^{(1/2)} \qquad (4.5)$$

Here ω_0 is the frequency of oscillation in an individual well. The factor $\exp(-\lambda)$ represents the overlap between the wave functions for the two potential wells. Δ and λ are distributed randomly over an interval, their distribution being described by:

$$P(\Delta,\lambda)d\Delta d\lambda = \bar{P}d\Delta d\lambda, \text{ for } |\Delta| \leq \Delta_{\max}, \text{ and } \lambda_{\min} \leq \lambda \leq \lambda_{\max} \qquad (4.6)$$

---

[1]Note that the "two level system" describes a particular case of tunneling state.

with this distribution, the density of states for the TLS exhibits a logarithmic dependence on energy, and it can be often considered as uniform:

$$n(E) = \bar{P}\ln\left(\frac{2E}{\Delta_{0min}}\right), \text{ with } \Delta_{0min} = \hbar\omega_0\exp(-\lambda_{max}).$$

(4.7)

If the only present vibrational modes in a solid are TLSs, it can be shown that the specific heat is given by the following integration over them:

$$c_v = \int_0^\infty n(E)\left(\frac{E^2}{k_BT^2}\right)\text{sech}^2\left(\frac{E}{k_BT}\right)dE$$

(4.8)

For the range of energies of interest ($10^{-5} < E < 10^{-4}$ eV), $n(E)$ can be taken to be a constant n_0. Therefore Eq. 4.8 becomes [36]:

$$c_v = \frac{\pi^2}{12}k_B^2 n_0 T$$

(4.9)

which accounts naturally for the linear variation of the specific heat of glasses at very low temperatures ($T < 1$ K), (note that this expression of the specific heat is two times lower than that given by Anderson [37]: $\pi^2 k_B^2 n_0 T/6$). Therefore according to this model, the atoms of interest for the specific heat will be those for which the energy barrier is sufficiently large so that "resonant tunnelling" between the two local minima does not occur, but sufficiently small so that "tunnelling" between the two levels can take place and thermal equilibration can occur during the time span of the specific heat experiment.

4.3.2   Thermal conductivity and sound transport

To obtain the thermal conductivity and the acoustic absorption in glass, interaction of TLSs with phonons must be taken into account. This interaction results in a scattering of propagating phonons by the localized TLSs and limits the mean free path l. Hence phonons with energy $\hbar\omega$ can be scattered by a process of excitation from the ground state (absorption of a phonon) followed by an emission of an incoherent phonon. Such a process is called "resonant scattering" [36, 37] and the resulting mean free path is given by:

$$l_{res}^{-1}(T,\omega) = \alpha\omega \ \tanh\left[\frac{\hbar\omega}{2k_BT}\right]$$

(4.10)

where
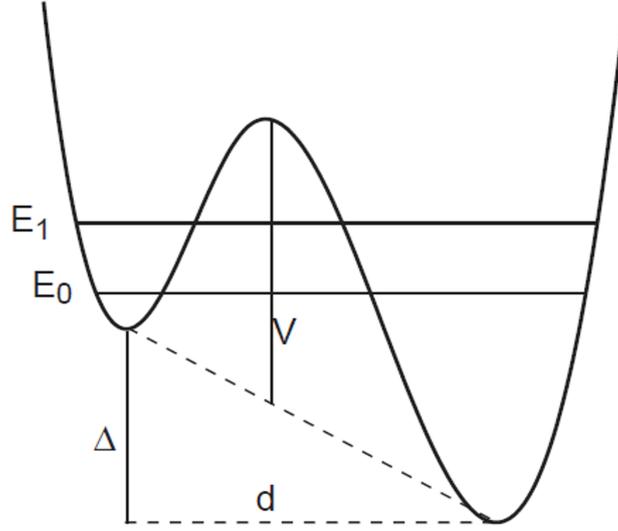
Figure 4.2: Schematic illustration of the double-well potential characterizing a two-level system plotted as a function of a suitable generalized coordinate.

$$\alpha = \frac{\pi \bar{P} \gamma^2}{\rho \upsilon^3} \tag{4.11}$$

and $\bar{P}$ is the density of TLS states associated with thermal conductivity. In general $n_0/\bar{P} \sim 10$ [80]. The average coupling between TLS and the strain field is γ, ρ is the mass density and υ is the velocity of sound.

Since $\hbar \omega = k_B T$ for thermal phonons, the mean free path is proportional to T^{-1} at low temperatures: $l_{\text{res}} \propto T^{-1}$. At low temperature the specific heat includes large contributions from local excitations that do not carry heat, thus it is approximated by the Debye specific heat $C_D \propto T^3$. Substituting this relation into the equation for thermal conductivity given by kinetic theory, we get the temperature dependence $\kappa \sim T^2$ in accordance with the experimental results below 1 K both in respect of temperature dependence and magnitude. Thus κ can be approximated by [81]:

$$\kappa(T) = \frac{\rho k_B^3 T^2}{6 \pi \hbar^2 \bar{P}} \sum_i \frac{\upsilon_i}{\gamma_i} \tag{4.12}$$

with i indicating their polarization, transverse (t) and longitudinal (l).

Therefore the resonant scattering mechanism is able to explain the initial growth of κ as a function of temperature, but not the subsequent plateau. For this, another non-resonant scattering is defined. Initially it was considered by Jäckle [82], is due to TLS relaxation. This arises

because phonons perturb the energy-level separation, and as a result the level population must readjust to a new equilibrium, which is given by [83]:

$$l_{\text{rel,TLS}}^{-1}(T,\omega) = \frac{\gamma^2\omega}{\rho\upsilon^3} \int_0^\infty \int_0^\infty P(E,\tau) \left[\frac{\Delta}{E}\right]^2 \frac{1}{k_B T} \text{sech}^2 \left[\frac{E}{2k_B T}\right] \frac{\omega\tau}{1+\omega^2\tau^2} dE d\tau \qquad (4.13)$$

at low temperature ($T < 100K$), using the assumption $\frac{\Delta^2 \omega\tau}{E^2 k_B T} = 1$, this expression is approximated by [80]:

$$l_{\text{rel,TLS}}^{-1}(T,\omega) = \frac{\alpha}{\pi}\omega \int_0^\infty \frac{e^x dx}{(e^x+1)^2} \left[\frac{\pi}{2} - \tan^{-1}(\omega\tau_m(x))\right] \qquad (4.14)$$

where $x = E/k_B T$,

$$\begin{aligned} \tau_m^{-1}(x) &= \left[\frac{1}{\upsilon_l^5} + \frac{2}{\upsilon_t^5}\right] \frac{\gamma^2 k_B^3 T^3}{2\pi\rho\hbar^4} x^3 \coth\left[\frac{x}{2}\right] \\ &= Ax^3 \coth\left[\frac{x}{2}\right] \end{aligned} \qquad (4.15)$$

where τ_m is the minimum relaxation time for a TLS with energy E at temperature T.

For $\omega\tau_m \ll 1$, $l_{\text{rel,TLS}}^{-1} = \frac{\alpha}{4}\omega$

For $\omega\tau_m \gg 1$, $l_{\text{rel,TLS}}^{-1} = \frac{\pi^3}{16}\alpha A T^3$.

Therefore, the relaxation of the levels takes place at a rate τ, moreover this process yields a relaxational mean free path $l_{\text{rel,TLS}} \propto T^{-3}$. Therefore, the net mean free path is given by $l_{\text{TLS}}^{-1} = l_{\text{res}}^{-1} + l_{\text{rel}}^{-1}$. It explains qualitatively, that when included in the thermal conductivity expression given by the kinetic theory, a plateau in thermal conductivity appears. For quantitative agreement, more sophisticated models are required, including non uniform distributions of the parameters Δ, V, and τ.

A phenomenological model was given by Yu and Freeman [80] able to fits both the specific heat and thermal conductivity data from low temperature to about 100 K. In order to explain the plateau, it is viewed as a crossover from a low-frequency region ($\nu \lesssim 10^{11}$ Hz) with a long mean free path ($l \sim 150\lambda$) to a high frequency region ($\nu \gtrsim 10^{12}$ Hz) with a short mean free path ($l \sim \lambda$), where λ is the phonon wavelength. Moreover, in the crossover region $l \propto \lambda^4$ as for Rayleigh scattering [84]. According to this model, the decrease in mean free path at high

frequency is explained by a sharp increase at energy E_0 in the density of states $n(E)$ of local excitations which scatter phonons. Therefore, this enhancement accounts for both the rise in κ above the plateau and the anomalous specific heat.

These local modes are described by Einstein oscillators (EO) of energy E, and a density of state $n(E)$ given by:

$$n(E) = n_0[1 + S\Theta(E - E_0)] = \begin{cases} n_0 & \text{if } E < E_0 \\ n_0(1 + S) & \text{if } E > E_0 \end{cases} \tag{4.16}$$

where S is the step height, n_0 is the constant TLS density of states which contribute to the specific heat. Therefore the specific heat has contribution from TLS, local modes and Debye phonons. Einstein oscillators give linear rise to the specific heat in temperature, so like the TLS but with a different coefficient. Thus the maximum in C/T^3 may be viewed as a crossover from one to the other.

The Rayleigh scattering was included below the step in the form:

$$l_{\text{Rayleigh}}^{-1} = B\omega^4 \tag{4.17}$$

where B is a constant. Rayleigh scattering is only valid in the region $ka \lesssim 1$ where k is the phonon wave vector and a is the "size" of a scatter. For convenience, the cut off of the Rayleigh scattering is taken at E_0.

Consequently, the total mean free path is given by the following expression:

$$l^{-1}(T, \omega) = \begin{cases} l_{\text{res,TLS}}^{-1}(T, \omega) + l_{\text{rel,TLS}}^{-1}(T, \omega) + l_{\text{Rayleigh}}^{-1}(T, \omega) & \text{for } \hbar\omega < E_0, \\ l_{\text{res,TLS}}^{-1}(T, \omega) + l_{\text{rel,TLS}}^{-1}(T, \omega) + l_{\text{res,EO}}^{-1}(T, \omega) & \text{for } \hbar\omega > E_0. \end{cases} \tag{4.18}$$

4.4 Impact of stress on silicon nitride thermal properties

As stress can affect the mechanical properties of the SiN, its impact on thermal properties should be treated in terms of Q factor. Dissipation in amorphous solids seems to be universal, as we showed in the section 4.2. In addition, Q factor is in sharp relation with the phonon mean free path as given by Pohl [42]:

$$Q^{-1} = \frac{\upsilon}{2\pi v}\alpha = \frac{\upsilon}{\omega}\frac{1}{l} = \frac{1}{2\pi}\frac{\lambda}{l} = \frac{1}{kl} \tag{4.19}$$

where α is the the ultrasonic (energy) attenuation. Moreover, Pohl found that the ratio of the phonon wavelength λ to the phonon mean free path l, lie between 10^{-3} and 10^{-2} in almost all cases independent of chemical composition and frequency (wavelength) of the elastic waves, which varied by more than nine orders of magnitude in the different experiments.

However, there are exceptions such as in amorphous silicon where doping with 1% of hydrogen reduces the low temperature internal friction plateau by about a factor of 200 [85].

In addition, it was observed recently that the silicon nitride exhibits a remarkable Q factor. As shown in Fig. 4.3, high stress silicon nitride exhibits a dissipation Q^{-1} with two to three orders of magnitude lower than that of amorphous SiO_2 from 4 K up to room temperature. Moreover, dissipation in stress relieved has a Q^{-1} that is about an order of magnitude lower than typical amorphous solids [74].
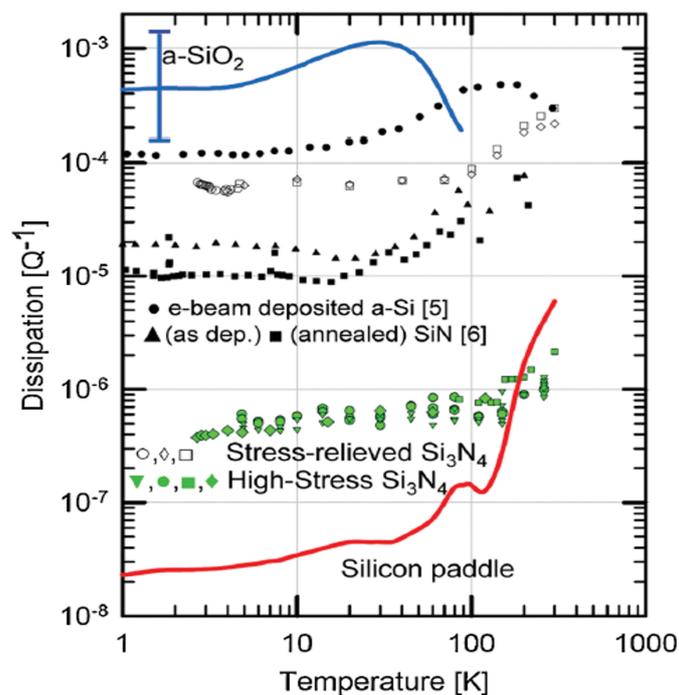
Figure 4.3: Temperature dependent internal friction measured for same high-stress LPCVD Si_3N_4 membrane structures. This is contrasted with the behavior of a-SiO_2 (solid blue line) and single crystal Si (solid red line) [74, 85].

The studied silicon nitride films shows no long-range order in x-ray diffraction and e-beam consistent with a disordered state, thus it is shown that stress alters the dissipation Q^{-1}.

This remarkable large effect of stress was seen experimentally. However, up to now there is not so many theoretical explanation for these results. In this sense, a theoretical model was provided recently by Wu and Yu [75], proposes that stress (whether internal or external) can reduce the dissipation in glasses. However, this cannot be explained by one physical effect, where impurities, dopants, and internal bond constraints can produce internal stress. According

to this model, the stress effect may be justified either by increasing TLS barrier heights or by decreasing the coupling between phonons and TLS.

In this study, we shall concentrate on thermal properties of silicon nitride and ignore measurements of mechanical dissipation. Since low dissipation implies a long phonon mean free path and a high thermal conductivity, this model predicts that the thermal conductivity of high stress Si_3N_4 (if there is no dissipation dilution) could be higher than stress relieved Si_3N_4, which is an order of magnitude higher than amorphous SiO_2 from 4 K up to room temperature.

Just as the model of Yu and Freeman explained above, this model cut off Rayleigh scattering at E_0. The thermal activation is included as well as direct phonon relaxation in the TLS relaxation processes, and the relaxation attenuation from Einstein oscillators is assumed to be negligible [83].

The internal friction is related to the Q factor by:

$$Q^{-1} = A\phi \tag{4.20}$$

where ϕ is the internal friction, and A is due to the dissipation dilution and is a function of macroscopic parameters, e.g., elastic moduli [86]. The dissipation dilution is the phenomenon with which a mechanical oscillator made from elastic elements with a given loss angle can have a quality factor rather greater than the expected value.

In this model, it is assumed that $A = 1$ in Eq. 4.20, thus Q^{-1} is used in place of the internal friction ϕ. Therefore, the total mean free path given by Eq. 4.18 can be written in term of Q^{-1} as:

$$Q^{-1} = \begin{cases} Q^{-1}_{\text{res,TLS}} + Q^{-1}_{\text{rel,TLS}} + Q^{-1}_{\text{Rayleigh}} & \text{for } E < E_0, \\ Q^{-1}_{\text{res,TLS}} + Q^{-1}_{\text{rel,TLS}} + Q^{-1}_{\text{res,EO}} & \text{for } E > E_0. \end{cases} \tag{4.21}$$

The attenuation due to TLS relaxation is given by:

$$Q^{-1}_{\text{rel,TLS}}(T, \omega) = \frac{2Q_0^{-1}}{\pi k_B T} \int_{V,\Delta} \left[\frac{\Delta}{E}\right]^2 \text{sech}^2\left[\frac{E}{2k_B T}\right] \frac{\omega\tau}{1 + (\omega\tau)^2}. \tag{4.22}$$

At low temperature ($0.1 < T < 10$ K) and low frequency ($\nu < 1$ THz), Q^{-1} is given by Q_0^{-1} which is a temperature-independent constant [83]:

$$Q_0^{-1} = \frac{\pi \bar{P}\gamma^2}{2\rho\upsilon^2} \tag{4.23}$$

and $\int_{V,\Delta} \equiv \int_0^{V_{max}} dV \int_0^{2V} d\Delta P(\Delta,V)/\bar{P}$ with $V_{\max} = V_0 + 6\sigma_0$.

$P(\Delta,V)$ is the TLS distribution of Δ and V. Δ is the energy asymmetry between the potential energy wells, V is the height of the energy barrier. It assumed that Δ has a uniform distribution and V a Gaussian distribution with an average V_0 and a variance σ_0 [82]:

$$P(\Delta,V) = \frac{2\bar{P}}{\hbar\Omega_0} exp\left[-\frac{(V-V_0)^2}{2\sigma_0^2}\right]. \tag{4.24}$$

τ^{-1} is the TLS relaxation rate given by the sum of the direct phonon relaxation rate τ_d in which the excited TLS decays to the ground state by emitting a phonon, and the rate τ_{Arr}^{-1} of Arrhenius activation over the barrier:

$$\tau^{-1} = \tau_d^{-1} + \tau_{\text{Arr}}^{-1} \tag{4.25}$$

$$\tau_d^{-1} = \sum_{a=\ell,t} \left(\frac{\gamma_a^2}{\upsilon_a^5}\right) \frac{E\Delta_0^2}{2\pi\rho\hbar^4} \coth\left(\frac{E}{2k_BT}\right) \tag{4.26}$$

$$\tau_{\text{Arr}}^{-1} = \tau_0^{-1}\cosh\left(\frac{\Delta}{2k_BT}\right) e^{-\frac{V}{k_BT}} \tag{4.27}$$

where the sum is over the longitudinal and transverse phonon modes and $\tau = 2/\Omega_0$.

The tunneling matrix element Δ_0 is given by [83]:

$$\Delta_0 = \frac{\hbar\Omega_0}{\pi}(\sqrt{\Lambda+1} + \sqrt{\Lambda})\exp(-\sqrt{\Lambda^2 + \Lambda}), \tag{4.28}$$

where $\Lambda = 2V/\hbar\Omega_0$, and $\hbar\Omega_0$ is the energy spacing level between the harmonic oscillator wells.

At low temperature and low frequency, TLS relaxation dominates Q^{-1} where the plateau in Q^{-1} is given by:

$$Q_{\text{plat}}^{-1} = Q_0^{-1}\exp\left[-\frac{V_0^2}{2\sigma_0^2}\right] \tag{4.29}$$

and therefore this replaces Eq. 4.23 which presents the limit of $Q_{\text{rel,TLS}}^{-1}$ for $\omega\tau_m \ll 1$ [80].

The Rayleigh, Einstein oscillator, and resonant phonon scattering Q^{-1} terms are given by:

$$
\begin{aligned}
Q_{\text{ray}}^{-1} &= B\upsilon\omega^3 \\
Q_{\text{EO}}^{-1} &= Q_0^{-1}\frac{2S_k}{\pi} \\
Q_{\text{res,TLS}}^{-1} &\simeq Q_0^{-1}\tanh\left(\frac{\hbar\omega}{2k_{\text{B}}T}\right)
\end{aligned}
\tag{4.30}
$$

where S_k is the step height in the density of states of the Einstein oscillators that is used to fit the thermal conductivity and B is a constant.

To summarize, according to this model, there is two possible ways in which stress can reduce dissipation:

- either by increasing the barrier height of microscopic fluctuating V (by increasing the average height V_0 and decreasing the variance σ_0 in $P(\Delta, V)$,

- or by decreasing the coupling (deformation potential) γ between phonons and TLS.

In the following sections, we will present the theoretical predictions of thermal conductivity and specific heat using the two assumptions explained above. Then we will discuss our experimental results in term of this model.

4.4.1 Specific heat

The specific heat $C(T)$ in glass has contributions from the phonons which is approximated with the Debye specific heat C_D, from TLS C_{TLS}, and from local modes which is modeled with Einstein oscillators C_{EO} [80]:

$$
C(T) = C_D(T) + C_{\text{TLS}}(T) + C_{\text{EO}}(T), \tag{4.31}
$$

where

$$C_D = 9\frac{N}{V}k_B\left(\frac{T}{\Theta_D}\right)^3\int_0^{x_D} dx 4x^4 \frac{e^x}{(e^x-1)^2},\tag{4.32}$$

$$C_{\text{TLS}} = k_B\bar{P}\int_{V,\Delta} x^2 \frac{e^x}{(e^x+1)^2} = \frac{\pi^2}{6}n_0 k_B^2 T,\tag{4.33}$$

$$C_{\text{EO}} = n_0 S_c k_B^2 T\int_{x_0}^{x_D} dx \frac{x^2 e^x}{(e^x-1)^2},\tag{4.34}$$

where $x = E/k_B T$, $x_0 = \hbar\Omega_0/k_B T$, $x_D = \Theta_D/T$. With N/V is the number density of formula units and Θ_D is the Debye temperature. n_0 is the TLS density of states that contribute to the specific heat, and S_c is the size of the step in the density of states due to the Einstein oscillations that contribute to $C(T)$.

In order to study a possible effect of stress on the specific heat, we have used Eq. 4.31 to fit our experimental data on specific heat for both low stress and high stress SiN membrane (50 nm and 100 nm). As we don't know the stoichiometry of the SiN low stress, N/V is determined by comparing the 50 nm specific heat data to a fitted data of the same thickness of $SiN_{1.15}$ low stress [87]. As shown in Fig. 4.4, there is a slight difference between the two data. According to theoretical fit, it was found that the ratio of n_0 to N/V for $SiN_{1.15}$ is given by [75]:

$$\frac{n_0\times 10K}{(N/V)10^{-3}} = 5.6\tag{4.35}$$

Therefore, as n_0 presents the TLS density of states that contribute to the specific heat, and as the two experimental data are very similar, we assume that the SiN low stress has the same ratio of n_0 to N/V. Using Eq. 4.35 one can make N/V as function of n_0 into Eq. 4.32. Finally the data is fitted by Eq. 4.31 to determine n_0, $\bar{P}$, Θ_D, and S_c.

Once n_0 is known from the fit, N/V can be calculated through Eq. 4.35. This value can be then used to fit the specific heat of 100 nm SiN low stress. The high stress SiN is a stoichiometric LPCVD silicon nitride, thus N/V is well known.

Fig. 4.5 shows experimental data of 50 nm SiN low stress along with theoretical fit using Eq. 4.31. The other data are fitted using the same model with the parameters given in Table. 4.1. A comparison between the different measurements is shown in Fig. 4.6. The curves of high stress (50 nm and 100 nm) and low stress (100 nm) are very close to each other. This is consistent with the prediction of the barrier height model V and the γ model, where the high stress and stress relieved Si_3N_4 lie on top each other [75].

From Table. 4.1 we see that the TLS density of state n_0 of both 50 nm low stress and high stress: $n_0 = 644\times 10^{45}/$J m^3 and $n_0 = 770\times 10^{45}/$J m^3 are respectively much higher than n_0 of their 100 nm counterpart low stress and high stress: $n_0 = 172\times 10^{45}/$J m^3 and
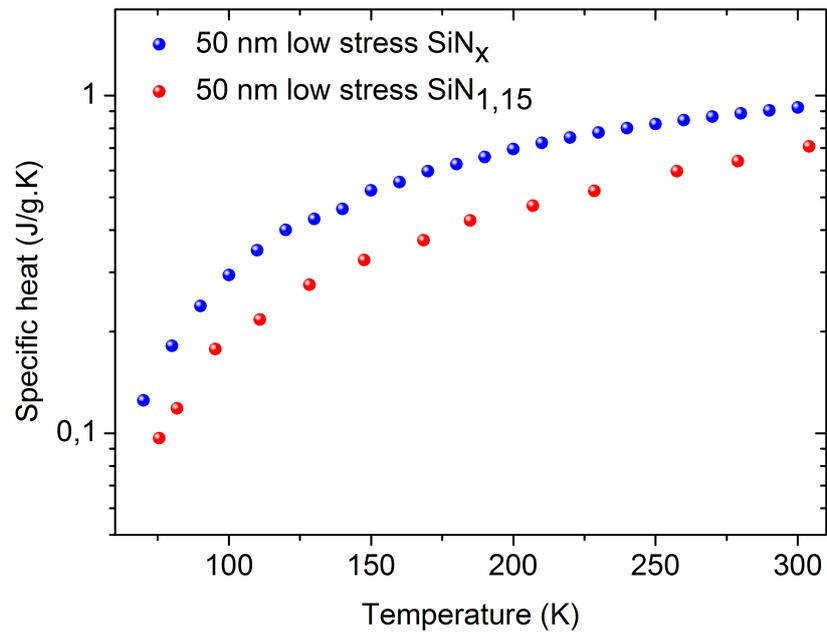
Figure 4.4: Experimental data measurements are shown for 50 nm $SiN_{1.15}$ [87], and 50 nm SiN_x measured by our method.

$n_0 = 481 \times 10^{45}$/J m^3. This will account for the high specific heat at low temperature as shown in the inset of Fig. 4.6. For the 50 nm SiN low stress which is slightly higher than the other curves at high temperature, we suggest that this behavior comes probably from the measurement conditions.

To summarize, we have demonstrated experimentally that stress has no effect on the specific heat of silicon nitride. This is consistent with the predictions of the V and γ models where it is assumed that stress increases the TLS barrier heights or decreases the coupling between phonons and TLS respectively.

Table 4.1: Parameters of fits for, A (50 nm low stress), B (100 nm low stress), C (50 nm high stress) and D (100 nm high stress).

Quantities	Low stress		High stress	
	A(50 nm)	B(100 nm)	C(50 nm)	D(100 nm)
ρ (10^3 Kg.m^3)	2.7	2.7	3.1	3.1
υ_L (10^3 m/s)	11.7	11.7	11.17	11.17
S_c	5	4	7	9
Θ_D (K)	649	620	630	650
n_0 (10^{45}/J m^3)	644.9	172.75	770	481.7
$\hbar\Omega_0/k_B$ (K)	150	150	130	130
$n_0 \times 10K/(N/V)(10^{-3})$	5.6	1.8	8	5
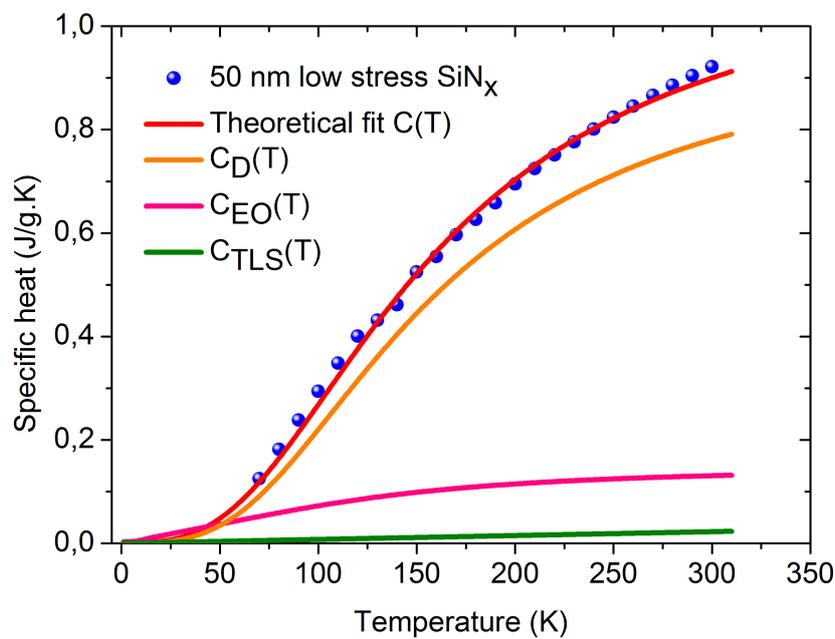
Figure 4.5: Specific heat measurement of 50 nm low stress SiN$_x$. The red solid line is the theoretical fit to experimental data $C(T)$, is given by the sum of $C_D(T)$, $C_{EO}(T)$ and $C_{TLS}(T)$. The parameters of the fit are given in Table 4.1.

4.4.1.1 Low temperature behaviors

Fig. 4.7 shows the measured heat capacity of 50 nm Si$_3$N$_4$ high stress along with both calculated heat capacities using the Deybe model C_D and $C(T)$ given by Eq. 4.31. The measured heat capacity is apparently much higher than what is expected from the Debye phonon heat capacity. This is especially significant below 100 K when the heat capacity deviates significantly from the T^3 Debye law.

As shown in Fig. 4.7, below 3 K this deviation is well explained by the TLS model, where
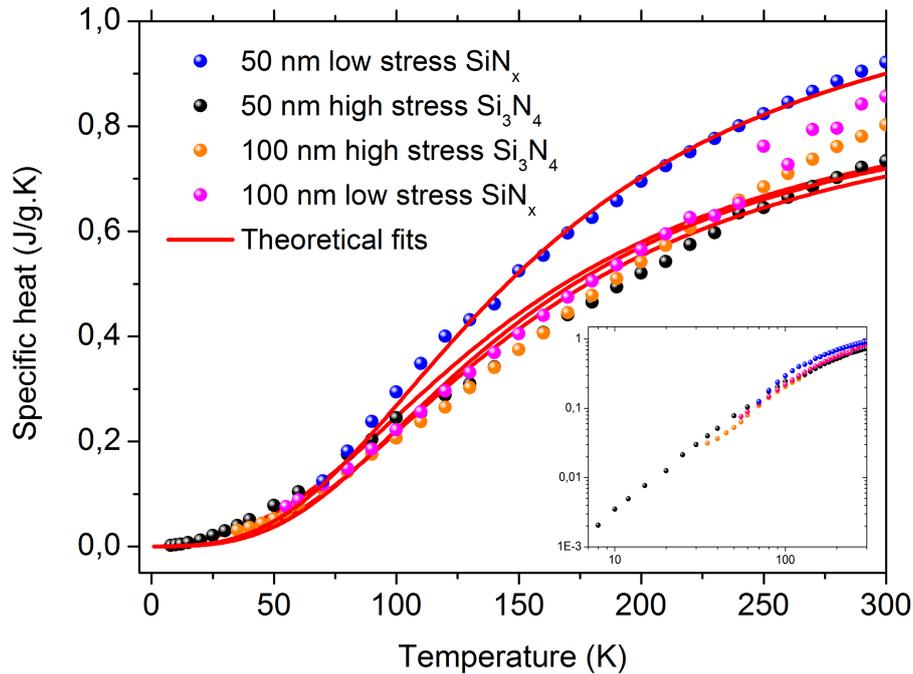
Figure 4.6: Specific heat measurement of 50 nm and 100 nm thick of both SiN low stress and high stress along with their respective fit using Eq. 4.31. The parameters of fits are given in Table 4.1.

TLS dominates the contribution to the specific heat, thus C varies linearly with temperature.

Above 3 K, C still deviates strongly from the expected $C_D \propto T^3$ dependence, exhibiting a bump in C/T^3 at about ~ 10 K as shown Fig. 4.8. This bump reflects the presence of an excess of modes in the vibrational density of states, and could be related to the so-called boson peak observed by neutron or Raman vibrational spectroscopies [88]. Moreover, in the same temperature range the thermal conductivity shows a plateau. The boson peak is an universal behavior of glasses and supercooled liquid and it is responsible for the low temperature anomalies in the thermodynamic properties. Fig. 4.9 shows experimental data of amorphous materials at low temperature which show boson peak around 10 K.

It has been shown that a consistent description of these additional anomalous features is possible in terms of the soft potential model [89, 90]. The soft potential model assumes the existence of additional quasi-local vibrations that interact with the sound waves, giving rise to the boson peak. This model can be considered as an extension at higher temperature of the two level system model TLS, describing the thermal anomalies of glasses below 1 K. The quasi-local vibrations are additional non acoustic modes characterized by a large vibrational amplitude of some group of atoms. In terms of the vibrational density of states $g(\omega)$ and the frequency ω, the boson peak is due to a maximum in $g(\omega)/\omega^2$. Whereas the Debye vibrational density of state which is proportional to ω^2 give a constant.

According to the soft potential model, the boson peak energy depends on the interaction
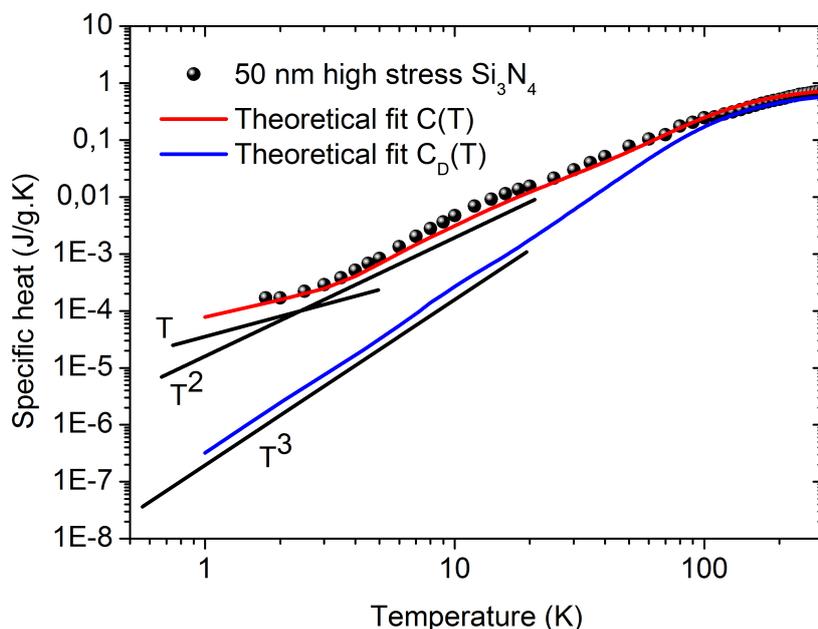
Figure 4.7: Specific heat measurement of 50 nm Si_3N_4 membrane from low temperature up to room temperature. The solid blue and red lines show theoretical predictions according to Debye's model and the model given by Eq. 4.31 respectively.
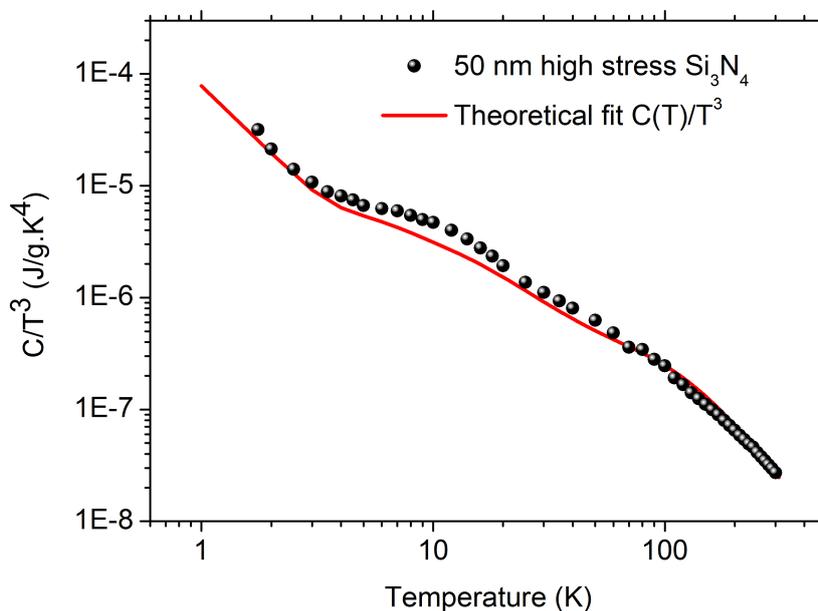
Figure 4.8: Specific heat measurement of 50 nm Si_3N_4 membrane divided by T^3. The solid line is the theoretical fit.

among the different harmonic oscillators (the quasi-local vibrations can be described as low frequency harmonic oscillators which weakly couple to the sound waves). Therefore, the energy of the boson peak is maximum where the interaction is stronger. On the other hand, the
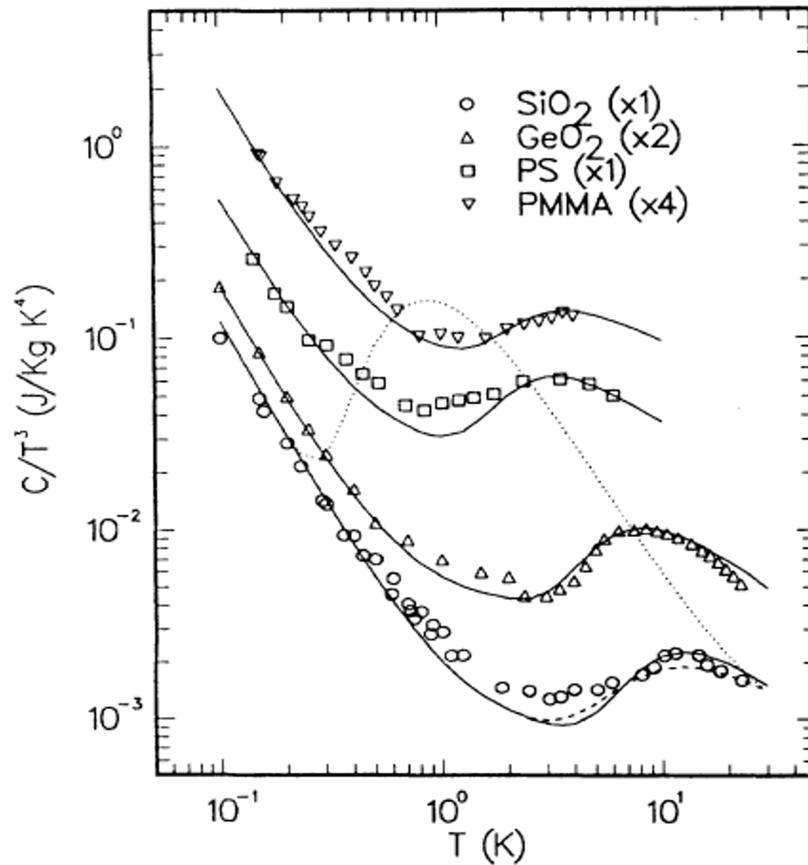
Figure 4.9: Experimental specific heat data divided by T^3 for different glasses, the solid lines are theoretical fits to the experimental data [80].

weak coupling between quasi-local vibrations and acoustic modes indicate no influence on the acoustic properties of the system. Moreover, it was recently shown that the same physical mechanism is fundamental for the formation of two-level systems and the boson peak. The raising of a peak in the reduced vibrational density of states seems to necessarily lead to the creation of two-level systems and vice versa [91].

The TLS density of state in SiN is around three orders of magnitude larger than values for amorphous SiO_2 [75, 80]. However, the energy of boson peak in SiO_2 seems to be much higher than that of SiN. This is provided predominately by a weak coupling between the quasi-local vibrations and acoustic modes in SiN.

4.4.2 Thermal conductivity

In glasses the thermal transport is due to propagating phonons [92], the thermal conductivity $\kappa(T)$ may be written as

$$\kappa(T) = \frac{1}{3} \int_0^{\omega_D} C_D(T, \omega) \upsilon l(T, \omega) d\omega \tag{4.36}$$

where ω_D is the Debye frequency, and υ is given by a weighted average of longitudinal and transverse sound velocities,

$$\frac{3}{\upsilon^3} = \frac{1}{\upsilon_l^3} + \frac{2}{\upsilon_t^3}. \tag{4.37}$$

The specific heat is approximated by the Debye specific heat C_D as given by Eq. 4.32, and $l(T, \omega)$ is given by $l(T, \omega) = Q(T, \omega)\upsilon/\omega$.

Fig. 4.10 shows the predicted thermal conductivity for high stress and stress relieved Si_3N_4 according to the two assumptions V and γ, and the experimental data of 50 nm, 200 SiN low stress and SiO_2 [75]. Both the prediction of SiN high stress and theoretical fits of experimental data are performed using Eq. 4.36. Note that with the γ approach, the average barrier height is taken as $V_0 = 0$.

As shown in Fig. 4.10, this model fits the thermal conductivity of SiN low stress and SiO_2 very well. The required parameters to perform the fits such as V_0 σ_0 are obtained from the fit of the mechanical dissipation of low stress silicon nitride using Eq. 4.23 and Eq. 4.29. However, the both theoretical predictions V and γ of Si_3N_4 high stress are much higher than that of low stress with a thermal conductivity at room temperature around 35 W/m.K and 21×10^3 W/m.K, respectively. Moreover according to V and γ assumption for the Si_3N_4 low stress, the thermal conductivity is around 16 W/m.K and 170 W/m.K, respectively.

According to this model, the predicted thermal conductivity is surprisingly much higher than the experimental data. This was seen in all cases and especially for the high stress Si_3N_4.

In order to study any possible effects of stress on silicon nitride thermal conductivity, we have used this model to fit our data. We have applied V approach, because with γ approach the predicted curve at room temperature shows a thermal conductivity with three order of magnitude higher than the experimental data as shown in Fig. 4.10.

Fig. 4.11 shows the thermal conductivity measurement of 100 nm SiN_x along with the theoretical fit using Eq. 4.36. To perform the fit, the parameters V_0 and σ_0 are determined from the fit of the mechanical dissipation. Therefore, we follow the authors in Ref. [75], where the experimental data of dissipation shown in Fig. 4.3 for LPCVD silicon nitride high stress and low stress are fitted through Eq. 4.29.
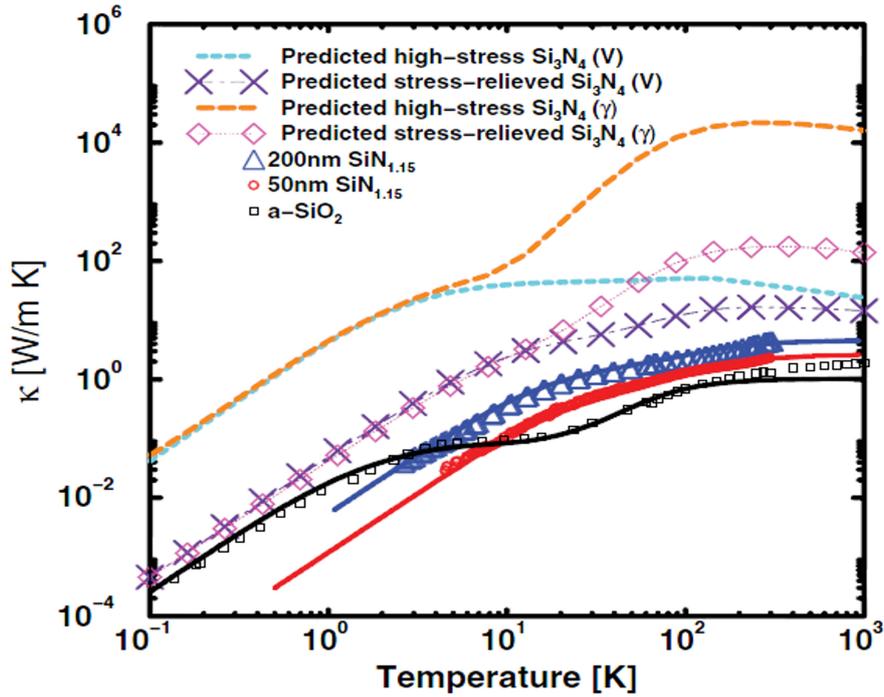
Figure 4.10: $\kappa(T)$ vs T for amorphous SiO_2 and silicon nitride. Experimental data points are shown for 50- and 200-nm-thick $SiN_{1.15}$ and SiO_2. The solid lines through the points are theoretical fits. Predictions where stress affects V or γ are indicated in the legend by (V) and (γ), respectively [75].

The other parameters $\bar{P}$, γ are determined from the fit of the thermal conductivity in such way that these conditions are satisfied [74],

$$Q_{\text{plat}}^{-1} = \frac{\pi \bar{P} \gamma^2}{2\rho \upsilon^2} \exp\left[-\frac{V_0^2}{2\sigma_0^2}\right] \sim \begin{cases} 10^{-4} - 10^{-3} & \text{for SiN low stress,} \\ 10^{-7} - 10^{-6} & \text{for SiN high stress.} \end{cases} \tag{4.38}$$

The parameters of the fits of 50 nm high stress and 100 nm low stress are shown in Table. 4.2.

As shown in Fig. 4.12, by using the condition of Eq. 4.38 we find that the theoretical fit is much higher than the experimental data. Moreover we find that the fits of SiN high stress works only if we multiply Q_{plat}^{-1} by a factor of $\sim 10^{-3}$. Thus if we take the condition of low stress, however the fitted data are for SiN high stress. This is consistent with the experimental data which shows a slight difference between the different measurement of SiN high stress and low stress as shown in Fig. 4.13.

Thus, we presume that the initial assumption $A = 1$ is not true, and $A \sim 10^{-3}$. Consequently, we can conclude that stress does not affect the dissipation in silicon nitride. Therefore, the

Figure 4.11: Thermal conductivity measurement of 100 nm high stress membrane along with the theoretical fits using Eq. 4.36.
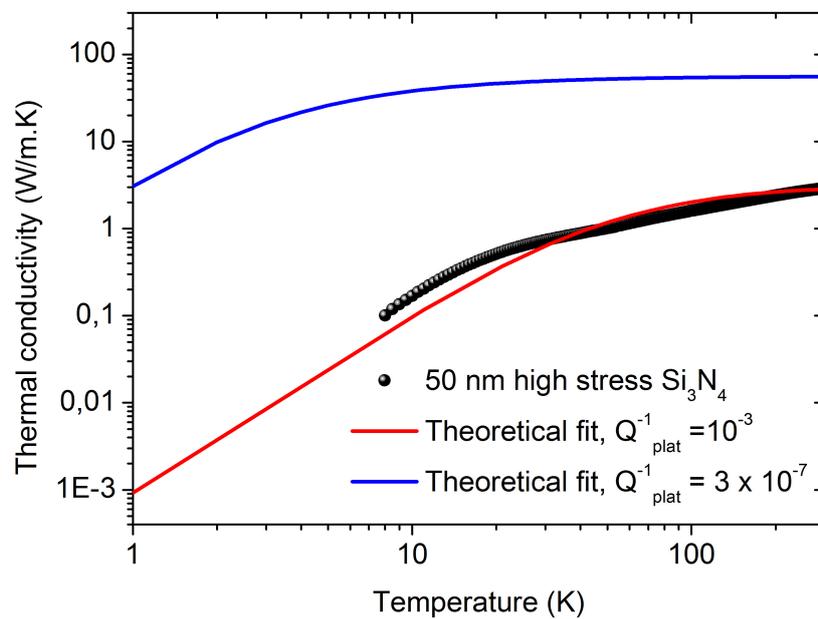
Figure 4.12: Thermal conductivity measurement of 50 nm high stress membrane along with the theoretical fits using Eq. 4.36.

dissipation dilution seems to be the cause of the reduction of dissipation by an applied stress in high stress silicon nitride. In addition stress should not affect thermal conductivity of silicon nitride as it is seen experimentally.
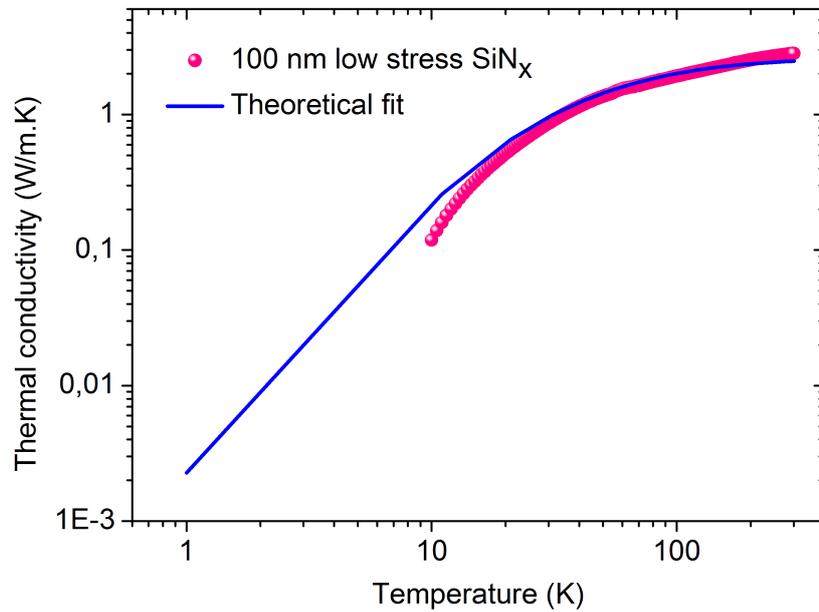
Table 4.2: Parameters of fits for thermal conductivity of 50 nm Si_3N_4 high stress and 100 nm SiN_x low stress.

Quantities	Low stress 100 nm	High stress 50 nm red line	blue line
S_k	0.8	3	3
$\bar{P}(10^{45}/J.m^3)$	1.16	5.17	5.17
γ (eV)	8.7	50	0.83
$\sigma_0(\times 10^3$ K)	9	7.5	7.5
$V_0(\times 10^4$ K)	2.3	3.05	3.05
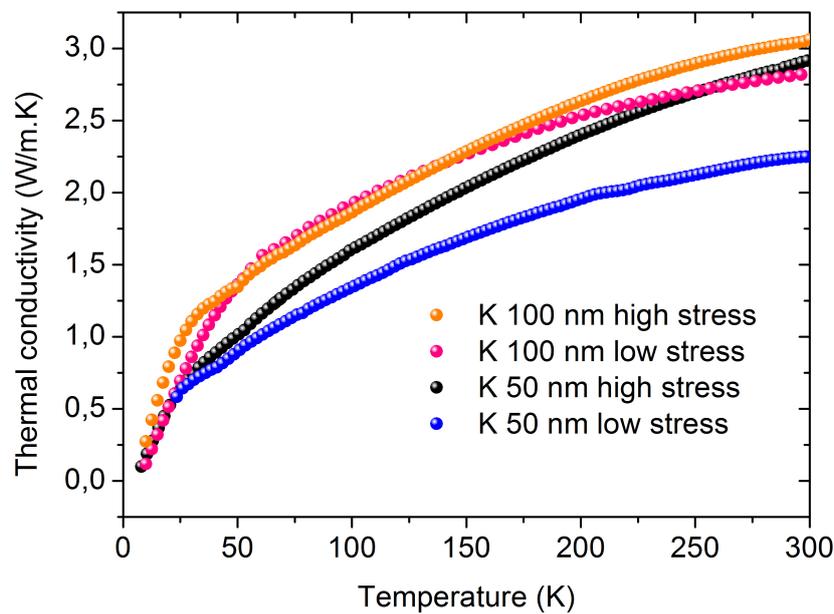
Figure 4.13: Thermal conductivity measurement of 50 nm and 100 nm thick membrane for both SiN low stress and high stress. The 100 nm curves of low stress and high stress show nearly no difference. The 50 nm curves show more difference at high temperature.

Fig. 4.13 shows results of thermal conductivity measurement of 50 nm and 100 nm membrane for both silicon nitride high stress and low stress. At low temperature $T < 20$ K, the curves are very close to each others, where the characteristic plateau is expected in the same temperature range. For $T > 20$ K, $\kappa(T)$ curves for high stress and low stress 100 nm membrane lie on top of each other, with the exception at room temperature where they show a slight difference. Whereas, $\kappa(T)$ curves for high stress and low stress 50 nm membrane show a difference up to 25 % at room temperature.

Fig. 4.14 shows the phonon mean free path in the membranes determined from $l = 3\kappa/Cv$. At high T all curves (with the exception of 50 nm low stress) approach the same limit at room temperature which is two times higher than the inter-atomic spacing (≈ 2.5 A° for amorphous SiN). As the temperature decreases, the mean free path increase rapidly to reach an order of

ten nanometers at 20 *K*. This is surprisingly small and cannot explain the sensitivity to the reduced dimension. Moreover, this can be explained by the fact that the measured *C* includes large contributions from local excitations that do not carry heat.
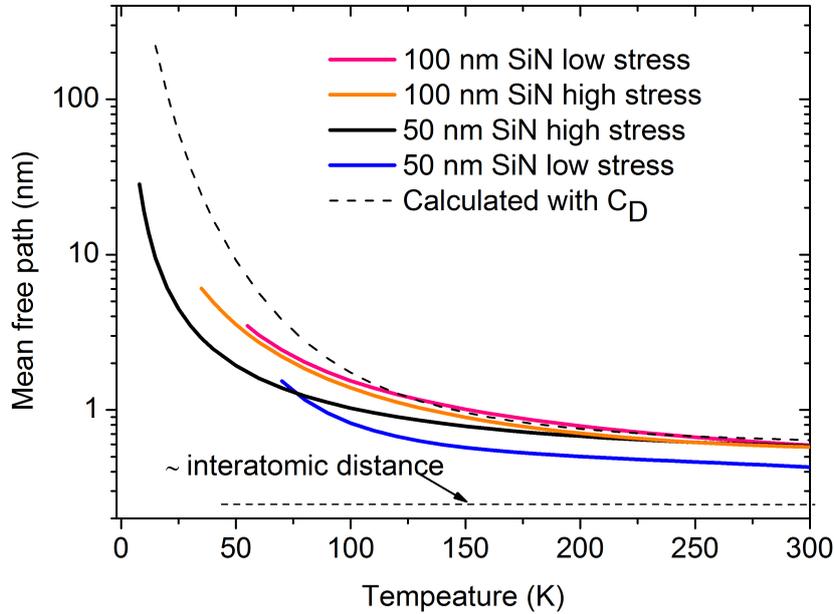
Figure 4.14: Mean free path of measured samples calculated using experimental data. The dashed line shows the estimation of the mean free path using C_D.

Therefore the mean free path is estimated using C_D, with the common model of disordered insulator [34, 45]. Below 30 K, *l* exceeds the 50 nm membrane thickness. Whereas for the 100 nm membrane *l* is still lower than the membrane thickness.

We return towards the behavior at room temperature. In most materials *l* saturates closer to the interatomic spacing near room temperature. The $\sim$ 2-3 times higher saturation may be an evidence for phonon transport due to far larger than expected contribution from long wavelength modes [93]. It was shown recently that a very small population of phonons with mean free path on the order of 1 μm and wavelength much longer than the expected thermal wavelengths carry up to 50 % of the heat in SiN at room temperature [93].

Therefore, if long *l* phonons carry a significant amount of heat in SiN a higher *T*, reduced system such as suspended membrane should show evidence of surface scattering effects even at room temperature. This possible effect in our samples are highlighted through an AFM measurements. Fig. 4.15 shows AFM scan results on four samples similar to those measured before. The rms height roughness for all samples shows a comparable values. One find 0.7 nm, 0.55 nm, 0.57 nm, and 0.48 nm for 50 nm high stress, 50 nm low stress, 100 nm high stress, and 100 nm low stress, respectively. At given temperature, the dominant phonon wave length is given by $\lambda_{dom} = \upsilon/\nu_{max}$. Here $\upsilon \approx 6.5 \times 10^3$ m/s is the average velocity of sound and $\nu_{max} = 4.25 k_B T/h \sim 90$ GHZ $\times T$ is the dominant frequency. This gives $\lambda_{dom} = 0.24$ nm at 300 K. This shows no evidence of surface scattering effects at room temperature in our samples.
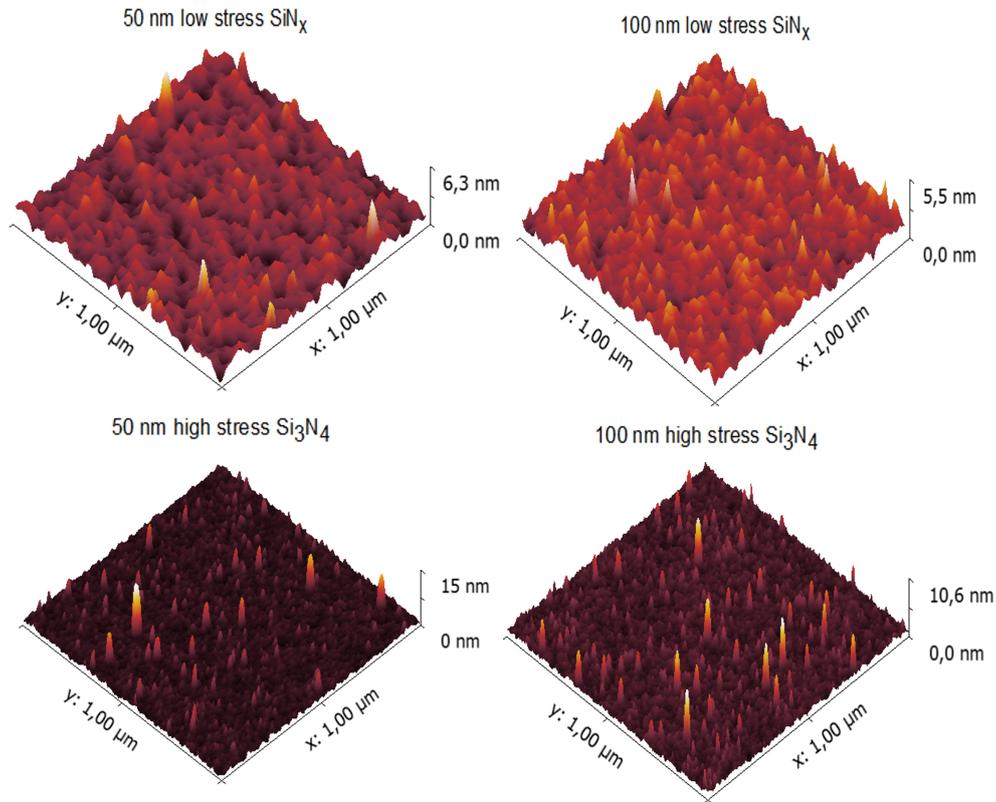
Figure 4.15: AFM micrographs for 50 nm and 100 nm of both SiN low stress and high stress. The rms height roughness shows a comparable values.

4.4.2.1 Low temperature behavior

The 50 nm and 100 nm membrane thick of SiN high stress are measured at low temperature, 30 mK $< T <$ 10 K using the same measurement chain. The thermal conductivity measurements are shown in Fig. 4.16 along with the theoretical fits using Eq. 4.36.

The 50 nm curve is in good agreement with the fit, where a T^2 rise is shown as it is expected in this range of temperature. However this plateau is extended until 2 K where another unexpected rise in temperature is shown. Whereas the 100 nm curve shows a plateau with a rise slightly higher that T^2, and as $\kappa(T)$ of 50 nm, another unexpected rise in temperature is starting at 1 K.

At 2 K the dominant phonon wave length is given by $\lambda_{dom} = 36$ nm. While this is still significantly less than the membrane thickness, the number of allowed modes in the thickness direction will be substantially reduced from the 3D limit. Thus we suggest that the difference in κ is due to enhancement of the boundary scattering at the membrane surfaces, which is more enhanced in the 50 nm than the 100 nm membrane thick.

At $T = 2$ K, the phonon mean free path exceed the 1μm. Thus this behavior of $\kappa(T)$ for

$T < 2$ K indicates that specular scattering occurs at the surfaces and dominate the phonon transport. Therefore, we assume that the second unexpected rise at $T < 2$ K can be explained by the fact that one attains the limits of applicability of the 3ω method.

The main limitation of this method lies in the need to define the local temperature on each point of the membrane. Moreover, the 3ω voltage is related to the thermal conductance of the membrane through Fourier's law. However, when the transport is ballistic, the notion of local temperature disappears. At very low temperatures, the phonons mean free path is much larger than the membrane thickness, thus the temperature can no longer be defined at the membrane surfaces. However, to solve the equation of heat transfer, we consider that the membrane have the same temperature in cross plane. We assume that this assumption becomes no longer valid in this temperature range.
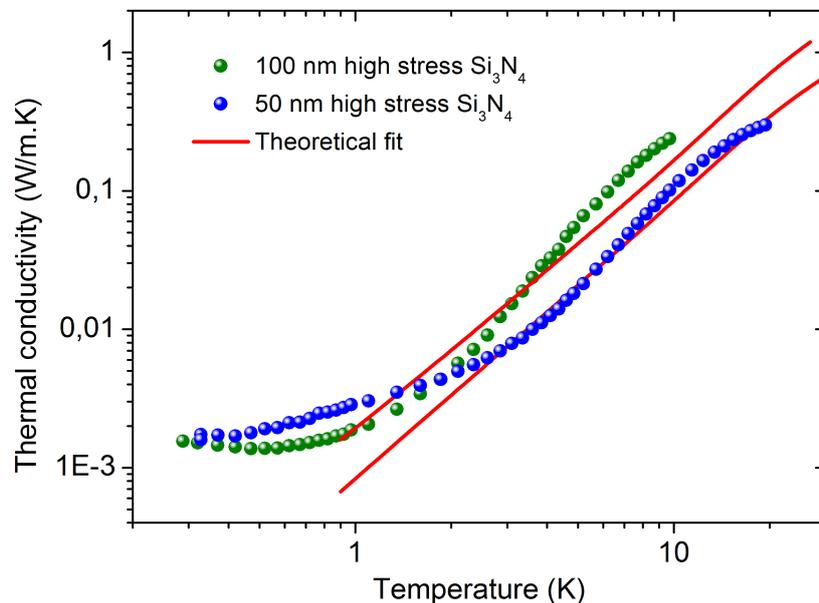
Figure 4.16: Thermal conductivity measurement of 50 nm and 100 nm high stress membrane at low temperature 300 mK $< T <$ 300 K, along with the theoretical fits.

Fig. 4.17 shows the thermal conductivity measurement from 300 mK to 300 K of 50 nm and 100 nm high stress SiN membrane. The curves deviate at low temperature (T < 1 K and T < 2 K for 100 nm and 50 nm, respectively) from the T^2 rise as we have explained above. Then the curves show the expected plateau upto $\sim$ 20 K and the second rise in temperature as predicted for amorphous materials.
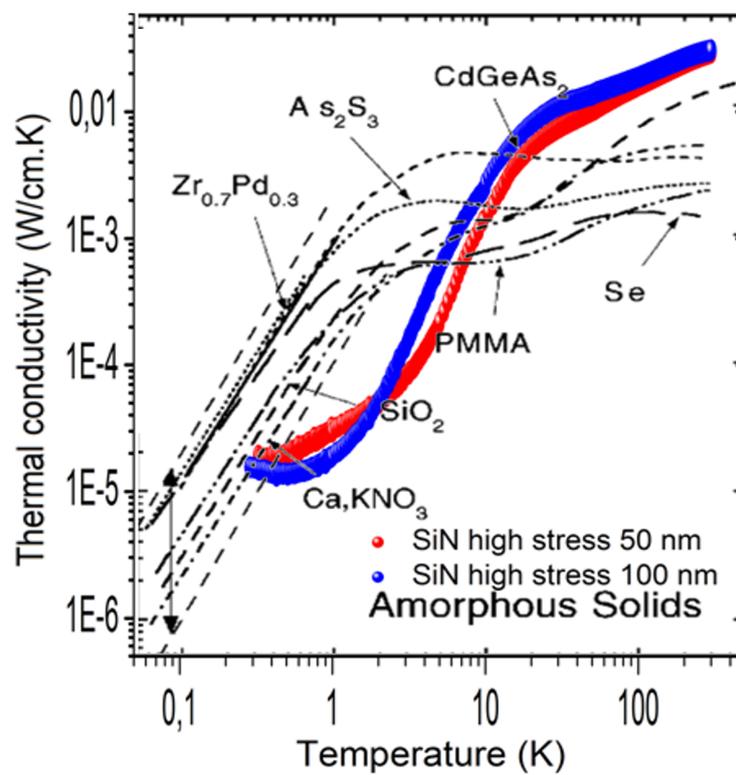
Figure 4.17: Thermal conductivity of several amorphous solids [42, 94]. The blue line and red line are our experimental measurement for 50 nm and 100 nm SiN high stress respectively.

Chapter 5

3ω-Völklein method application

Since 1990, the 3ω technique is used to characterize thermal properties of materials from nanoscale to bulk. Moreover, it is adapted to measure thermal properties of materials with different forms; solid, liquid, gas and powder [65]. However, there is still some deficiencies which limits its practical applications, the lack in sensitivity in some cases. In addition, for the electrically conductive specimen, an insulating layer about tens of nanometers thick, SiO_2 or SiN_x in most cases should be deposited on the measured surface to prevent electrical conduction through the specimen. However, in the case of porous or relatively rough surface, the deposited layer for insulation can become easily ineffective.

Here we propose that the earlier characterized SiN membrane can be used as a highly sensitive sensor to measure thermal properties of another material deposited on the backside of the membrane. The mechanical properties of silicon nitride, the fact that it is an insulating material, the stability with temperature, and its low thermal conductivity, all this makes it a perfect candidate to play this role; demonstrating the high versatability of the 3ω method on membrane for the thermal characterisation of thin films.

5.1 Thermal model

We demonstrate in this section the application of the SiN sensor (constituted by a 100 nm SiN membrane and the deposited NbN thermometer on topside), to the measurements of thermal conductance and heat capacity of 200 nm Bi_2Te_3 thermoelectric film. The Bi_2Te_3 film is deposited on the backside of the SiN membrane by magnetron sputtering technique. The main idea in this model is that if we have the thermal properties of the suspended SiN membrane measured by 3ω-Völklein method, we can extract thermal properties of another material deposited on backside of membrane by measuring the two films together.

As the Bi_2Te_3 film is sufficiently thin ($\sim 200nm$), we assume that the part of films (SiN

and Bi$_2$Te$_3$) just beyond the NbN transducer are heated like the thermometer. Thus, there is no gradient of temperature in the cross plane direction. Consider the geometry shown in Fig. 5.1, the 100 nm SiN membrane is supported by the silicon substrate and the Bi$_2$Te$_3$ film is deposited on the backside of the membrane. The aim of this experiment was to validate the assumption that the SiN membrane can be used to measure another material. Thus, in order to simplify, the resistance of contact between SiN and Bi$_2$Te$_3$ film it not taken into account at the initial stage. According to the assumptions given above, the equation of heat transfer of the system given by the two films is given by Eq. 3.45,

$$\frac{\partial^2 T(x,t)}{\partial x^2} = \frac{1}{D}\frac{\partial T(x,t)}{\partial t}$$

where D the total thermal diffusivity is given by,

$$D = \frac{\kappa_{\text{SiN}} + \kappa_{\text{Bi}_2\text{Te}_3}}{\rho_{\text{SiN}}C_{\text{SiN}} + \rho_{\text{Bi}_2\text{Te}_3}C_{\text{Bi}_2\text{Te}_3}} \tag{5.1}$$

where κ_{SiN}, C_{SiN}, ρ_{SiN}, and $\kappa_{\text{Bi}_2\text{Te}_3}$, $C_{\text{Bi}_2\text{Te}_3}$, $\rho_{\text{Bi}_2\text{Te}_3}$ are the thermal conductivity, specific heat and density of SiN and Bi$_2$Te$_3$ respectively.
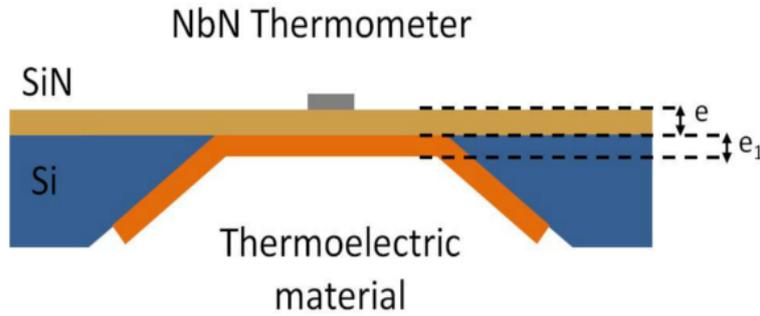
Figure 5.1: Schematic of SiN membrane shows the thermoelectric material deposited on the backside. e is the thickness of the membrane and e_1 the thickness of the thermoelectric film.

The heat capacity C' defined in Eq. 3.44 by the heat capacity of the half NbN thermometer and the part of SiN membrane beyond it, becomes,

$$C' = \rho_{\text{NbN}}c_{\text{NbN}}Le'\frac{b}{2} + c\rho\frac{b}{2}Le + \rho_{\text{Bi}_2\text{Te}_3}c_{\text{Bi}_2\text{Te}_3}Le_1\frac{b}{2} \tag{5.2}$$

where e_1 is the thickness of Bi$_2$Te$_3$ film. As the heat is transferred in plane by the two layers, the thermal conductance K_p becomes,

$$K_p = K_{\text{SiN}} + K_{\text{Bi}_2\text{Te}_3}. \tag{5.3}$$

Therefore, the thermal conductivity of Bi_2Te_3 film at low frequency can be calculated by,

$$V_{3\omega} = \frac{1}{2}\alpha R \sum_{m=0}^{\infty} \sum_{n=1}^{\infty} \frac{S_{mn}RI^2(-1)^{m+1}[1-(-1)^n]}{n\pi^3 \ell^2 (K_{SiN} + K_{Bi_2Te_3}) \left[\left(\frac{n}{L}\right)^2 + \left(\frac{m+1/2}{\ell}\right)^2\right]} \qquad (5.4)$$

Once the thermal conductivity of the Bi_2Te_3 film is calculated using Eq. 5.4, the specific heat can be determined by fitting the 3ω voltage versus frequency through,

$$|V_{3\omega}^{rms}(\omega)| = \frac{\alpha R_e^2 R_1 (V_{ac}^{rms})^3}{4(R_e + R_1)^4 \left(K_{SiN} + K_{Bi_2Te_3}\right)\left[1 + \omega^2\left(4\tau^2 + \frac{2\ell^4}{3D^2} + \frac{4\tau\ell^2}{3D}\right)\right]^{1/2}} \qquad (5.5)$$

where $\tau = C'/K_p$. C' and D are given by Eq. 5.2 and Eq. 5.1 respectively.

5.1.1 Experimental results

Fig. 5.2 and Fig. 5.3 show respectively the thermal conductivity and specific heat of a 200 nm thick Bi_2Te_3 film. The measurement has been performed between 100 and 300 K. The general behaviors is an decrease of the thermal conductivity and increase of the specific heat respectively as the temperature increases, a usual trends reported in the literature for Bi_2Te_3. A value close to 1 W/m.K and 0.3 J/g.K are obtained at room temperature for thermal conductivity and specific heat, respectively. These results are in good agreement with previous measurements [32, 95], confirming a very low thermal conductivity for this thermoelectric materials.
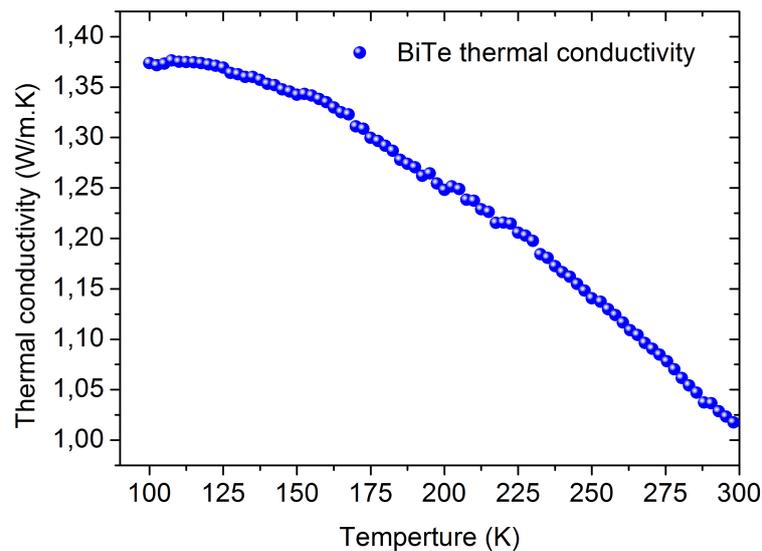
Figure 5.2: Thermal conductivity of 200 nm thick Bi_2Te_3 film as a function of temperature.
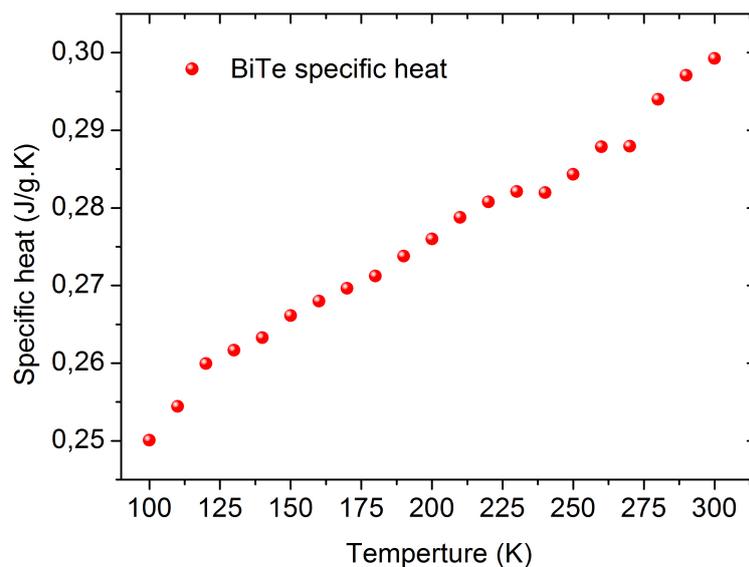
Figure 5.3: Specific heat of 200 nm thick Bi_2Te_3 film as a function of temperature.

5.2   Advantages and limits of the 3ω-Völklein method

Among the different methods dedicated to measure thermal properties, these measurements can be performed either by a steady state or a time dependent heat flow method. Both types have advantages and disadvantages and the best choice depends on the requirements of the experiment. Most of steady state experiments lead to obtain in-plane thermal conductivity. This method uses a heat source-sink principle and the temperature is measured using thermocouples positioning at two or more separate locations along the film. Thus when the film is ultra thin, the out of plane measurement becomes very difficult. On the other hand, time dependent methods are

widely used to obtain out of plane thermal conductivities, especially for layered systems. These methods can overcome most difficulties provided by the steady state techniques. However, the thermal penetration depths should carefully considered to be larger than the substrate thickness.

Furthermore, the different techniques can be categorized according to the heating and temperature sensing methods by: electrical heating and sensing, optical heating and sensing, and combined electrical/optical methods [57]. Although the optical techniques can eliminate influences of pads on a temperature field measurement, since they do note require contact with sample, the overlapping of the optics and probe light at the region of excitation can reduce the accuracy of this method. Therefore, the electrical techniques are the most popular, due to their simple experimental setups and their superior measuring ability.

In this study, we have coupled the 3ω method to suspended membrane geometry to obtain a specific thermal sensor able to characterize another material deposited on the backside of the membrane. We have tested this model to measure thermal properties of Bi_2Te_3 film and the results are in excellent agreement with literature. As the SiN is an insulator, this model is able to measure very thin film whatever its nature, insulator, semi-conductor or metallic. The only limit of this method can be at very low temperature, where the transport of phonon becomes ballistic and the thermal decoupling between the different layers; thermometer, SiN and measured film influences the measurement.

Conclusion

We have proposed and experimentally demonstrated a new technique to measure thermal properties of very thin membranes. This technique consists in coupling the 3ω method to the Völklein geometry (elongated suspended membrane). A NbN transducer is deposited on the center of the membrane which serves both as heater and thermometer. The sample of interest is then implemented into a specific Wheatstone bridge in order to eliminate the electrical 1ω signal. This technique allows the measurement with very high sensitivity of the 3ω thermal signal. Moreover, this measurement chain has the advantage to remove the different harmonics which do not have a thermal origin. Silicon nitride membranes studied in this work constitute a typical amorphous materials. We have been interested in the study of the thermal transport in such system of reduced dimensions as function of temperature and intrinsic modified stress. In order to accomplish this goal, silicon nitride membranes of high stress and low stress have been measured respectively with the thickness 50 nm and 100 nm.

The overall behaviour of the measured thermal conductivity is an increase as the temperature is increased, a trend commonly found for amorphous material. The data of 100 nm thick SiN membrane of low stress and high stress show a very comparable curves, whereas the 50 nm curves of low stress and high stress deviate at high temperature. The 50 nm data show thermal conductivity less than that of the 100 nm, this is consistent of the effect of reduced dimensions. The expected plateau are seen for temperature T < 20 K, down to 2 K and 1 K for SiN 50 nm and 100 nm membrane thick respectively. The plateau of the 50 nm curve is in good agreement with T^2 rise, whereas the 100 nm curve shows a plateau with a rise slightly higher than T^2. At T = 2 K, the phonon mean free path exceed the 1μm. Thus this behavior of κ(T) for T < 2 K indicates that specular scattering occurs at the surfaces of the membranes and dominates the phonon transport. Therefore, we assume that the second unexpected rise for T < 2 K could be explained by the fact that one attains the limits of applicability of the 3ω method.

The measured heat capacity is apparently higher than what is expected from the Debye phonon heat capacity. This is especially significant below 100 K where the heat capacity deviates significantly from the T^3 Debye law. Below 1 K this deviation is well explained by the TLS model, where TLS dominates the contribution to the specific heat, thus C varies linearly with temperature. Above 1 K, C still deviates strongly from the expected $C_D \propto T^3$ dependence, exhibiting a bump in C/T^3 at about $\sim$ 10 K. This bump reflects the presence of an excess of modes in the vibrational density of states, and could be related to the so-called boson peak. It has been shown that a consistent description of these additional anomalous features is possible

in terms of the soft potential model. The soft potential model assumes the existence of additional quasi-local vibrations that interact with the sound waves, giving rise to the boson peak. The TLS density of state in SiN is around three orders of magnitude larger than that of amorphous SiO_2. However, the amplitude of boson peak in SiN seems to be much smaller than that of SiO_2. This is provided predominately by a weak coupling between the quasi-local vibrations and acoustic modes in SiN.

It was seen experimentally that stress has no effect on the specific heat of silicon nitride. Moreover, we have demonstrated that stress does not affect the dissipation in silicon nitride, and the dissipation dilution seems to be the sole cause of the reduction of dissipation by an applied stress in high stress silicon nitride. Therefore, stress should not affect thermal conductivity of silicon nitride, and this is consistent with the experimental results.

As application for this method, we have demonstrated that the SiN membrane can be used as specific thermal sensor to characterize another material deposited on the backside of the membrane. We have tested this model to measure thermal properties of Bi2Te3 film and the results are in excellent agreement with literature. As the SiN is an insulator, this model is able to measure very thin film whatever its nature, insulator, semi conductor or metallic. The only limit of this method can be at very low temperature, where the transport of phonon becomes ballistic at the surfaces of the membranes, and the thermal decoupling between the different layers starts to influence the measurement.

Bibliography

[1] David G. Cahill, Wayne K. Ford, Kenneth E. Goodson, Gerald D. Mahan, Arun Majumdar, Humphrey J. Maris, Roberto Merlin, and Simon R. Phillpot. Nanoscale thermal transport. *Journal of Applied Physics*, 93:793–818, 2003.

[2] C. Dames and G. Chen. Theoretical phonon thermal conductivity of Si/Ge superlattice nanowires. *Journal of Applied Physics*, 95:682–693, 2004.

[3] Y. Dubi and M. Di Ventra. Fourier's law: Insight from a simple derivation. *Physical Review E*, 79, 2009.

[4] P.G. Klemens. Theory of thermal conduction in dielectric solids: Effects of radiation damage. *Nuclear Instruments and Methods in Physics Research Section B: Beam Interactions with Materials and Atoms*, 1:204 – 208, 1984.

[5] Joseph Callaway. Model for lattice thermal conductivity at low temperatures. *Phys. Rev.*, 113:1046–1051, Feb 1959.

[6] Ali Shakouri. Recent developments in semiconductor thermoelectric physics and materials. *Annual Review of Materials Research*, 41:399–431, 2011.

[7] L. D. Hicks and M. S. Dresselhaus. Effect of quantum-well structures on the thermoelectric figure of merit. *Phys. Rev. B*, 47:12727–12731, May 1993.

[8] Avram Bar-Cohen and Peng Wang. On-chip hot spot remediation with miniaturized thermoelectric coolers. *Microgravity Science and Technology*, 21:351–359, 2009.

[9] J. S. Heron, T. Fournier, N. Mingo, and O. Bourgeois. Mesoscopic size effects on the thermal conductance of silicon nanowire. *Nano Letters*, 9:1861–1865, 2009.

[10] D. G. Cahill. Thermal conductivity measurement from 30 K to 750 K: the 3ω method. *Review of Scientific Instruments*, 61:802–808, 1990.

[11] Deyu Li, Scott T. Huxtable, Alexis R. Abramson, and Arun Majumdar. Thermal transport in nanostructured solid-state cooling devices. *Journal of Heat Transfer*, 127:108–114, 2005.

[12] Tom Klitsner and R. O. Pohl. Phonon scattering at silicon crystal surfaces. *Phys. Rev. B*, 36:6551–6565, 1987.

[13] Deyu Li, Yiying Wu, Philip Kim, Li Shi, Peidong Yang, and Arun Majumdar. Thermal conductivity of individual silicon nanowires. *Applied Physics Letters*, 83:2934–2936, 2003.

[14] S. M. Lee and D. G. Cahill. Heat transport in thin dielectric films. *Journal of Applied Physics*, 81:2590–2595, 1997.

[15] A. A. Joshi and A. Majumdar. Transient ballistic and diffusive phonon heat transport in thin films. *Journal of Applied Physics*, 74:31–39, 1993.

[16] Allon I. Hochbaum, Renkun Chen, Raul Diaz Delgado, Wenjie Liang, Erik C. Garnett, Mark Najarian, Arun Majumdar, and Peidong Yang. Enhanced thermoelectric performance of rough silicon nanowires. *NATURE*, 451:163–U5, JAN 10 2008.

[17] Jean-Savin Heron, Chandan Bera, Thierry Fournier, Natalio Mingo, and Olivier Bourgeois. Blocking phonons via nanoscale geometrical design. *PHYSICAL REVIEW B*, 82, OCT 29 2010.

[18] Christophe Blanc, Ali Rajabpour, Sebastian Volz, Thierry Fournier, and Olivier Bourgeois. Phonon heat conduction in corrugated silicon nanowires below the casimir limit. *Applied Physics Letters*, 103:043109, 2013.

[19] H. B. G. Casimir. Note on the conduction of heat in crystals. *Physica*, 5:495–500, June 1938.

[20] W. Holmes, J. M. Gildemeister, P. L. Richards, and V. Kotsubo. Measurements of thermal transport in low stress silicon nitride films. *Applied Physics Letters*, 72:2250–2252, 1998.

[21] Tom Klitsner, J. E. VanCleve, Henry E. Fischer, and R. O. Pohl. Phonon radiative heat transfer and surface scattering. *Physical Review B*, 38:7576–7594, 1988.

[22] A. Sikora, H. Ftouni, J. Richard, C. Hébert, D. Eon, F. Omnès, and O. Bourgeois. Highly sensitive thermal conductivity measurements of suspended membranes (SiN and diamond) using a 3ω-Völklein method. *Review of Scientific Instruments*, 83:054902, 2012.

[23] A. Sikora, H. Ftouni, J. Richard, C. Hébert, D. Eon, F. Omnès, and O. Bourgeois. Erratum: "Highly sensitive thermal conductivity measurements of suspended membranes (SiN and diamond) using a 3ω-Völklein method". *Review of Scientific Instruments*, 84:029901, 2013.

[24] Ankur Jain and Kenneth E. Goodson. Measurement of the Thermal Conductivity and Heat Capacity of Freestanding Shape Memory Thin Films Using the 3 omega Method. *Journal of Heat Transfer*, 130:102402, 2008.

[25] Yan Zhang, J. Christofferson, A. Shakouri, Deyu Li, A. Majumdar, Yiying Wu, Rong Fan, and Peidong Yang. Characterization of heat transfer along a silicon nanowire using thermoreflectance technique. *Nanotechnology, IEEE Transactions on*, 5:67 – 74, jan. 2006.

[26] Xi Liu, Xiaoming Wu, and Tianling Ren. In situ and noncontact measurement of silicon membrane thermal conductivity. *Applied Physics Letters*, 98:174104, 2011.

[27] T. Kühn, D. V. Anghel, J. P. Pekola, M. Manninen, and Y. M. Galperin. Heat transport in ultrathin dielectric membranes and bridges. *Phys. Rev. B*, 70:125425, Sep 2004.

[28] D. V. Anghel, J. P. Pekola, M. M. Leivo, J. K. Suoknuuti, and M. Manninen. Properties of the phonon gas in ultrathin membranes at low temperature. *Phys. Rev. Lett.*, 81:2958–2961, Oct 1998.

[29] A. Barua, Md. S. Hossain, K.I. Masood, and S. Subrina. Thermal management in 3-D integrated circuits with graphene heat spreaders. *Physics Procedia*, 25:311 – 316, 2012.

[30] Suresh V. Garimella. Advances in mesoscale thermal management technologies for microelectronics. *Microelectronics Journal*, 37:1165 – 1185, 2006.

[31] Christophe Goupil. Thermodynamics of the thermoelectric potential. *Journal of Applied Physics*, 106:104907, 2009.

[32] Bed Poudel, Qing Hao, Yi Ma, Yucheng Lan, Austin Minnich, Bo Yu, Xiao Yan, Dezhi Wang, Andrew Muto, Daryoosh Vashaee, Xiaoyuan Chen, Junming Liu, Mildred S. Dresselhaus, Gang Chen, and Zhifeng Ren. High-thermoelectric performance of nanostructured bismuth antimony telluride bulk alloys. *Science*, 320:634–638, 2008.

[33] Yi Ma, Qing Hao, Bed Poudel, Yucheng Lan, Bo Yu, Dezhi Wang, Gang Chen, and Zhifeng Ren. Enhanced thermoelectric figure-of-merit in p-type nanostructured bismuth antimony tellurium alloys made from elemental chunks. *Nano Letters*, 8:2580–2584, 2008.

[34] R. C. Zeller and R. O. Pohl. Thermal Conductivity and Specific Heat of Noncrystalline Solids. *Physical Review B*, 4:2029–2041, 1971.

[35] Anthony J. Leggett. Amorphous materials at low temperatures: why are they so similar? *Physica B: Condensed Matter*, 169:322 – 327, 1991.

[36] W. A. Phillips. Tunneling states in amorphous solids. *Journal of Low Temperature Physics*, 7:351–360, 1972.

[37] P. w. Anderson, B. I. Halperin, and c. M. Varma. Anomalous low-temperature thermal properties of glasses and spin glasses. *Philosophical Magazine*, 25:1–9, 1972.

[38] André Gusso, M. G. E. da Luz, and Luis G. C. Rego. Quantum chaos in nanoelectromechanical systems. *Phys. Rev. B*, 73:035436, Jan 2006.

[39] R. M. Costescu, D. G. Cahill, F. H. Fabreguette, Z. A. Sechrist, and S. M. George. Ultra-low thermal conductivity in W/Al$_2$O$_3$ nanolaminates. *Science*, 303:989–990, 2004.

[40] S.-M. Lee, David G. Cahill, and Thomas H. Allen. Thermal conductivity of sputtered oxide films. *Phys. Rev. B*, 52:253–257, Jul 1995.

[41] D. A. Antoniadis K. E. Goodson, L. T. Su and M. I. Flik. Prediction and measurement of the thermal conductivity of amorphous dielectric layers. *Journal of Heat Transfer*, 116:317, 1994.

[42] Robert O. Pohl, Xiao Liu, and EunJoo Thompson. Low-temperature thermal conductivity and acoustic attenuation in amorphous solids. *Reviews of Modern Physics*, 74:991–1013, 2002.

[43] M. M. Leivo and J. P. Pekola. Thermal characteristics of silicon nitride membranes at sub-Kelvin temperatures. *Applied Physics Letters*, 72:1305–1307, 1998.

[44] Adam L. Woodcraft, Rashmi V. Sudiwala, Elley Wakui, Ravinder S. Bhatia, James J. Bock, and Anthony D. Turner. Thermal conductance measurements of a silicon nitride membrane at low temperatures. *Physica B: Condensed Matter*, 284-288:1968–1969, 2000.

[45] B. L. Zink and F. Hellman. Specific heat and thermal conductivity of low-stress amorphous Si-N membranes. *Solid State Communications*, 129:199–204, 2004.

[46] M. I. Flik, B. I. Choi, and K. E. Goodson. Heat transfer regimes in microstructures. *Journal of Heat Transfer-transactions of The Asme*, 114:666–674, 1992.

[47] A. Majumdar. Microscale heat-conduction in dielectric thin-films. *Journal of Heat Transfer-Transactions of Thin Asme*, 115:7–16, Feb 1993.

[48] T. Kühn and I.J. Maasilta. Ballistic phonon transport in dielectric membranes. *Nuclear Instruments and Methods in Physics Research Section A: Accelerators, Spectrometers, Detectors and Associated Equipment*, 559:724 – 726, 2006.

[49] B.A. Auld. *Acoustic Fields and Waves in Solids*, volume II. Robert E. Krieger Publishing Company, second edition, 1990.

[50] H. F. C. Hoevers, M. L. Ridder, A. Germeau, M. P. Bruijn, P. A. J. de Korte, and R. J. Wiegerink. Radiative ballistic phonon transport in silicon-nitride membranes at low temperatures. *Applied Physics Letters*, 86:251903, 2005.

[51] A Kaushik, H Kahn, and AH Heuer. Wafer-level mechanical characterization of silicon nitride MEMS. *Journal of microelectromechanical systemes*, 14:359–367, Apr 2005.

[52] DP Osterman, R Patt, R Hunt, and JB Peterson. Antenna-coupled bolometer with a micromachined-beam thermal link. *Applied physics letters*, 71:2361–2363, 1997.

[53] D. W. Denlinger, E. N. Abarra, Kimberly Allen, P. W. Rooney, M. T. Messer, S. K. Watson, and F. Hellman. Thin film microcalorimeter for heat capacity measurements from 1.5 to 800 K. *Review of Scientific Instruments*, 65:946–959, 1994.

[54] Wen-Hsien Chuang, Thomas Luger, Rainer K. Fettig, and R. Ghodssi. Mechanical property characterization of lpcvd silicon nitride thin films at cryogenic temperatures. *Microelectromechanical Systems, Journal of*, 13:870–879, 2004.

[55] A. Suvorova B.R. Lawn Y. Liu X.Z. Hu J.M. Dell L. Faraone H. Huang, K.J. Winchester. Effect of deposition conditions on mechanical properties of low-temperature PECVD silicon nitride films. *Materials Science and Engineering A*, pages 453–459, 2006.

[56] D. R. Southworth, R. A. Barton, S. S. Verbridge, B. Ilic, A. D. Fefferman, H. G. Craighead, and J. M. Parpia. Stress and Silicon Nitride: A Crack in the Universal Dissipation of Glasses. *Physical Review Letters*, 102, 2009.

[57] Terry M. Tritt. *Thermal Conductivity: Theory, Properties, and Applications*. Kluwer Academic / Plenum Publishers, 2004.

[58] O. M. Corbino. *Phys. Z.*, 11:413, 1910.

[59] O. M. Corbino. *Phys. Z.*, 12:292, 1911.

[60] Norman O. Birge and Sidney R. Nagel. Wide-frequency specific heat spectrometer. *Review of Scientific Instruments*, 58:1464–1470, 1987.

[61] Jung Hun Kim, Albert Feldman, and Donald Novotny. Application of the three omega thermal conductivity measurement method to a film on a substrate of finite thickness. *Journal of Applied Physics*, 86:3959–3963, 1999.

[62] Jiezhu Jin, Mohan P. Manoharan, Qing Wang, and M. A. Haque. In-plane thermal conductivity of nanoscale polyaniline thin films. *Applied Physics Letters*, 95:033113, 2009.

[63] Olivier Bourgeois, Thierry Fournier, and Jacques Chaussy. Measurement of the thermal conductance of silicon nanowires at low temperature. *Journal of Applied Physics*, 101:016104, 2007.

[64] X. Jack Hu, Antonio A. Padilla, Jun Xu, Timothy S. Fisher, and Kenneth E. Goodson. 3-Omega Measurements of Vertically Oriented Carbon Nanotubes on Silicon. *Journal of Heat Transfer*, 128:1109–1113, 2006.

[65] Scott N. Schiffres and Jonathan A. Malen. *Improved 3-omega measurement of thermal conductivity in liquid, gases, and powders using a metal-coated optical fiber*, volume 82. Review of Scientific Instruments, 2011.

[66] Olivier Bourgeois, Emmanuel Andre, Cristina Macovei, and Jacques Chaussy. Liquid nitrogen to room-temperature thermometry using niobium nitride thin films. *Review of Scientific Instruments*, 77:126108, 2006.

[67] David G. Cahill, M. Katiyar, and J. R. Abelson. Thermal conductivity of a-si:h thin films. *Phys. Rev. B*, 50:6077–6081, 1994.

[68] L. Dumoulin, L. Bergé, J. Lesueur, H. Bernas, and M. Chapellier. Nb-si thin films as thermometers for low temperature bolometers. *Journal of Low Temperature Physics*, 93:301–306, 1993.

[69] D. Querlioz, E. Helgren, D. R. Queen, F. Hellman, R. Islam, and David. J. Smith. Beneficial effects of annealing on amorphous Nb–Si thin-film thermometers. *Applied Physics Letters*, 87:221901, 2005.

[70] A. F. Lopeandia, E. Andre, J.-L. Garden, D. Givord, and O. Bourgeois. Highly sensitive parylene membrane-based ac-calorimeter for small mass magnetic samples. *Review of Scientific Instruments*, 81:053901, 2010.

[71] Myers G. E. *Analytical Methods in Conduction Heat Transfer*. AMCHT, Madison, WI, 2nd edition, 1998.

[72] D.L. DeVoe. Thermal issues in MEMS and microscale systems. *Components and Packaging Technologies, IEEE Transactions on*, 25:576–583, 2002.

[73] M.A. Haque and M.T.A. Saif. Thermo-mechanical properties of nano-scale freestanding aluminum films. *Thin Solid Films*, 484:364 – 368, 2005.

[74] D. R. Southworth, R. A. Barton, S. S. Verbridge, B. Ilic, A. D. Fefferman, H. G. Craighead, and J. M. Parpia. Stress and silicon nitride: A crack in the universal dissipation of glasses. *Phys. Rev. Lett.*, 102:225503, Jun 2009.

[75] Jiansheng Wu and Clare C. Yu. How stress can reduce dissipation in glasses. *Physical Review B*, 84:174109, 2011.

[76] P. Temple-Boyer, C. Rossi, E. Saint-Etienne, and E. Scheid. Residual stress in low pressure chemical vapor deposition sin_x films deposited from silane and ammonia. *Journal of Vacuum Science & Technology A: Vacuum, Surfaces, and Films*, 16:2003–2007, 1998.

[77] W. D. Nix M. F. Doerner. Stresses and deformation processes in thin films on substrates. *Critical Review in Solid state and Material Science*, 14, 1988.

[78] G. Gerald Stoney. The tension of metallic films deposited by electrolysis. *Proceedings of the Royal Society of London. Series A*, 82:172–175, 1909.

[79] C. Seoánez, F. Guinea, and A. H. Castro Neto. Surface dissipation in nanoelectromechanical systems: Unified description with the standard tunneling model and effects of metallic electrodes. *Phys. Rev. B*, 77:125107, Mar 2008.

[80] Clare C. Yu and J. J. Freeman. Thermal conductivity and specific heat of glasses. *Phys. Rev. B*, 36:7620–7624, Nov 1987.

[81] S. Hunklinger and A.K. Raychaudhuri. Chapter 3: Thermal and elastic anomalies in glasses at low temperatures. volume 9 of *Progress in Low Temperature Physics*, pages 265 – 344. Elsevier, 1986.

[82] J. Jäckle. Ultrasonic attenuation in glasses at low-temperatures. *Z. Phys*, 257:212–223, 1972.

[83] D. Tielbürger, R. Merz, R. Ehrenfels, and S. Hunklinger. Thermally activated relaxation processes in vitreous silica: An investigation by brillouin scattering at high pressures. *Phys. Rev. B*, 45:2750–2760, Feb 1992.

[84] Walter Schirmacher and Michael Wagener. Vibrational anomalies and phonon localization in glasses. *Solid State Communications*, 86:597 – 603, 1993.

[85] Xiao Liu, B. E. White, Jr., R. O. Pohl, E. Iwanizcko, K. M. Jones, A. H. Mahan, B. N. Nelson, R. S. Crandall, and S. Veprek. Amorphous solid without low energy excitations. *Phys. Rev. Lett.*, 78:4418–4421, Jun 1997.

[86] Y. L. Huang and Peter R. Saulson. Dissipation mechanisms in pendulums and their implications for gravitational wave interferometers. *Review of Scientific Instruments*, 69:544–553, 1998.

[87] D. R. Queen and F. Hellman. Thin film nanocalorimeter for heat capacity measurements of 30 nm films. *Review of Scientific Instruments*, 80:063901, 2009.

[88] U. Buchenau, M. Prager, N. Nücker, A. J. Dianoux, N. Ahmad, and W. A. Phillips. Low-frequency modes in vitreous silica. *Phys. Rev. B*, 34:5665–5673, Oct 1986.

[89] U. Buchenau, Yu. M. Galperin, V. L. Gurevich, D. A. Parshin, M. A. Ramos, and H. R. Schober. Interaction of soft modes and sound waves in glasses. *Phys. Rev. B*, 46:2798–2808, Aug 1992.

[90] L. Gil, M. A. Ramos, A. Bringer, and U. Buchenau. Low-temperature specific heat and thermal conductivity of glasses. *Phys. Rev. Lett.*, 70:182–185, Jan 1993.

[91] D. A. Parshin, H. R. Schober, and V. L. Gurevich. Vibrational instability, two-level systems, and the boson peak in glasses. *Phys. Rev. B*, 76:064206, Aug 2007.

[92] M. P. Zaitlin and A. C. Anderson. Phonon thermal transport in noncrystalline materials. *Phys. Rev. B*, 12:4475–4486, Nov 1975.

[93] Rubina Sultan, A. D. Avery, J. M. Underwood, S. J. Mason, D. Bassett, and B. L. Zink. Heat transport by long mean free path vibrations in amorphous silicon nitride near room temperature. *Phys. Rev. B*, 87:214305, Jun 2013.

[94] D G Cahill and R O Pohl. Lattice vibrations and heat transport in crystals and glasses. *Annual Review of Physical Chemistry*, 39:93–121, 1988.

[95] Salvatore Grasso, Naohito Tsujii, Qinghui Jiang, Jibran Khaliq, Satofumi Maruyama, Miriam Miranda, Kevin Simpson, Takao Mori, and Michael J. Reece. Ultra low thermal conductivity of disordered layered p-type bismuth telluride. *J. Mater. Chem. C*, 1:2362–2367, 2013.

RESUME

Les matériaux amorphes possèdent des propriétés thermiques très différentes de celles des matériaux cristallins. Autant L'effet de dimensions spatiales réduites sur le transport thermique a été observé dans les matériaux cristallins qu'il est mal connu pour les systèmes amorphes. Dans ce travail de thèse, nous avons étudié les propriétés thermiques des membranes très minces de SiN amorphe (système 2D). Afin d'atteindre cet objectif nous avons proposé et validé expérimentalement une nouvelle technique de mesure ultra-sensible (3ω-Völklein) des propriétés thermiques des membranes suspendues. Cette méthode unique permet de mesurer sur le même dispositif à la fois la conductivité thermique et la chaleur spécifique sur une plage de température allant de 4 K à 300 K. Nous avons utilisé cette méthode pour étudier l'effet de stress interne sur la conductivité thermique dans le SiN amorphe, ainsi que la variation des libres parcours moyens des phonons dans ces systèmes de basses dimensionnalités.

ABSTRACT

Amorphous materials have very different thermal properties of their crystalline counterparts. The effect of the reduced spatial dimensions on heat transport was extensively studied and observed in crystalline materials, which is not the case for amorphous. In this thesis, we study the thermal properties of thin amorphous SiN membranes (2D system). To achieve this goal, we have proposed and experimentally validated a new ultra-sensitive technique (3ω-Völklein) to measure the thermal properties of suspended membranes. This specific technique allows the measurement of both the thermal conductivity and the specific heat over a temperature range 4 K-300 K using the same device. We used this method to investigate the effect of internal stress on the thermal conductivity in amorphous SiN membrane, as well as the variation of phonons mean free path in such low dimensions systems.